CHARACTERIZATION OF Zr-Fe-Cu ALLOYS FOR AN INERT MATRIX FUEL FOR NUCLEAR ENERGY APPLICATIONS

A Thesis

by

BRIAN ANTHONY BARNHART

Submitted to the Office of Graduate Studies of
Texas A&M University
in partial fulfillment of the requirements for the degree of

MASTER OF SCIENCE

Chair of Committee,	Sean M. McDeavitt
Committee Members,	Lin Shao
	Raymundo Arroyave
Head of Department,	Yassin Hassan

August 2013

Major Subject: Nuclear Engineering

ABSTRACT

An ultra-high burnup metallic inert matrix nuclear fuel concept is being characterized and evaluated by Lawrence Livermore National Laboratory based on a metal matrix fuel concept originally developed at the Bochvar Institute in Russia. The concept comprises a dispersion of uranium metal microspheres in a Zr-based alloy matrix that provides thermal bonding between the fuel particles and the cladding material. The objective of this study was to experimentally evaluate both the microstructural and thermophysical properties of Zr-Fe-Cu alloys. The experiments and analyses described were divided into three main parts, nominally based on the analysis methods used to examine the alloys.

An Electron Probe Microanalyzer (EPMA) was used to characterize the metallurgical properties of the proposed matrix alloys. The groups of alloys were cast using a high temperature inert atmosphere furnace. The cast alloys showed the expected combination of phases with the exception of the $ZrFe_2$ Laves phase which was predicted for the Zr-12Fe-15Cu[1] alloy but was not detected. The Zr-12Fe-5Cu alloy consisted of a Zr solution phase dispersed in a matrix of two different intermetallic phases. The second alloy, Zr-12Fe-10Cu, did not produce a homogenous mixture and consisted of two distinct phase morphologies. The top half of the sample was Zr rich and contained Zr precipitates dispersed in a matrix of intermetallic compounds while the bottom half consisted solely of intermetallic compounds. The third alloy, Zr-12Fe-15Cu, was comprised of four different intermetallic phases three of which had the same apparent Zr_2(Fe,Cu) structure but had distinct phase morphologies based on the Backscatter Electron (BSE) images.

Upon determining the phase morphologies of each of the fabricated alloys Differential Scanning Calorimetry (DSC) and Thermal Gravimetric Analysis (TGA) were used to measure phase transformation and melting temperatures. Little difference was observed between the as-cast and annealed samples. The transitions shifted slightly to higher temperatures and the annealed Zr-12Fe-15Cu alloy only had two transitions compared to three seen in the as-cast samples. Slight changes were observed in the melting temperatures between the as-cast and annealed alloys. Zr-12Fe-5Cu had the largest melting temperature

[1] *All alloy designations are given in wt% unless otherwise noted*

(886.3°C) while Zr-12Fe-10Cu had the smallest melting temperature (870°C). The third alloy, Zr-12Fe-15Cu, had a melting point just below that of Zr-12Fe-5Cu at 882.7°C.

Light Flash Analysis (LFA) was implemented to determine the low temperature (20-260°C) thermal diffusivity values of each alloy. The as-cast measurements were more precise than the annealed samples, most likely the result of non-ideal sample integrity prior to loading. Each of the three alloys showed a linear increase in thermal diffusivity over the temperature range. Values for Zr-12Fe-5Cu ranged from 3.54 ± 0.06 mm^2/s to 4.42 ± 0.10 mm^2/s. The Zr-12Fe-10Cu alloy had maximum and minimum values of 4.19 ± 0.22 mm^2/s and 3.17 ± 0.16 mm^2/s, respectively. Lastly, Zr-12Fe-15Cu had the largest thermal diffusivity ranging from 3.52 ± 0.15 mm^2/s at 20°C to 4.64 ± 0.16 mm^2/s at 260°C. Overall, the data from the LFA measurements showed that the Zr-Fe-Cu alloy system had similar diffusivity values compared to other common reactor materials.

DEDICATION

To my wife and family, without your love and support I would not be where I am today.

ACKNOWLEDGMENTS

First and foremost I would like to express my deepest gratitude to my advisor Dr. Sean McDeavitt, who first introduced me to the world of materials, for the continued patience and support he's given to a young and inexperienced materials scientist. Without his experience and recommendations this would not have been possible. I would also like to thank my committee members, Dr. Lin Shao and Dr. Raymundo Arroyave, for their leadership and willingness to help me throughout this entire process.

I would also like to thank everyone at Lawrence Livermore National Lab for their continued funding in support of this project and especially Dr. Patrice Turchi and Dr. Joe McKeown for their encouragement and help throughout this assignment. I would also like to give my utmost appreciation to Dr. Ray Guillemette for his seemingly endless knowledge of electron microscopy and countless hours on the EMPA helping me understand what I was seeing.

I am eternally indebted to my first advisor and mentor, Dr. Samim Anghaie, who first gave me the chance to do research as a young undergraduate student and who first instilled in me the desire to perform research. I would also like to thank all of my colleagues at the University of Florida, without them I never would have made it to graduate school.

I am also immensely grateful for my friends and classmates at Texas A&M University, especially those in the FCML group, for their endless help both in class and in the lab. A special thanks to Sangjoon Ahn and Sandeep Irukuvarghula for their continued advice and friendship throughout this process.

My family and wife for whom this thesis is dedicated to, I give the greatest thanks. Without their love and support I never would have made it to where I am today.

And finally, I give all the glory to God, without whom nothing is possible. It is because of His grace that I was given the opportunity to complete this work.

NOMENCLATURE

BHT	Group B Annealed Samples
BWR	Boiling Water Reactor
CALPHAD	CALculation of PHAse Diagrams
CHT	Group C Annealed Samples
DSC	Differential Scanning Calorimetry
EDS	Energy Dispersive Spectroscopy
EPMA	Electron Probe Microanalyzer
FCCI	Fuel Clad Chemical Interaction
FCMI	Fuel Clad Mechanical Interaction
IMF	Inert Matrix Fuel
LFA	Light Flash Analysis
LLNL	Lawrence Livermore National Lab
LWR	Light Water Reactor
MRF	Materials Research Furnace
PIE	Post Irradiation Examination
PWR	Pressurized Water Reactor
SEM	Scanning Electron Microscope
TGA	Thermal Gravimetric Analysis
WDS	Wavelength Dispersive Spectroscopy

TABLE OF CONTENTS

Page

LIST OF FIGURES

Page

Page

Page

Page

Page

LIST OF TABLES

Page

Page

1. INTRODUCTION

1.1. Motivation

As of 2006, there were a total 435 nuclear power reactors operating around the globe providing roughly 15% of the world's electricity. [1] This number is projected to reach between 35% and 100% by the year 2030. [2] With today's global dependence on electricity it's paramount that we get the most out of our nuclear reactors. Presently, the current fleet of nuclear power reactors only uses a few percent of their fuel. Consequently with the growing need for more electricity, future generations of nuclear power plants will require greater use of their nuclear fuel. In other worlds, nuclear fuel must reach a higher burnup then what is currently being achieved. It takes approximately 20-25 years to develop and qualify new fuel which will inevitably spend only 1/5 of that time in a nuclear reactor. [3] One goal of advanced fuel research around the world is to develop an accelerated scientific methodology for the development of ultra-high burnup fuel that can withstand the microstructural changes induced by fission products and fuel to clad interactions.

How well a fuel can perform is determined by its ability to continue operating as originally designed. During a fuel's lifetime it is subjected to a harsh reactor environment that includes high temperatures and pressures in addition to high neutron irradiation fluence. Because of this extreme environment it will experience multiple degradation phenomena such as fission gas swelling, void migration due to thermal gradients, and fission product precipitation, all of which challenge its ability to perform and become more pronounced as burnup increases. Some phenomena will cause minor changes such as a small shift in the temperature gradient and power density across the fuel which will inevitably lead to large fluctuations across the entire core. Other phenomena can have a more severe impact resulting in cladding failure and the release of fission products into the coolant stream. All of these factors need to be considered in the development and design of advanced nuclear fuels in an effort to safely optimize fuel performance. These phenomena ultimately lead to contact of the fuel and cladding leading to fuel cladding chemical interaction (FCCI) and fuel cladding mechanical interaction (FCMI), which can inevitably result in cladding failure.

Over the past decades, the performance of standard low-burnup, low-utilization fuels has settled into a fairly well characterized challenge. In other words, the system works in its current configuration. However, the need to develop long-term sustainability and expansion of the nuclear fuel cycle and significant safety events such as the tsunami-induced challenges at the Fukushima-Daichi power plants are motivating the development of advanced nuclear energy systems and advanced nuclear fuels. Several novel concepts have been proposed and are being developed. One such fuel type, and the subject context for this thesis, is a metallic inert matrix nuclear fuel (IMF) developed at the A.A. Bochvar Institute in Russia. This fuel concept is comprised of metallic fuel microspheres coated with a Zr-based brazing alloy used as a matrix and thermal bonding agent to the cladding. [4] An IMF has the potential to be a suitable replacement to traditional PWR and BWR fuels as they offer increased thermal conductivity as well as potentially higher fuel densities, while offering an increased tolerance to fuel swelling and fuel clad interaction.

One promising feature of IMF dispersion type fuels is the ability to test each of the components (actinide fuel, metal matrix, and cladding) separately before irradiating the fuel as a whole. Work has been done by A. Savchenko, et al., at the A.A. Bochvar Institute to develop these fuels as well as well as a method for fuel fabrication. [5] In-pile testing of the IMF bundles has shown that the fuel coupled with a Zr matrix and stainless steel cladding performed well and is promising for both fast and thermal reactors. [6]

1.2. Project Overview and Objective

An ultra-high burn-up metallic inert matrix nuclear fuel concept is being characterized and evaluated by Lawrence Livermore National Laboratory and Texas A&M University based on a metal matrix fuel concept originally developed at the Bochvar Institute in Russia. The concept, as stated previously, comprises a dispersion of uranium metal microspheres in a Zr-based alloy matrix that provides thermal bonding between the fuel particles and the cladding material. This project, in conjunction with the work being done at LLNL, was designed to characterize the microstructural and thermophysical behavior of the Zr-(6-12)Fe-(6-12)Cu base alloys proposed as potential metal matrix. The Zr alloys, introduced by Savchenko, et al., are chemically active and have a strong tendency to wet

most surfaces when in liquid phase. The alloying additions suppress the high melting temperature of Zr from 1855°C down to below 900°C, which is needed for the fuel fabrication step but also limits the fuel's maximum operating temperature. This family of alloys has reported eutectic melting levels ranging from 850°C to 860°C. [4] The "low melting" and active wetting combined with low neutron cross sections makes these alloys a promising IMF candidate.

The objective of this study was to experimentally evaluate both the microstructural and thermophysical properties of the Zr-12Fe-(5,10, and 15)Cu alloys. The experiments and analyses described were divided into three main parts, nominally based on the analysis methods used to examine the alloys. The first utilized an Electron Probe Microanalyzer (EPMA) to characterize the metallurgical properties of the proposed matrix of alloys, as described in Section 3.1. Upon determining the phase morphologies of each of the fabricated alloys, the second part of the study utilized Differential Scanning Calorimetry (DSC) and Thermal Gravimetric Analysis (TGA) to measure the phase transformations and melting temperatures of the proposed alloys. The DSC-TGA measurements will go to complement the simulation studies being completed by Dr. Patrice Turchi et. al. at LLNL using CALPHAD. The third and final step was to use Light Flash Analysis (LFA) to determine the low temperature (20 to 260°C) thermal diffusivity values of each alloy. These low temperature measurements will act as a basis to examine the overall trend of the thermal diffusivity as a function of temperature and help to elaborate on the feasibility of these alloys as a metal matrix material.

This section provides a general overview of the project as well as a brief motivation to why advanced nuclear fuel research needs to be pursued and more specifically where this fuel design concept fits in the overall initiative to advance commercial nuclear fuel to higher and higher burnup. Section 2 gives a brief background of commercial nuclear fuel and the key phenomenon that limit its lifetime in a reactor. Additionally, Section 2 gives insight into the fuel concept developed at the Bochvar Institute and where the Zr-Fe-Cu alloys fit into the design. The experimental methods and analysis techniques are outlined and discussed in Section 3. Data obtained from each of the analysis techniques are presented in Section 4. Section 5 gives a detailed description and comparison of the acquired data with Section 6 giving a summary of the observed phenomena with suggestions to future works to be done.

2. BACKGROUND*

In order to discuss the nominal advantages of advanced nuclear fuel design, a broad understanding of the fundamental physical phenomena is needed. This section presents a summary of some of the relevant issues related to the experimental work completed for this thesis. Topics discussed in this section include: uranium dioxide fuel, the IMF fuel design concept by Savchenko et. al., as well as the Fe-Zr and Cu-Zr phase diagrams.

2.1. UO_2 Fuel

The United States is currently the largest producer of nuclear power in the world accounting for more than 30% of the world's nuclear energy. Within the US, nuclear energy accounts for over 19% of the total electrical output. [7] Currently, after the decommissioning of four nuclear generating stations, Crystal River Unit-3 in Florida, Kewaunee in Wisconsin, and San Onofre Units 2 & 3 in California, there are 100 reactors, 65 PWRs and 35 BWRs. Most of the reactors built in the US were constructed between 1967 and 1990 and fall under the general designation of "Generation II" reactors; these reactors currently operate using UO_2 as their fuel.

Uranium dioxide is a very stable and well understood compound and has several features that make it appealing for use in a nuclear reactor. The UO_2 crystal has a fluorite structure of the CaF_2 type. At beginning of life (BOL), UO_2 is manufactured to be as pure as possible; as such when it is loaded into the fuel bundles it is a single phase and has no phase transformations between ambient temperatures and melting. [8] Because of this, it has a highly symmetrical structure and experiences no anisotropic effects, a feature that plagues many other fuel designs, most notably uranium metal based fuels such as U-10Zr and U-20Pu-10Zr. [9] Even though UO_2 has been a mainstay for commercial reactors, there are several phenomena which affect its behavior under irradiation.

---

* *Part of this Section is reprinted from Springer Bull. Alloy. Phase Diagr., 9, 1988, 589, The Fe-Zr (Iron-Zirconium) System, D. Arias and J.P. Abriata, Fig. 1, Copyright 1988 by Springer US, with kind permission from Springer Science+Business Media B.V.*
Part of this Section is reprinted from Springer Bull. Alloy. Phase Diagr., 11, 1990, 453, Cu-Zr (Copper-Zirconium), D. Arias and J.P. Abriata, Fig. 1, Copyright 1990 by Springer-Verlag, with kind permission from Springer Science+Business Media B.V

The initial decreased loading density as a result of manufacturing (nominally 95% dense) results in an increased porosity which initially helps with fission gas retention and reduces swelling. However, the induced porosity also has several secondary effects, namely influencing the physical properties of the fuel pellet. For instance, initial porosity reduces the already low thermal conductivity values, which are discussed in more detail below. Physical properties are also greatly affected by the exact chemical composition of the initial pellets. Changes in the O/U ratio affect the composition of the fuel pellet, changing the physical properties, in particular those which rely on particle migration, such diffusion coefficients, in addition to the chemical behavior of the various fission productions. [8]

Beyond the initial physical and compositional properties of UO_2 that affect its performance additional changes that occur in the reactor during irradiation also affect its performance especially at high burnup. During its time in the core a fuel pellet undergoes extreme conditions. These conditions produce several phenomena that affect both the physical and chemical make-up of the fuel. On a microscopic level, restructuring of the fuel as a result of neutron irradiation plays a significant role in the overall fuel performance. Restructuring is the consequence of microscopic changes in the fuel structure resulting from nuclear reactions. In most instances, displaced atoms caused by neutron bombardment return to a semblance of their original lattice position, however, under significant neutron irradiation, some defects do not recombine and defect clusters begin to accumulate. Microstructural changes such as point defect clusters caused by radiation damage coupled with stresses caused by thermal gradients build up and result in macroscopic changes in the fuel. [10] In addition to build up in microscopic changes, macroscopic changes in the fuel are also the result of several factors including thermal expansion, cracking as a result of strain energy release, irradiation induced swelling, and FCMI. [11] Arguably the most limiting factor in how a fuel performs is the accumulation of fission products and build-up of fission gasses. Neutron absorption in uranium and decay of fission products results in the production of numerous nuclides which build up inside of the fuel pellet. A high burnup fuel pellet is depicted Figure 2-1. Typical features seen in a fuel pellet irradiated to at high burnup include cracking both axially and radially as well as a large central void that forms. Additionally, one can also see the dark rim around the outside of the fuel pellet which consists of the zone in which FCCI and FCMI are present. [12]

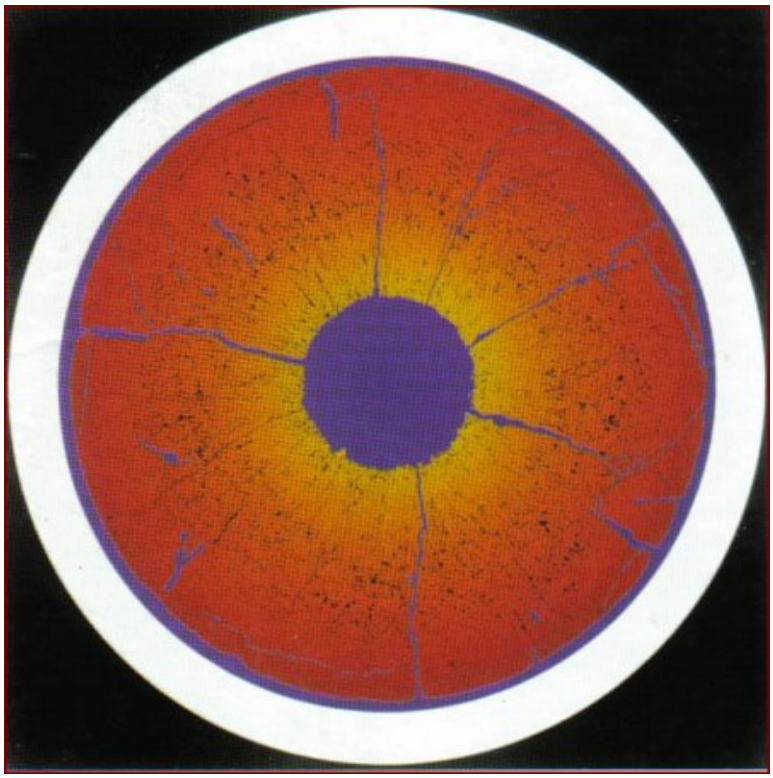

Figure 2-1: False color image of the radial cross section of a UO_2 fuel pellet irradiated to high burnup (Figure adopted from [12])

Even though several physical and chemical changes occur in UO_2 during irradiation, these phenomena affect all types, albeit by varying amounts, of fuel materials. One key feature inherent to UO_2 fuel, because it's a ceramic, is low thermal diffusivity, and consequently low thermal conductivity. Even though the melting temperature of pure UO_2 is extremely high, ranging from 3113 ± 20 K [13] to 3138 ±15 K [14], these temperatures can quickly be achieved during transients because of the poor thermal properties. Typical values for UO_2 at 95% theoretical density are shown in Figure 2-2.

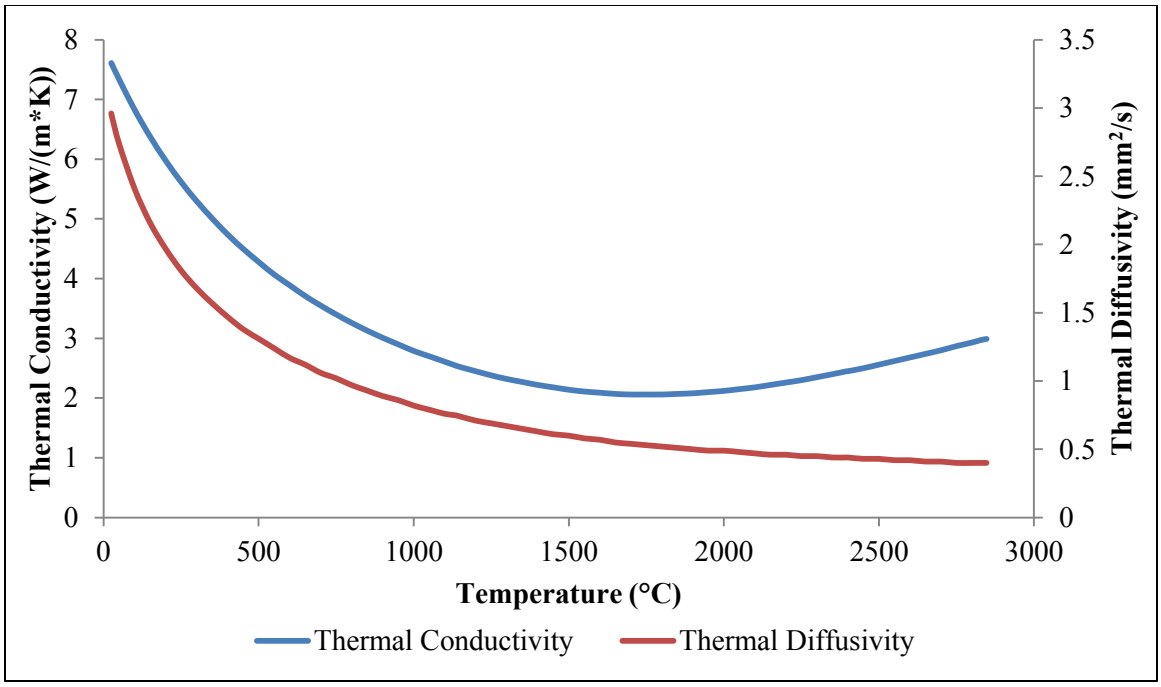

Figure 2-2: Thermal conductivity and thermal diffusivity of 95% TD UO_2 fuel.[2]

Extensive post irradiation examination (PIE) has been done in order to better understand the phenomena that occur during the fuel lifetime. [15] Additionally, efforts have been made to increase the thermal conductivity of UO_2 by doping it with additives such as SiC, diamond, and BeO. [16] Even with the research being done to improve conventional UO_2 fuel, advanced fuel research is still ongoing in order to develop a fuel that can withstand the harsh reactor environment for longer burnup by designing it to better withstand the phenomena that occur during irradiation.

2.2. Zr-Alloy Metal Matrix IMF Design Concept

The IMF design concept that provides the context for the research reported in this thesis was first developed by Savchenko et. al. at the A.A. Bachvar Institute in Russia. [6] This particular IMF concept is composed of three distinct parts: an actinide fuel meat, a zirconium brazing alloy, and a metal cladding. The zirconium brazing alloy makes this

[2] *Values taken from IAEA collection of thermophysical properties of reactor materials [37]*

particular IMF fuel design unique to other IMF dispersion fuels in existence, although several other concepts proposed by Savchenko et. al. have utilized aluminum as a matrix material. [17] Inert matrix fuels offer several key advantages over traditional light water fuel including an improved irradiation resistance along with an increased thermal conductivity which lowers the centerline fuel temperature during operation. This improves the fission product and gas retention, lowering the effective fuel swelling. The matrix braze alloy provides a thermal bond between the fuel and cladding without direct fuel-clad contact mitigating FCCI and FCMI effects. All of these features have the potential to allow the fuel to remain serviceable under both steady-state and transients conditions for burnups to up 100 MWd/kg. [6]

A schematic of the resulting fuel form is depicted in Figure 2-3. The fuel is composed of four distinct regions. The first is the uranium metal microspheres (fuel meat) depicted as orange circles of varying sizes. Next is the Zr matrix which coats both the microspheres as well as the interior wall of the cladding shown in both blue and green in the figure. The third region is the cladding shown in red, and finally the fourth "zone" is the open void shown in white within the inside of the cladding. The fuels are fabricated via capillary impregnation. Capillary impregnation is a two stage fabrication process that utilizes the capillary properties of the molten zirconium alloys. The first stage is vibroloading in which a powder mixture of coarse fuel microspheres and fine pre-alloyed matrix particles are loaded into the fuel cladding which is vibrated to achieve maximum powder packing density. The second stage is to anneal the powder mixture above the melting temperature of the Zr brazing alloy under a vacuum. During this process the fuel granules and cladding surface become coated by the actively wetting Zr alloy that fills the voids between the particles (leaving some open void space) and forming a metallurgical bond between the fuel and cladding. The resulting fuel structure consists of 3 separate components, not including the cladding, with volume fractions of: 55-65% fuel, 10-20% matrix, and 15-30% open void. [5]

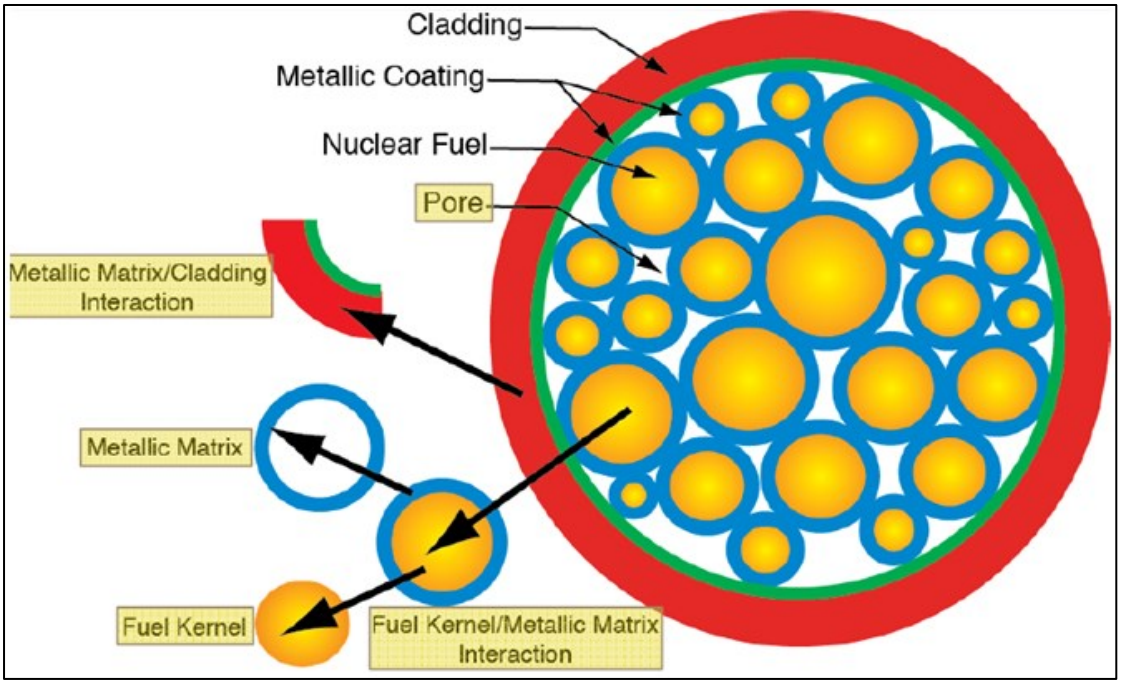

Figure 2-3: Schematic of the radial cross section of the fabricated fuel element. Figure adopted from [18]

One of the advantages of IMF as a replacement for the conventional UO_2 LWR fuel is the increased uranium content in the fuel meat which ultimately allows for longer burnup and greater use of the fuel. Novel fuel meat materials have been shown to increase the uranium content 15-50% compared to standard UO_2 pellets. [19] Several IMF concepts call for the use of aluminum as an inert matrix. Recent studies with miniplate testing have shown that high uranium content fuels are restricted by the matrix material. Under irradiation testing, RERTR-4, with high uranium content fuel, the aluminum matrix is only compatible up to 200°C. Above this temperature, the interdiffusion between the fuel and the aluminum causes a breakdown in the aluminum matrix decreasing the thermal conductivity of the system ultimately raising the temperature of the fuel. As fuel temperature increases, the rate of reaction between the aluminum matrix and fuel also increase, thus increasing fuel temperature even higher. This is particularly damaging in the case of U-Mo/Al fuels. [20]

Novel zirconium based alloys have been proposed by A.M. Savchenko et. al., as a metal matrix for high uranium content alloys. [21] The proposed alloys, shown in Table 2-1, have deep ternary and quaternary eutectics depressing the relatively high melting temperature

of pure Zr from 1855°C down to below 900°C. The low melting point is a necessity for the fabrication of the fuel by capillary impregnation. The potential brazing matrix alloys considered in Table 2-1 consist of several variations with Zr-Fe-Be and Zr-Fe-Cu forming the base alloys and Ti and Nb used as possible additions. Each of the alloys is made up of a large fraction of intermetallic phases and as a result exhibit higher temperature coefficient of linear expansion as well as thermal conductivity when compared to pure Zr. [6] Additionally, each of the alloys has demonstrated the same resistance to water and superheated steam inherent to zirconium alloys. [21] The inherent characteristics of the IMF form make it an ideal platform to develop an accelerated scientific methodology for advanced fuel. Each of the components can be separated and studied individually prior to studying their interactions as an integrated fuel form.

Table 2-1: Alloy composition and temperature data for Zr brazing alloys (Table adopted from A.M. Savchenko et. al.) [4]

Group	Alloy Composition (wt%)						Melting T (°C)	Impregnation T (°C)
	Zr	Ti	Fe	Cu	Be	Nb		
1	Base	5-20	4-7	1-3	1.5-2.5	-	690-720	780-810
2	Base	-	4-8	0.5-3.0	2-3	1-3	780-810	850-870
3	Base	5-10	8-14	8-14	-	-	810-820	880-900
4	Base	-	6-12	6-12	-	-	850-860	900-910

The Group 4 alloys in Table 2-1 were selected for examination in this study. Each of these alloys are interesting and may find applications in IMF systems, the Zr-Fe-Cu system was selected as the highest temperature system with the simplest elemental composition for practical handling. The high temperature was considered most relevant for applications in conventional LWR power producing systems where safety margins to minimize the risk of melting fuel are the most stringent. The lower temperature alloys could be used to enable IMF solutions for research reactors and lower power energy systems.

2.2.1. Zr-Fe and Zr-Cu Phase Diagrams

In order to better understand the phase morphology of the Zr-Fe-Cu alloy system it is useful to consider the two binary alloy systems between the primary component, Zr, and the minor alloying components. Because the nominal phase composition lies within the Zr rich portion of the ternary system, only the Zr-Fe and Zr-Cu phase systems are discussed below.

2.2.1.1. Zr-Fe Alloy System

The binary Zr-Fe alloy phase diagram is presented in Figure 2-4. This has several uncertainties evidenced by the existence of multiple variations to the binary phase diagrams in literature. [22] [23] [24] [25] Disagreement stems from the existence, or lack thereof, of various intermetallic phases such as $ZrFe_3$, Zr_4Fe, and Zr_3Fe. Figure 2-4 depicts the phase diagram presented by Arias and Abriata. [22] While not the focus of this study, it is noted that that thermodynamic analysis of phase equilibria is being carried in order to optimize the binary phase diagram. [24] Within the Zr rich zone (> 70wt%) four phases exist: αZr, βZr, Zr_3Fe, and Zr_2Fe. The solubility of Fe in αZr is nearly nonexistent (<0.16 at%), while Figure 2-4 shows a maximum solubility of 6.5 at% at 928°C in βZr. [26] The low solubility of Fe in both αZr and βZr leads to the formation of intermetallic compounds as witnessed by the relatively wide αZr + $FeZr_3$ zone seen in Figure 2-4.

2.2.1.2. Cu-Zr Alloy System

The binary Cu-Zr equilibrium phase diagram consists of ten phases, however in the Zr rich alloys only three phases are of interest. Figure 2-5 depicts the phase diagram developed by D. Arias and J.P.Abriata. [27] It's not surprising, given their relatively similar electronic configuration, electronegativity, and atomic size (as expected due to their proximity on position on the periodic table) that the Cu-Zr system is very similar to the Fe-Zr system. Zirconium rich alloys are dominated by the Zr_2Cu intermetallic phase. Like the Fe-Zr system, copper has very limited solubility in αZr (<0.46 wt%) and a maximum solubility

of 6.7 wt% in βZr at 995°C. The limited solubility Cu leads to the formation of intermediate compounds resulting in a relatively large αZr + Zr_2Cu zone.

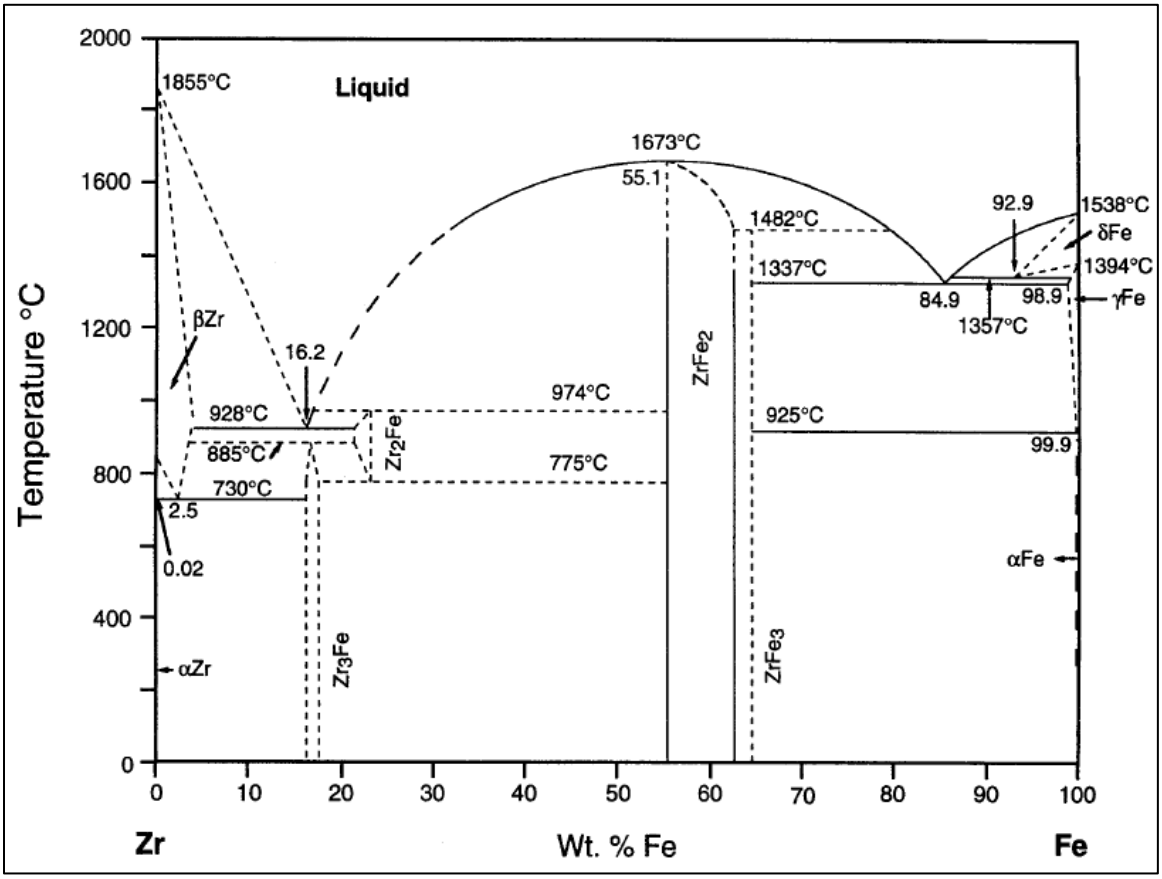

Figure 2-4: Fe-Zr binary phase diagram based on D. Arias and J.P. Abriata. [22]

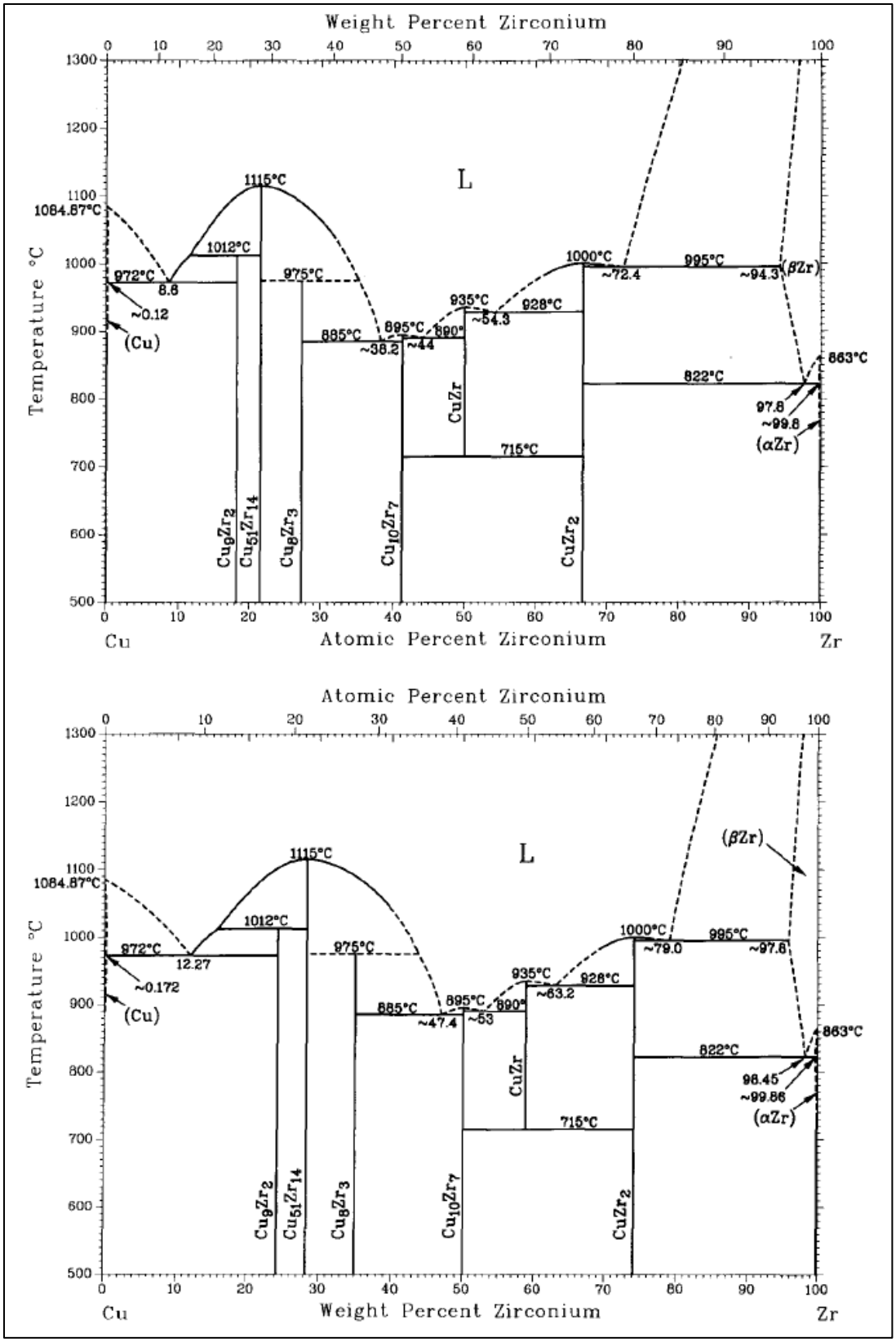

Figure 2-5: Cu-Zr binary phase diagram based on D. Arias and J.P. Abriata. [27]

3. EXPERIMENTAL

Various compositions of Zr-Fe-Cu alloys were melt-cast using materials research furnaces (MRF), Figure 3-1. Each of alloy groups was melt-cast under an inert atmosphere of flowing argon gas. The microstructural and thermophysical behavior of each of the alloys was then characterized for both as-cast and annealed samples. Three groups of alloys were melt-cast using the procedures outlined in the following sections. Group A was the initial melt-cast group, Group B was used for Differential Scanning Calorimetry (DSC) analysis, while Group C was used for Light Flash Analysis (LFA). All three groups where examined using the EPMA and the microstructural behaviors were characterized using energy dispersive spectroscopy (EDS) and wavelength dispersive spectroscopy (WDS).

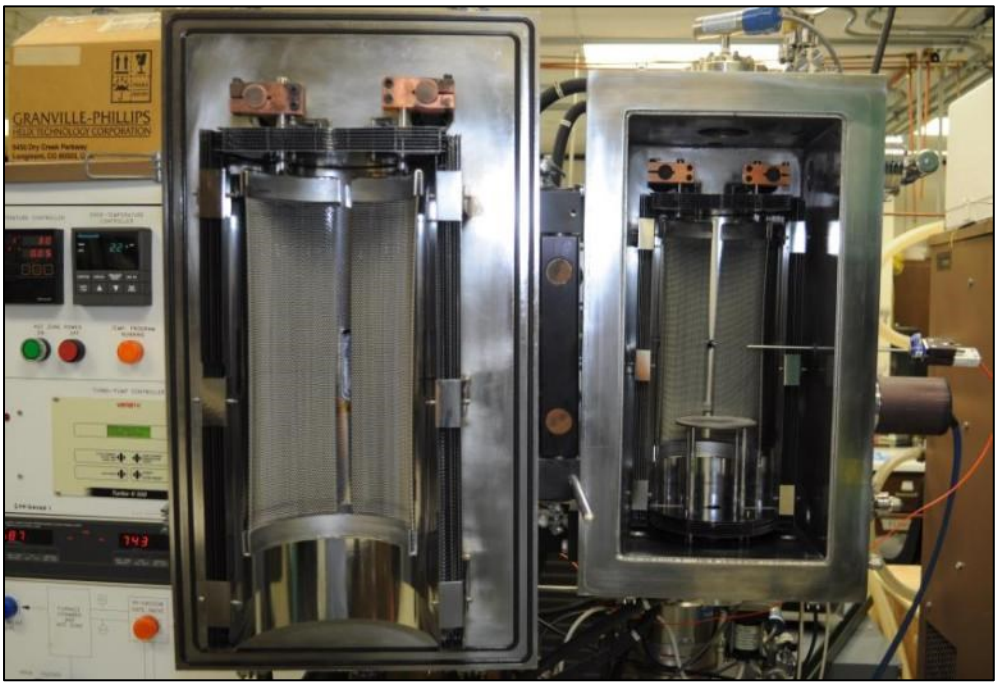

Figure 3-1: Photograph of the high temperature furnace in which all of the alloy groups were melt-cast

3.1. Fabrication of Alloy Groups

Pure metal source materials of iron and copper were procured from the Alfa Aesar Company while zirconium metal was used from the existing high purity crystal bar

zirconium in the lab. The Fe and Cu were ordered (100 g each) in slug form with dimensions 9.5 mm dia x 9.5 mm length and 6.35 mm dia x 12.7 mm length, respectively; the purity of the Fe was 99.95+% while the Cu was 99.9999% . Due to the high reactive nature of molten zirconium, yttrium oxide crucibles were procured to contain the melts for all casting.

Three specific variations of the Zr-Fe-Cu alloys were selected for fabrication. The alloys were selected based on the phase morphology diagram in Fig. 3-2 from Dr. P. Turchi (LLNL). It was decided to focus on 12 wt %Fe alloys with Cu variation that place the alloy systems into three distinct phase fields; this was done, in part to simplify the test matrix while the methods were being established. The blue box in Fig. 3-2 represents the original alloy matrix considered by A. Savchenko et. al. and outlined in Table 2-1. The three compositions indicated in Fig. 3-2 were expected to exhibit three distinct phase morphologies at 890°C, but their equilibrium room temperature structure was not evident from Fig. 3-2. The phases expected at high temperature are:

- Zr-12Fe-(6.5>)Cu: α-Zr solution phase (BCC) plus two intermetallic phases ($FeZr_3$ and $CuZr_2$)
- Zr-12Fe-(6.5-12.5)Cu: Three intermetallic phases ($FeZr_2$, $FeZr_3$, and $CuZr_2$)
- Zr-12Fe-(12.5<)Cu : Three intermetallic phases (Fe_2Zr, $FeZr_2$, $CuZr_2$)

The selection of the alloy composition was based, in part, on the composition/morphology diagram for Zr alloys with Cu-Fe additions shown in Fig. 3-2. This was one of several diagrams available and it only represented one isotherm; the intent was to cast alloys with distinct morphologies for characterization. The three alloys were nominally in distinct phase fields and should therefore exhibit modestly different properties. Both the Zr-12Fe-5Cu and Zr-12Fe-15Cu alloys were outside of the nominal composition space for the matrix under investigation, but were metallurgically interesting as the variations in copper moved the phase equilibrium into distinct morphology zones.

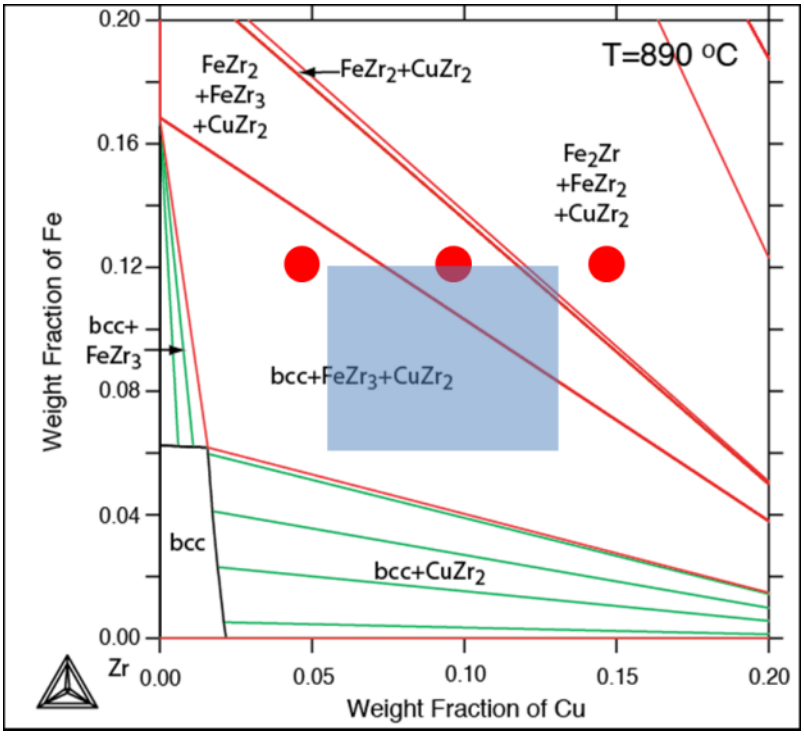

Figure 3-2: A phase morphology diagram for Zr-Fe-Cu alloys showing stable phases at a particular isotherm (890°C) for Cu-Fe composition "space" in a Zr base alloy (Figure courtesy of P. Turchi)

3.1.1. Group A

These initial alloy samples were produced by melt casting pure metal components. For this fabrication series, the target alloy compositions are listed in Table 3-1 and the actual measured masses of the metals charged into the melt crucibles are listed in Table 3-2.

Table 3-1: Target alloy compositions

SAMPLE	METAL WEIGHT PERCENT		
	Zr	Fe	Cu
1	83	12	5
2	80	12	8 (not 10)
3	73	12	15

Table 3-2: Initial alloy component masses before melting (Group A)

	(1) Zr-12Fe-5Cu		(2) Zr-12Fe-8Cu		(3) Zr-12Fe-15Cu	
	Mass (g)	Conc. (wt%)	Mass (g)	Conc. (wt%)	Mass (g)	Conc. (wt%).
Fe	2.1913	12.1	2.2107	12.1	2.3104	12.0
Cu	0.8921	4.9	1.5139	8.3	2.9019	15.0
Zr	15.0672	83.0	14.5538	79.6	14.1028	73.0
Total:	18.1497	100	18.278	100	19.3151	100

The casting was carried out with the maximum furnace temperature set to be 1600°C. The casting procedure was as follows:

1) The furnace chamber was placed under a vacuum and backfilled three times with argon gas to purge oxygen from the furnace chamber.
2) The furnace was controlled by a Honeywell DCP-200 which has a maximum heat up rate of 70°C/min, although a heat up rate of approximately 30-40°C/min was used.
3) The samples were heated to approximately 1600°C
4) The furnace was held at 1600°C for half an hour.
5) The furnace was then cooled back down to room temperature at a rate of 35°C/min.

The samples were left in the furnace over night to cool and were removed the next morning. A picture of the samples after they were removed from the yttria crucibles is shown in Fig. 3-3; the yttrium oxide had to be removed with a hammer since the alloys tightly bonded with the crucible wall. Dark (almost black) pieces of the crucible are visible clinging to the alloy samples. However, after the samples were polished (Figs. 3-4 to 3-6), they appeared to have homogenized completely, but there were some small casing voids present on each sample.

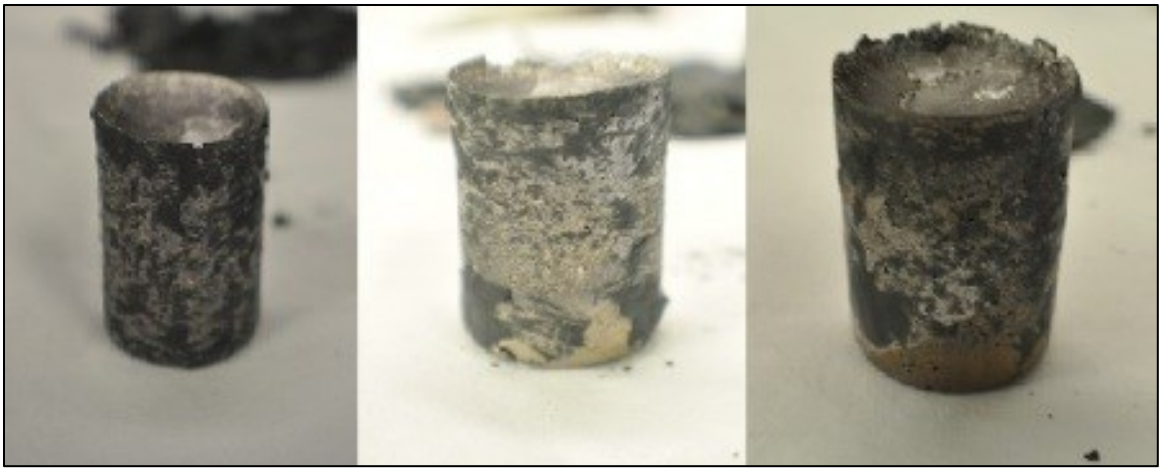

Figure 3-3: As cast samples: Zr-12Fe-5Cu (left), Zr-12Fe-8Cu (middle), Zr-12Fe-15Cu (right)

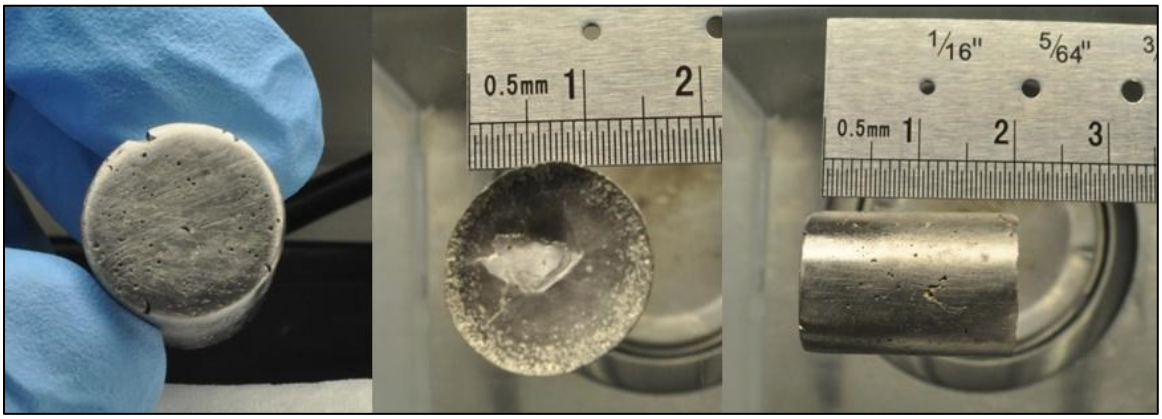

Figure 3-4: Photographs of polished Zr-12Fe-5Cu

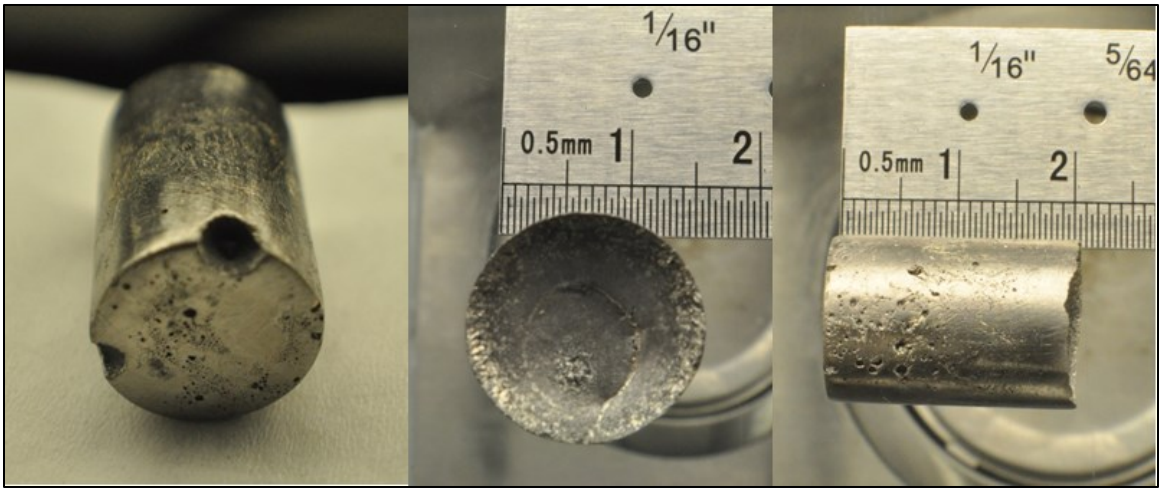

Figure 3-5: Photographs of polished Zr-12Fe-8Cu

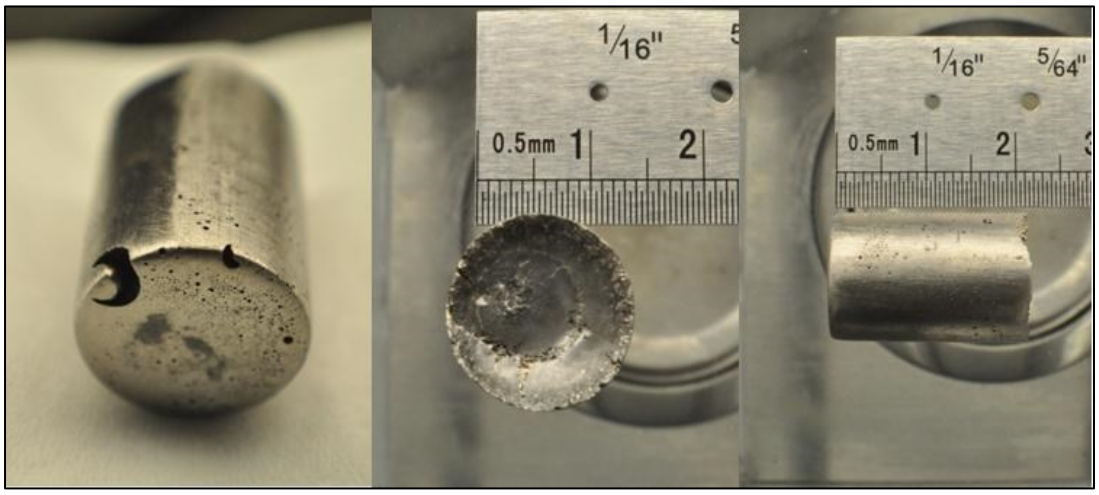

Figure 3-6: Photographs of polished Zr-12Fe-15Cu

3.1.2. Group B

It became evident through EMPA, as shown Section 4.1.1, that the alloys had not formed homogeneous structures and fresh castings were initiated with Zr-12Fe-(5,10,15)Cu compositions. For the second castings, the alloys were held in the molten state for a longer time to enable further mixing; the cast alloys were then cleaned, inverted, and re-melted. The copper composition of the mid-level alloy was changed from 8 wt % to 10 wt% because the

morphologies in the Zr-12Fe-5Cu and Zr-12Fe-8Cu samples were found to be nearly identical (see section 4.1).

These alloy samples were produced by melt casting pure metal components. For this fabrication series, the actual measured masses of the metals charged into the melt crucibles are listed in Table 3-3.

Table 3-3: Zr-12Fe-(5,10,15)Cu alloy component masses before melting (Group B)

	(1) ZR-12FE-5CU		(2) ZR-12FE-10CU		(3) ZR-12FE-15CU	
	Mass (g)	Conc. (wt%)	Mass (g)	Conc. (wt%)	Mass (g)	Conc. (wt%).
Fe	2.7332	12.27	2.7273	12.34	2.6298	12.15
Cu	1.1347	5.09	2.2464	10.17	3.2910	15.21
Zr	18.4073	82.64	17.1251	77.49	15.7198	72.64
Total:	22.2752	100	22.0988	100	21.6406	100

This casting was carried out in the same manner as the castings reported for Group A, except that the hold time at 1600°C was increased from 30 min to 75 min. After the initial casting, the alloys were cleaned and re-melted at 1200°C using the same procedure. The procedure for casting was as follows:

1) The furnace was evacuated and backfilled three times with argon gas.
2) Argon flow was initiated to provide an inert cover gas.
3) The furnace was heated at 35°C/min to 1600°C.
5) The furnace was held at 1600°C for 75 minutes.
6) The furnace was then cooled to room temperature at 35°C/min.

The samples were left in the furnace for approximately one hour, under a constant flow argon gas, to cool down to ambient temperature. Figs. 3-7 and 3-8 show the samples after the first melting after they were removed from their crucibles and after the surfaces were cleaned.

Figure 3-7: Photographs of the as-cast samples: Zr-12Fe-5Cu (left), Zr-12Fe-10Cu (middle), Zr-12Fe-15Cu (right)

Figure 3-8: Photographs of the alloy samples after removing the crucible remnants from the walls: Zr-12Fe-5Cu (left), Zr-12Fe-10Cu (middle), Zr-12Fe-15Cu (right)

Figure 3-9 was used to estimate the maximum temperature required for re-melting since it was desirable to minimize interactions with the yttria crucibles evident at 1600°C. From Fig. 3-9, it is apparent that all of the alloys should be completely molten at 1100°C, so the alloys were heated to 1200°C to be more certain. The samples were cast using the same procedure as before, with a maximum temperature of 1200°C. The as-cast samples from the second casting are pictured in Fig. 3-10.

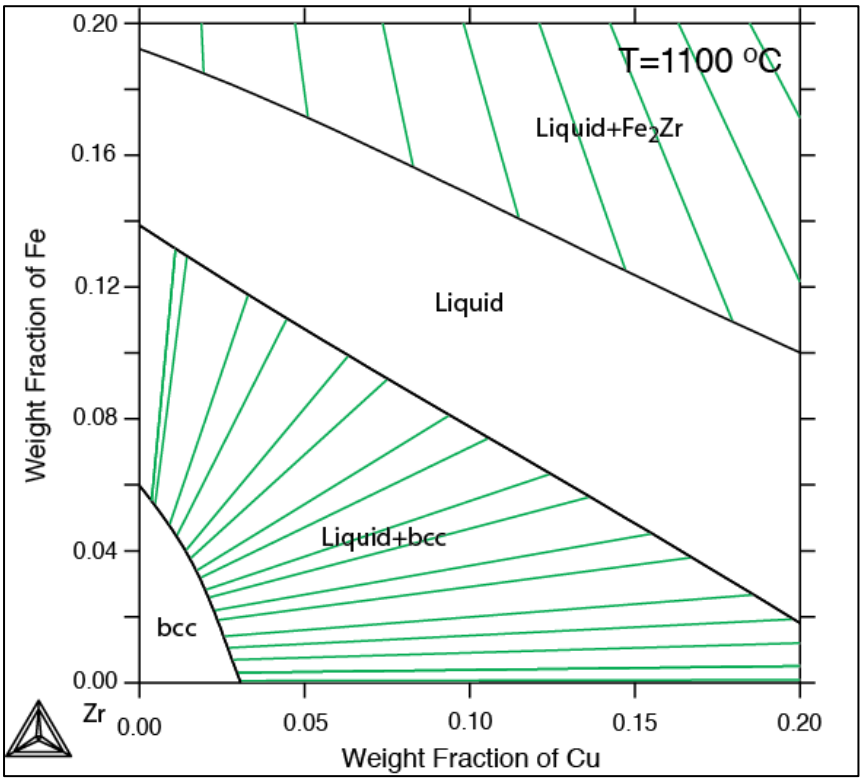

Figure 3-9: Phase morphology diagram for Zr-Fe-Cu alloys showing stable phases at a particular isotherm (1100°C) for Cu-Fe composition "space" in a Zr base alloy. (Figure courtesy of P. Turchi)

Figure 3-10: Photographs of the as-cast samples after second casting: Zr-12Fe-5Cu (left), Zr-12Fe-10Cu (middle), Zr-12Fe-15Cu (right).

3.1.3. Group C

A third casting was performed (Group C) in order to have the correct sample size to fit into the LFA. The samples were cast using the same method as Group B, that is, they were cast twice, inverting them for the second casting to insure uniformity in the casting. The actual measured masses of the metals placed into the melt crucibles are listed in Table 3-4. The as-cast samples, after each of their respective castings, are shown in Figs. 3-11 and 3-12. Each of the samples seemed to melt completely, expect for the first casting of Zr-12Fe-15Cu in which a small piece of copper didn't mix into the sample, however after the second casting it appeared that everything had mixed completely.

Table 3-4: Zr-12Fe-(5,10,15)Cu alloy component masses before melting (Group C)

	(1) Zr-12Fe-5Cu		(2) Zr-12Fe-10Cu		(3) Zr-12Fe-15Cu	
	Mass (g)	Conc. (wt%)	Mass (g)	Conc. (wt%)	Mass (g)	Conc. (wt%).
Fe	2.6875	12.1	2.6941	12.1	2.7180	12.5
Cu	1.0969	5.0	2.2467	10.2	3.3047	15.2
Zr	18.3950	82.9	17.1697	77.7	15.7252	72.3
Total:	22.1794	100	22.1105	100	21.7479	100

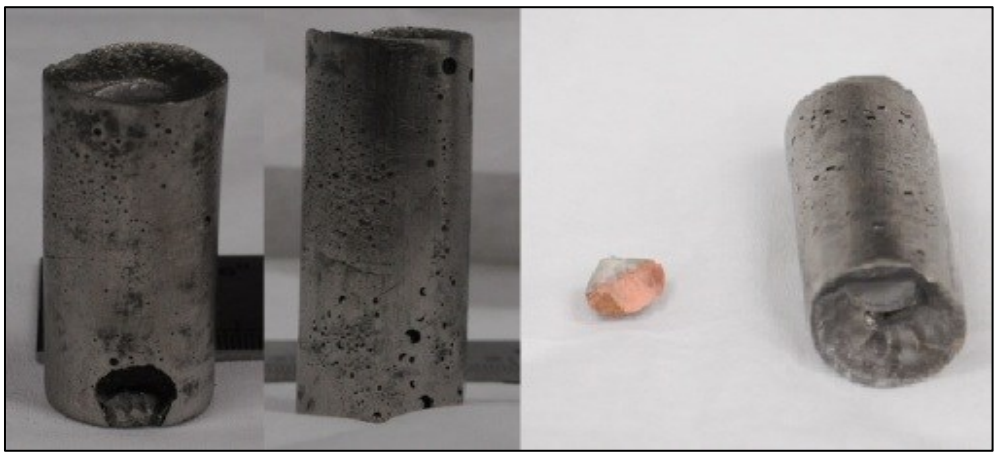

(a) (b) (c)

Figure 3-11: Photographs of the alloy samples after first casting: Zr-12Fe-5Cu (a), Zr-12Fe-10Cu (b), Zr-12Fe-15Cu (c)

(a) (b) (c)

Figure 3-12: Photographs of the alloy samples after second casting: Zr-12Fe-5Cu (a), Zr-12Fe-10Cu (b), Zr-12Fe-15Cu (c)

3.1.4. Annealing

To ensure homogeneity of the samples in preparation for DSC-TGA and LFA measurements, portions from each of the alloys from both Groups B and C were sectioned and prepared to be annealed. For the DSC-TGA measurements, to reduce compositional changes in the alloys, the melt cast slugs were sectioned radially into ~2 mm thick sections. From there a ~2 mm thick bar was cut by cutting the circular disk down the center twice. This bar was then sectioned in ~2 mm intervals, the results being a ~2x2x2 mm cube. This was done for each of the three Group B alloys. Because of the restrictions of the LFA sample holder, Group C alloys were sectioned radially with thicknesses ranging from 0.9 mm to 1.5 mm. Sectioned buttons from the top, middle, and bottom of the ingot were taken.

Sectioned buttons were then wrapped in tantalum foil, Group B only, and placed into half sealed cylindrical quartz tubes. The Group C samples would not fit into the quartz tubes with the tantalum foil wrapped around them, therefore, the Group C alloys were left bare and placed directly into the quartz tubes. The open end of the quartz tube was then placed into an Ultra-Torr fitting which was connected to a vacuum pump assembly. Once the quartz tubes reached the desired threshold (~10^{-3} Torr), the tube was heated using an acetylene torch and

manually twisted to be sealed. A representative picture of one of the quartz tubes is shown in Fig. 3-13.

Figure 3-13: Representative photograph of the quartz tubes after sealing.

The small concave dents which appear on one end of the quartz tube were intentionally created to determine whether or not the quartz tubs sealed properly. The low pressure inside of the tubes causes the quartz to concave in due to atmospheric pressure on the outside of the tube. Once each of the tubes was deemed to be correctly sealed, they were annealed at 700°C for 7 days[3]. The annealed samples had the same luster as the as-cast samples and appeared to not have oxidized. The Group C buttons did exhibit increased cracking which originated from the middle of the sample outward radially.

3.2. Electron Probe Microanalyzer

An EPMA, or more commonly electron microprobe, is an electron beam apparatus that bombards samples with electrons resulting in the release of both electrons and photons. The electron beam is produced typically from a heated tungsten filament. The beam is accelerated by high voltage and is focused by various magnetic lenses and apertures with an

[3] *Annealing temperature were determined using results collected from DSC-TGA analysis*

ending diameter of 0.1 to 1 μm. The energy of the electrons can be adjusted between 5 and 50 keV. Upon striking the surface of a sample, the electron beam produces several different products including: electrons, X-rays, and visible light. These products are then measured by various detectors each with a specific purpose. The imparted electron beam creates an interaction zone within the first couple microns of the surface of the sample from which the resulting products are emitted. The interaction zone resembles a tear drop and is approximately 1 μm in diameter. A representative sketch of the interaction zone is pictured in Fig. 3-14. Unlike a Scanning Electron Microscope (SEM) whose principle purpose is to produce images, an EPMA has several other features, many of which were utilized for data analysis.

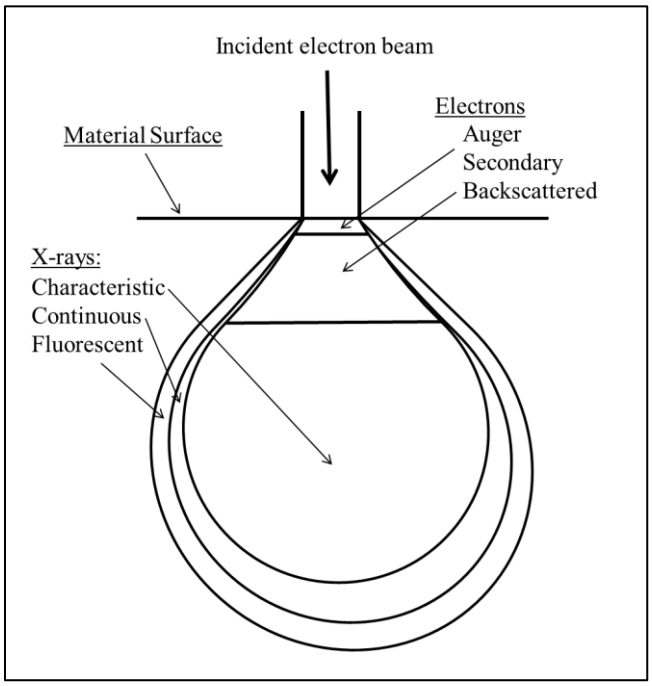

Figure 3-14: EPMA beam interaction zone and products (Figure not drawn to scale). Image adopted from [28]

3.2.1. Backscatter Electron Imaging

One of the products produced by the electron beam is backscatter electrons that are produced within the first 0.1 μm of the surface. Backscatter electrons are electrons that have had an elastic interaction with the specimen atoms and are reflected back toward the source. The intensity of backscattered electron that are produced are directly correlated to the mean atomic number of the incident material, high Z numbers produce more BSEs while low Z numbers produce less. The difference in intensity allows for the production of BSE images in gray scaled based off of the mean atomic number of the material. For all of the BSE images taken, the samples were run at 15keV and a 3-10 nA beam current. The lower the beam current the sharper the BSE images, however contrast is lost therefore an equal medium was found to produce sharp images while still allowing for enough contrast to distinguish between two similar phases.

3.2.2. Energy Dispersive and Wavelength Dispersive Spectroscopy

Almost all SEM systems are able to perform EDS, what makes EMPA systems unique is their ability to perform WDS. Both EDS and WDS use characteristic X-ray generated by the electron beam to determine the elemental make up of a particular sample. While EDS allows for qualitative elemental analysis giving relative abundances of particular elements, WDS can give quantitative elemental analysis by giving a numerical value for the atom and weight percent of a particular element.

The spectrometers of the WDS system consist of rotatable, oriented diffraction crystals coupled to gas-filled ionizing proportional counters. The detectors are arranged in a relationship in accordance to Bragg's Law (3.1)

$$n\lambda = 2d\sin(\theta) \tag{3.1}$$

where n is the order of diffraction, λ is the wavelength of the characteristic x-ray in Å, d is the atomic spacing of the diffracting crystal in Å, and θ is the angle of incidence. Incident X-

ray on the WDS detectors will either be constructive or destructive. Different crystals, crystal arrangements, and detectors are used based on the wavelength of the characteristic X-rays produced by the material. The two most common detector types are Li-drifted silicon detectors and high purity germanium detectors. WDS systems allow for better spatial resolution of the peaks by an order of magnitude. As stated previously, the main advantage of the EPMA is its ability to use the WDS detector to perform quantitative element analysis. This is done by taking scan of the sample in which a series of detectors are used to preferentially count the X-rays of the desired elements. A full description of the WDS system and a list of factors that affect the accuracy and precision of the analysis refer to the source reference. [28]

3.2.3. EPMA Sample Preparation

Alloy samples were prepared by sectioning the sample slugs using a diamond saw into small, less than 0.5 cm, pieces and were then mounted in an epoxy resin using a cylindrical plastic mold. The epoxy mounts were allowed to cure overnight until fully hardened. Several different polishing methods were used and were based off the original polishing method suggested by Buehler. The original procedure suggested by Buehler was modified slightly after various EPMA sessions by adding or subtracting steps or changing the lubricant used during polishing. Table 3-5 outlines the procedure used for each of the various alloy groups for both as-cast and annealed. Once polished, the samples were taken to the EPMA were they were sputtered with ~15 nm layer of carbon.

Table 3-5: Polishing procedure for each of the alloying groups

GROUP	LUBRICANT		GRIT SIZE						
	Water	Oil	240	320	600	800	3 μm	0.25 μm	0.06 μm
A	X	-	-	X	X	X	X	-	X
B	X	-	-	X	X	X	X	-	X
BHT*	X	-	-	X	X	X	X	X	X
C	-	X	X	X	X	X	X	-	X
CHT**	-	X	X	X	X	X	X	X	X

* BHT = Group B annealed alloys; ** CHT = Group C annealed alloys

3.3. Differential Scanning Calorimetry and Thermal Gravimetric Analysis

Phase transition temperatures for alloys between ambient and 1200°C were measured using a Netzsch STA 409 PC Luxx Simultaneous Thermal Analysis instrument coupled with Proteus Analysis Software. A schematic of the device used is shown in Fig. 3-15.

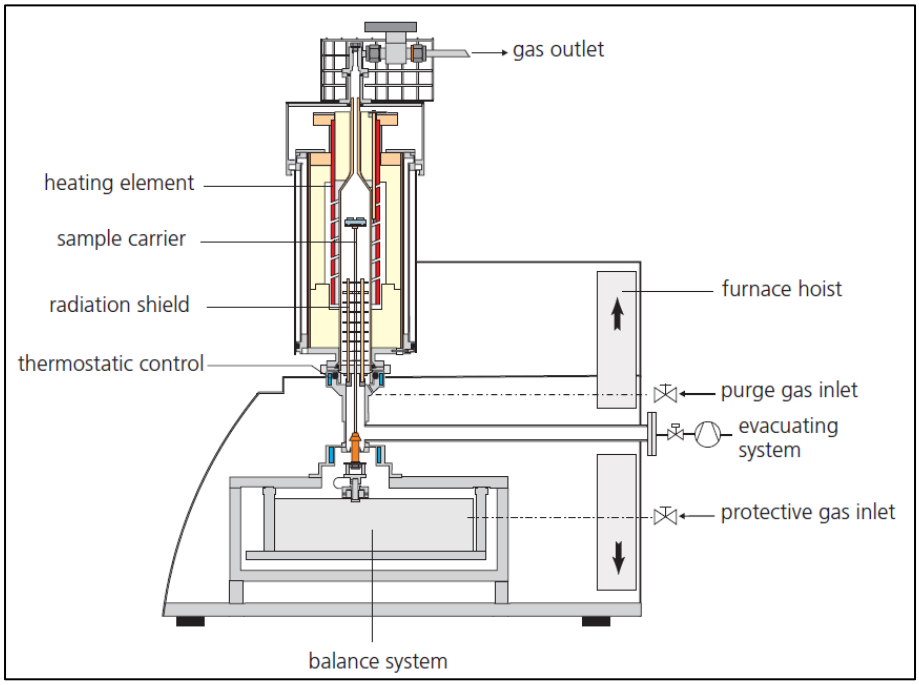

Figure 3-15: Schematic of STA-409PC Luxx (figure courtesy of Netzsch).

3.3.1. Baseline Measurements

The calibration file used during measurement was generated previously by Sangjoon Ahn. The standards used for the calibration file included, indium (In), tin (Sn), bismuth (Bi), zinc (Zn), aluminum (Al), silver (Ag), and gold (Au), supplied by the DSC manufacturer Baseline measurements were performed prior to sample measurements each time a new crucible was used. This was done by placing an empty alumina crucible of known mass in with an empty reference crucible of known mass. A correction file was then run with both

crucibles empty. Following the baseline measurement, a sample plus correction measurement was run with the desired sample placed in the sample crucible leaving the reference crucible empty. All parameters, e.g. temperature ramp rate, purge gas, purge gas flow rate, vacuum and backfilled times, were identical for both the baseline and sample measurements.

3.3.2. DSC-TGA Sample Preparation

Samples were cut into approximately 3x3 mm squares of varying thickness. Because a diamond saw was used to section the samples, the thickness and shape of each of the samples varied. Each sample measured weighed between 30 to 100 mg. In effort to avoid compositional changes between measured samples, each of the buttons was sectioned from a bar which was cut from the same radial section of each of the alloys. Each radial section was taken from the top half of each of the slugs. Because each of the alloys, namely the Zr-12Fe-5Cu and Zr-12Fe-10Cu alloys, were brittle, during sectioning, many of the samples had notches on one end making them uneven. Medium grit SiC paper was used to sand away each of these notches to ensure that each sample was flat to certify that it made intimate contact with the bottom of the measurement crucible. This limited contact with the purge gas, reducing the oxidation, thus increasing the accuracy of the measurements. Samples were then loaded into the bottom of the alumina crucible covered with a lid. The crucible was then placed on the DSC-TGA measurement head and the furnace was closed, as pictured in Fig. 3-15.

3.3.3. Sample Measurements

Once loaded, the furnace chamber was evacuated with a roughing pump and then backfilled with argon gas. This was done twice to ensure that most of the oxygen within the furnace chamber was evacuated. An argon purge and cover gas flow rate of 50 mL/min was used. In order to reduce the effects of oxidation at undesirable temperatures, a furnace ramp rate of 50 °C/min[4] was used from 25 to 690°C and then was decreased to 5 °C/min from

[4] *50 °C/min is the maximum ramp rate of the STA-409PC Luxx as stated in the manual*

690°C to 1200°C as per the calibration file. Mass increase due to oxidation was recorded using TGA along with the DSC curve. For measurements in which the oxidation was too high (~ 5% mass increase), the entire measurement was thrown out and a new sample was prepared and measured. Only the heating curve was considered during analysis due to hysteresis. [29] Sample measurements were run for each alloy until two identical heating curves were produced, therefore a minimum of three measurements were taken for each alloy with a maximum of six taken for some alloys.

3.4. Light Flash Analysis

Thermal diffusivity was measured between 20 and 260°C using a Netzsch Light Flash Analyzer (LFA) 447 NanoFlash Light Flash System coupled with Proteus Thermal Analysis Software. A schematic of the device used is shown in Figure 3-16.

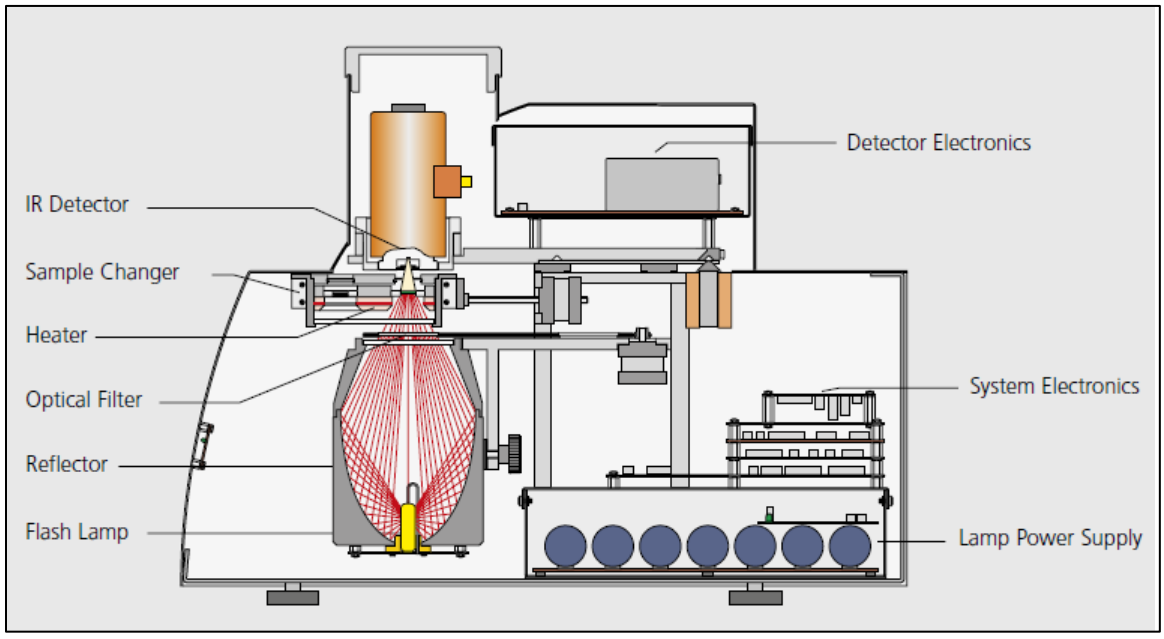

Figure 3-16: Schematic of LFA 447 NanoFlash Light Flash System (Figure courtesy of Netzsch).

3.4.1. LFA Sample Preparation

The LFA system uses sample holders which restricted the size and shape of the samples. Samples were cut from different sections of the Group C alloys, relative to one another, of the alloy slug. Each alloy was represented by a top, middle, and bottom of the ingot where possible. The nomenclature used for each section (top, middle, and bottom) only refers the relative position of the section within the alloy slug and is not indicative of the phase morphology. The samples were cut and ground to 1 to 1.6 mm thick depending on the sample. Ideally, sample thickness is based on thermal conductivity of the samples, however, since the thermal conductivity of the samples was not known and there was a limited amount of sample, button thickness was chosen in order to optimize the amount of samples sectioned while still maintaining sample integrity. The sample diameters ranged from 12.0 to 12.4 mm. The samples were then polished very lightly using fine grit SiC paper (400 Grit) in order to remove any notches as the result of sectioning the samples.

3.4.2. LFA Sample Measurement

Light flash analysis is a very well-known flash method. The basic concept is that a sample is heated to a desired temperature, once the sample is in thermal equilibrium with the system the front side of the sample is heated with a short light pulse by a xenon lamp (hence the name Light instead of Laser in the LFA acronym). The light is directed to the sample through a series of reflectors as shown in Figure 3-16. An infrared sensor is then used to measure the temperature change on the opposing side of the parallel sample as a function of time. The thermal diffusivity is then calculated using the half-time method given by Equation 3.2. [30]

$$\alpha = 0.1388 \times \frac{d^2}{t_{\frac{1}{2}}} \tag{3.2}$$

where α is the thermal diffusivity, d is the sample thickness, and $t_{1/2}$ is the time to reach half the maximum temperature. The system takes into consideration radial and facial heat losses as well as finite pulse effects and uses mathematical regression routines to adjust for these effects.

Measurements were taken from 20 to 260°C in increments of 10°C. The system first took a series of shots to optimize the detector signal as shown in Figure 3-17. Once an optimized signal is detected, the system took five shots at each of the temperature increments. The average of these five values, throwing out any outliers, was recorded. The results of this analysis are documented in Section 4.3.

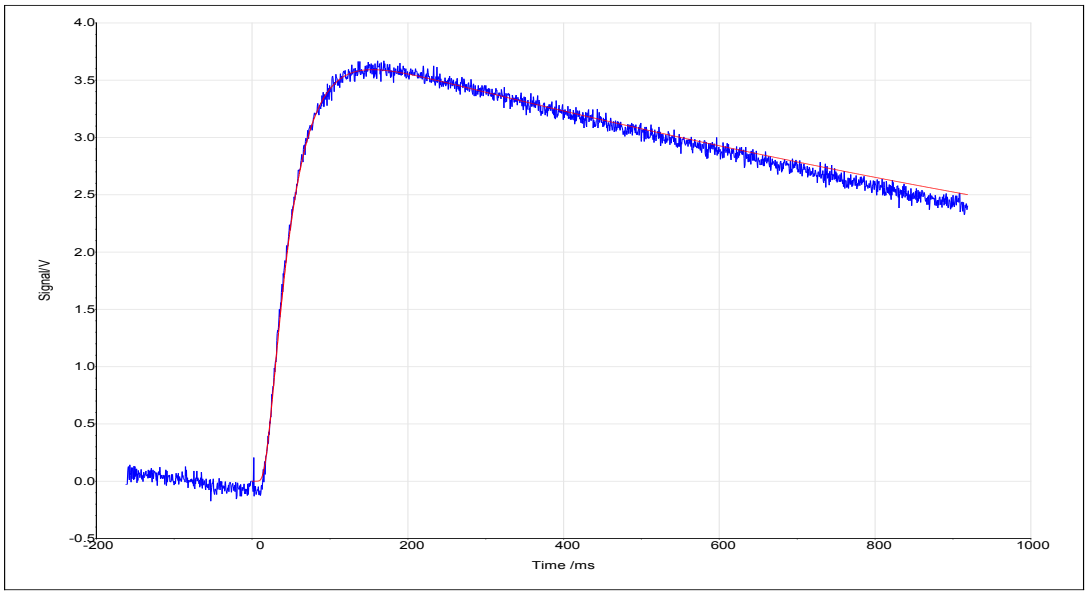

Figure 3-17: Representative detector signal where the y-axis is Signal (V) and the x-axis is time (ms).

4. RESULTS

Experimental data are shown in this section which is composed of three sections corresponding to the three different analytical methods used: EPMA, DSC-TGA, and LFA. Section 4.1 presents all of the EPMA results showing the phase morphologies of each of the three alloys for each of the three groups for both as-cast and annealed (Groups B and C only) for a total of 15 sets of EPMA results. Section 4.2 presents the DSC-TGA results from the Group B samples used to determine the onset of phase transformations as well as the melting temperatures of both the as-cast and annealed alloys. Finally, Section 4.3 presents the LFA data from the Group C alloys for both as-cast and annealed. Table 4-1 gives a brief summary of each of the methods used for each of the alloying groups.

Table 4-1: Summary of experimental methods used: X denotes method was used

	METHOD		
	EPMA	DSC-TGA	LFA
Group A	X	-	-
Group B	X	X	-
Group C	X	-	X

4.1. Microstructure of As-cast and Annealed Zr-Fe-Cu Alloys[56]

The figures in the following sections present BSE images and low magnification "optical scans" from the electron microprobe. The marker (+) in each of the images represents the general position for the subsequent BSE images taken at higher magnification. The radial section was cut from the bottom half of the sample while the axial section was cut from the top half of the samples. This was done to determine whether the samples morphologies were uniform.

[5] *All WDS values presented in this section are the result of individual analyzes.*
[6] *The apparent structures listed in this section are solely based on the atom percent obtained during WDS analysis. The actual phase structures were not characterized by more precise methods.*

4.1.1. Group A Alloys (Method Development Alloys)

4.1.1.1. Zr-12Fe-5Cu Alloy

Images from the axial and radial sections of the Zr-12Fe-5Cu alloy are presented in Figs. 4-1 to 4-3. The images were recorded at nominal magnifications of 90x, 300x, and 1000x and WDS was completed to determine nominal phase compositions. Table 4-2 summarizes the WDS data from the axial sample in Fig. 4-2 and Table 4-3 summarizes the WDS data from the radial sample in Fig. 4-3. It is notable that the sectioned alloy exhibited multiple cracks as a result of both sectioning and polishing indicating that the alloy is brittle.

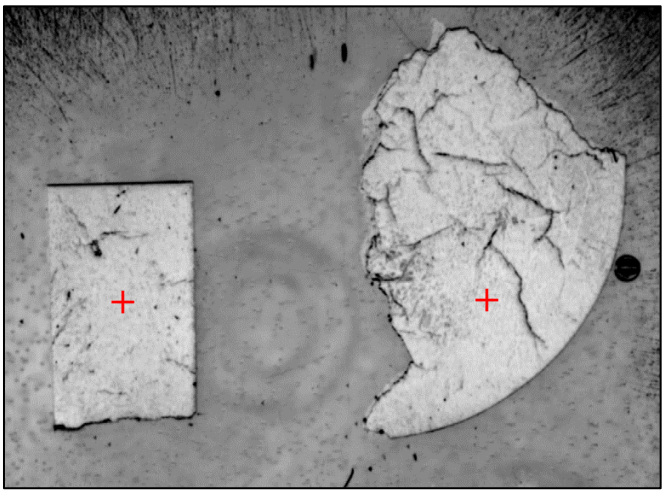

Figure 4-1: Optical scan of the Zr-12Fe-5Cu alloy: axial (left) and radial (right).

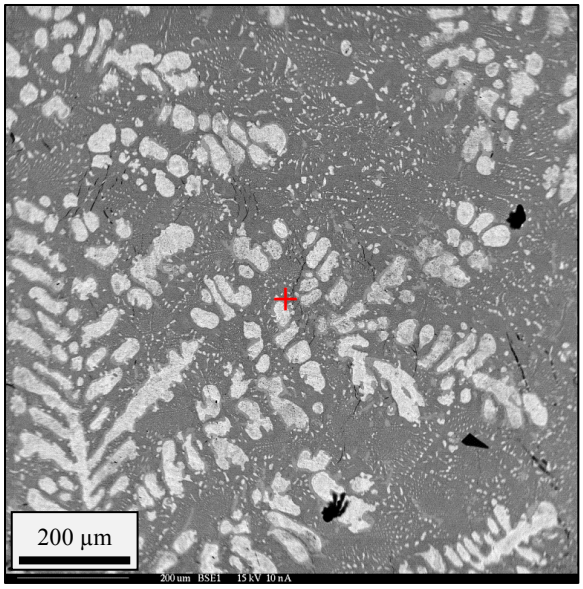

(a) Magnification = ~90x

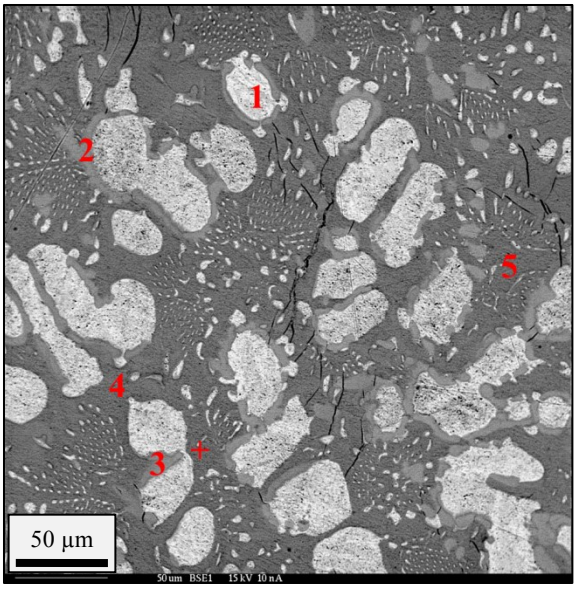

(b) Magnification = ~300x

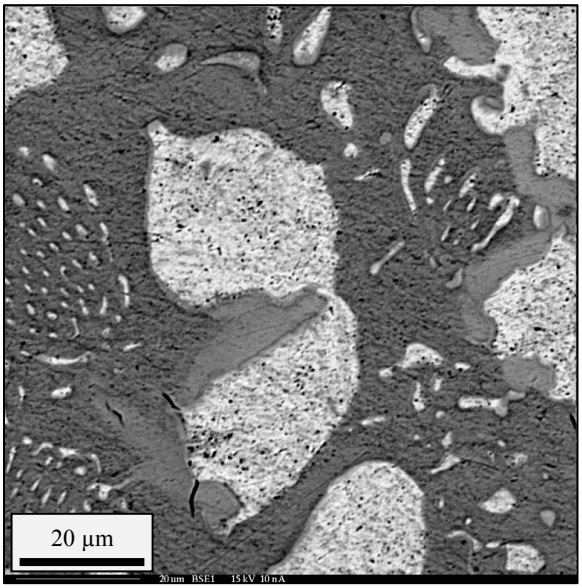

(c) Magnification = ~1000x

Figure 4-2: Backscattered electron images from the *axial* slice of the Group A Zr-12Fe-5Cu alloy: (a) 90x, (b) 300x, and (c) 1000x.

Table 4-2: Phase composition from WDS for Group A Zr-12Fe-5Cu (axial).

SPOT (FIG. 4-2B)	COLOR DESCRIPTION	ATOM PERCENT			WEIGHT PERCENT			
		Fe	Cu	Zr	Fe	Cu	Zr	Total
1	White	0.32	0.24	99.45	0.19	0.16	99.20	99.55
2	Light Gray	20.57	4.05	75.38	13.86	3.11	82.98	99.95
3	Light Gray	20.53	4.41	75.05	13.78	3.37	82.26	99.40
4	Bulk Gray	25.73	7.24	67.03	17.99	5.76	76.55	100.29
5	Bulk Gray	25.95	7.16	66.90	18.03	5.66	75.92	99.60

From Table 4-2 and Fig. 4-2 it was apparent that the 3 phases observed in the axial images corresponded well to the following:

SPOT 1: Zr solution phase with limited solubility for Fe and Cu

SPOTS 2-3: Apparent Zr_3M intermetallic (M = Fe and Cu)

SPOTS 3-4: Apparent Zr_2M intermetallic (M = Fe and Cu)

Table 4-3: Phase composition from WDS for Group A Zr-12Fe-5Cu (radial).

SPOT (FIG. 4-3B)	COLOR DESCRIPTION	ATOM PERCENT			WEIGHT PERCENT			
		Fe	Cu	Zr	Fe	Cu	Zr	Total
1	White	2.72	2.16	95.12	1.72	1.56	98.32	101.60
2	White	7.02	3.25	89.74	4.54	2.39	94.85	101.78
3	White (Light)	3.75	2.10	94.15	2.39	1.53	98.01	101.92
4	White (Dark)	3.45	2.15	94.40	2.19	1.56	97.87	101.62
5	Light Gray	20.82	3.71	75.47	14.19	2.88	84.02	101.09
6	Light Gray	20.64	3.67	75.69	14.06	2.85	84.24	101.15
7	Gray	2.51	2.16	95.33	1.55	1.52	96.03	99.09
8	Gray	0.73	1.61	97.66	0.44	1.11	96.94	98.49
9	Gray	1.79	1.92	96.29	1.10	1.34	96.51	98.95
10	Bulk Gray	24.21	8.55	67.25	17.20	6.91	78.03	102.14
11	Bulk Gray	22.97	9.80	67.23	16.30	7.91	77.91	102.12

From Table 4-3 and Fig. 4-3 it was apparent that the 3 phases observed in the radial images corresponded well to the following:

SPOTS 1-4 & 7-9: Zr solution phase with limited solubility for Fe and Cu

SPOT 5-6: Apparent Zr_3M intermetallic (M = Fe and Cu)

SPOTS 10-11: Apparent Zr_2M intermetallic (M = Fe and Cu)

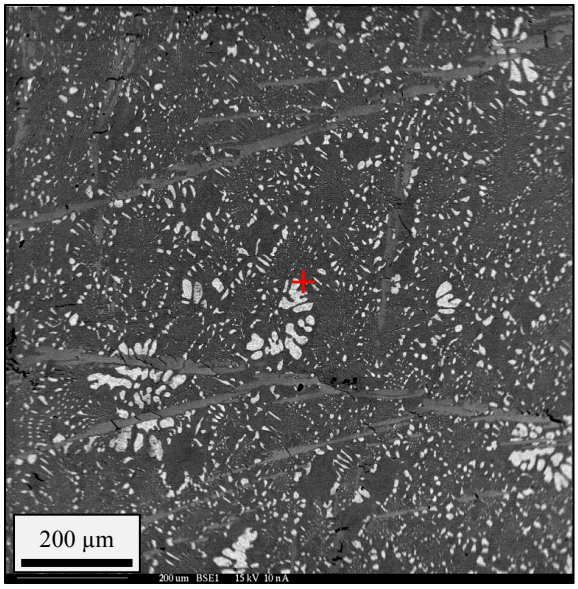

(a) Magnification = ~90x

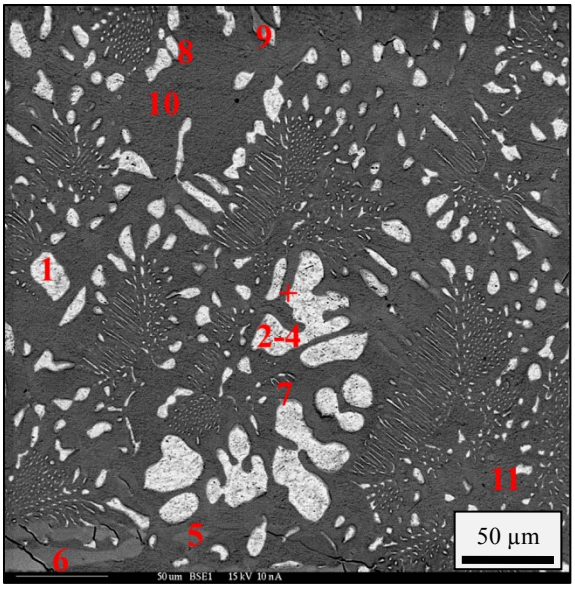

(b) Magnification = ~300x

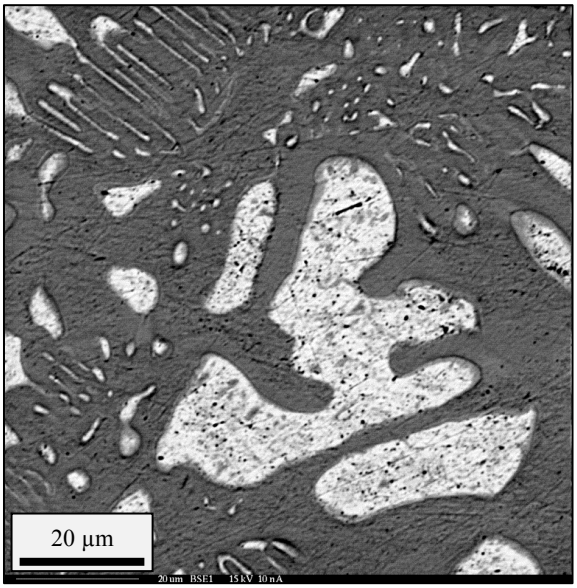

(c) Magnification = ~1000x

Figure 4-3: Backscattered electron images from the *radial* slice of the Group A Zr-12Fe-5Cu alloy: (a) 90x, (b) 300x, and (c) 1000x.

From the WDS results as well as the BSE images from Figs. 4-2 and 4-3, it is apparent that homogenous mixing of the alloying elements was obtained. There were three apparent phases in each section. During characterization, it was suspected that a fourth gray phase was also present. Surrounding the islands of zirconium precipitates was a dissimilar

phase evident due to size and contrast differences, but the WDS data in Tables 4-2 and 4-3 indicates that the both bright phases and surrounding grey phase were essentially identical in composition. This feature was seen in both in axial and radial sections, however it is much more prevalent in the radial section. Further analysis showed that the gray phases (Spots 7-9) were the result of rounding of the Zr precipitates thus lowering the intensity of the electron beam thus darkening then edges. The Zr precipitates were dispersed in a intermetallic matrix with an apparent Zr_2(Fe.Cu) structure. Additionally, a second intermetallic phase formed. In the axial section it formed exclusively around the Zr islands, however in the radial section it formed long strands through the bulk matrix phases. Further, there was a slight difference in the morphologies of the bright zirconium-rich phases (coarse in Fig. 4-2a and fine in Fig. 4-3a).

4.1.1.2. Zr-12Fe-8Cu Alloy

Images from the axial and radial sections of the Zr-12Fe-8Cu alloy are presented in Figs. 4-4 to 4-6. The images were recorded at nominal magnifications of 90x, 300x, and 1000x and WDS was completed to determine nominal phase compositions. Table 4-4 summarizes the WDS data from the axial sample in Fig. 4-5 and Table 4-5 summarizes the WDS data from the radial sample in Fig. 4-6. Once again it is notable that the sectioned alloy exhibited cracks, but fewer than those evident in the previous alloy.

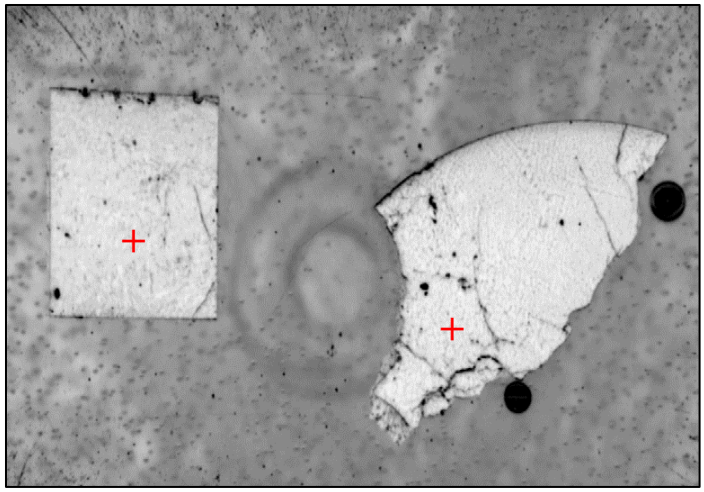

Figure 4-4: Optical scan of the Zr-12Fe-8Cu alloy: axial (left) and radial (right).

It is evident from the BSE images that there was a large variation between the axial and radial sections. The most apparent was the discrepancy in Zr content between the axial and radial portions examined. Large Zr precipitates were present in the axial (top) section while there appeared to be none present in the radial (bottom) section. The bright spots in Fig. 4-6b may indicate a very minor presence of the Zr solution phase with limited solubility for Fe and Cu, however due to limitations in the beam size the features were too small to analyze using WDS. While the axial section appeared to exhibit features similar to that in Zr-12Fe-5Cu (i.e. Zr precipitates in a matrix of intermetallics), the radial section consisted wholly of intermetallics with variations in all three elements with the minor presence of Zr precipitates. It appears that the matrix phases observed in the radial section had a finer structure, possibly the result of the decomposition of another phase, however the structures were far too small to analyze, and thus 5-10 μm averages were taken. Because averages were taken of seemingly heterogeneous structures, the results of the WDS analysis may not be representative of the actual elemental composition due to interference from competing phases. The large black floral-like structures are yttria inclusion as the result of casting.

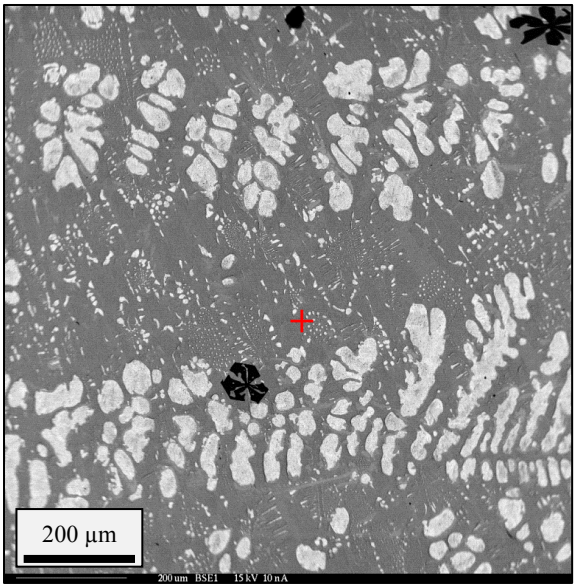

(a) Magnification = ~90x

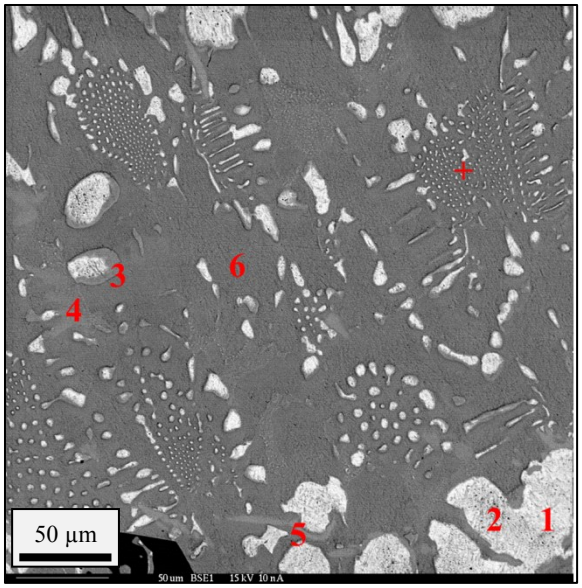

(b) Magnification = ~300x

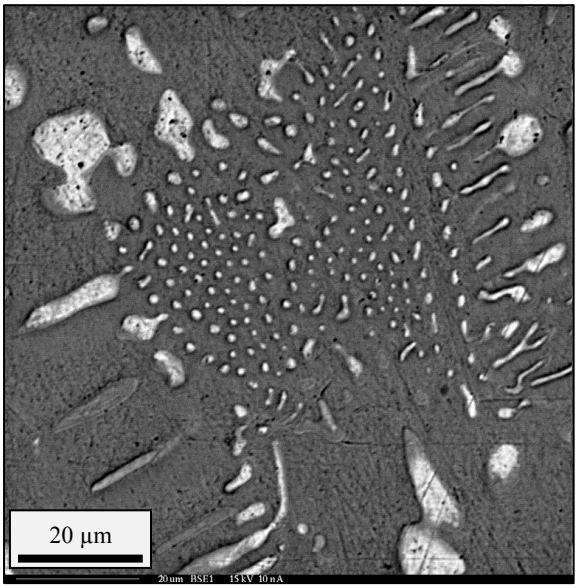

(c) Magnification = ~1000x

Figure 4-5: Backscattered electron images from the axial slice of the Group A Zr-12Fe-8Cu alloy: (a) 90x, (b) 300x, and (c) 1000x.

Table 4-4: Phase composition from WDS for Group A Zr-12Fe-8Cu (axial).

SPOT (FIG. 4-5B)	COLOR DESCRIPTION	ATOM PERCENT			WEIGHT PERCENT			
		Fe	Cu	Zr	Fe	Cu	Zr	Total
1	White	0.16	0.75	99.09	0.10	0.52	99.56	100.18
2	White	4.04	2.53	93.43	2.53	1.81	95.60	99.93
3	Gray	1.82	2.40	95.78	1.11	1.67	95.35	98.12
4	Light Gray	19.18	5.71	75.11	12.97	4.39	82.98	100.34
5	Light Gray	18.56	6.24	75.19	12.56	4.81	83.09	100.46
6	Bulk Gray	22.67	10.47	66.86	15.91	8.36	76.63	100.89

From Table 4-4 and Fig. 4-5 it was apparent that the 3 phases observed in the axial images corresponded well to the following:

SPOTS 1-3: Zr solution phase with limited solubility for Fe and Cu

SPOTS 4-5: Apparent Zr_3M intermetallic (M = Fe and Cu)

SPOTS 6: Apparent Zr_2M intermetallic (M = Fe and Cu)

Table 4-5: Phase composition from WDS for Group A Zr-12Fe-8Cu (radial).

SPOT (FIG. 4-6B)	COLOR DESCRIPTION	ATOM PERCENT			WEIGHT PERCENT			
		Fe	Cu	Zr	Fe	Cu	Zr	Total
1	Light Gray	12.88	14.28	72.84	8.71	10.98	80.41	100.10
2	Gray	17.14	12.47	70.40	11.66	9.65	78.25	99.57
3	Bulk Gray	23.12	10.01	66.87	16.13	7.95	76.22	100.30
4	Bulk Gray	23.02	10.28	66.70	16.20	8.23	76.67	101.10
5	Black Spot	21.27	11.71	67.03	14.79	9.27	76.17	100.23

From Table 4-5 and Fig. 4-6 it was apparent that the radial section selected has a different morphology which corresponded well to the following:

SPOT 1: Apparent Zr_3M intermetallic (M = Fe and Cu)

SPOT 2: Apparent Zr_3M intermetallic (M = Fe and Cu)

SPOTS 3-5: Apparent Zr_2M intermetallic (M = Fe and Cu)

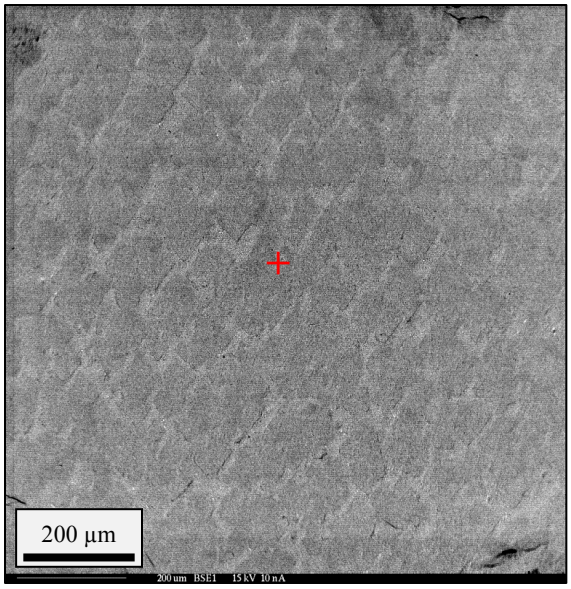

(a) Magnification = ~90x

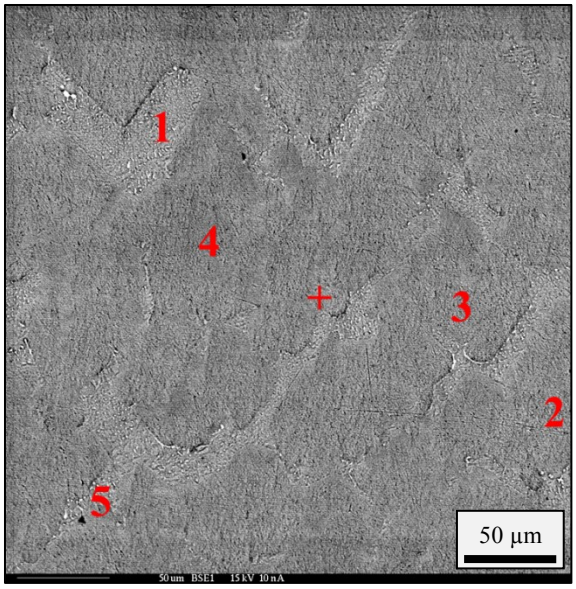

(b) Magnification = ~300x

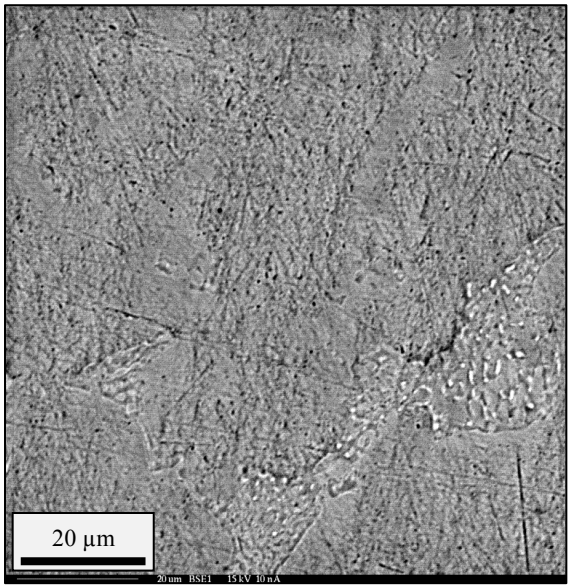

(c) Magnification = ~1000x

Figure 4-6: Backscattered electron images from the radial slice of the Group A Zr-12Fe-8Cu alloy: (a) 90x, (b) 300x, and (c) 1000x.

4.1.1.3. Zr-12Fe-15Cu Alloy

Images from the axial and radial sections of the Zr-12Fe-15Cu alloy are presented in Figs. 4-7 to 4-9. The images were recorded at nominal magnifications of 90x, 300x, and 1000x and WDS was completed to determine nominal phase compositions. Table 4-6 summarizes the WDS data from the axial sample in Fig. 4-8 and Table 4-7 summarizes the WDS data from the radial sample in Fig. 4-9. Once again cracks are evident in Fig. 4-7, however, it is of note that they only appear in the axial section which consequently exhibited some of the same features present in the previous two axial sections, namely the existence of Zr precipitates within the intermetallic matrix.

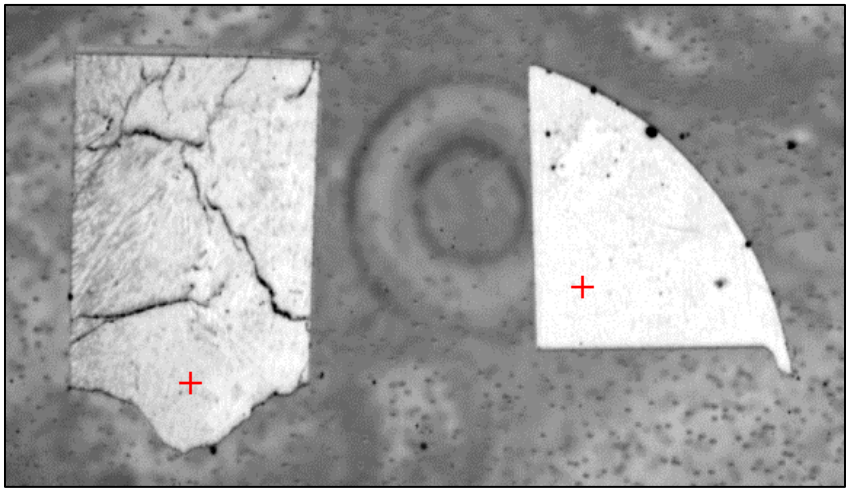

Figure 4-7: Optical scan of the Zr-12Fe-15Cu alloy: axial (left) and radial (right).

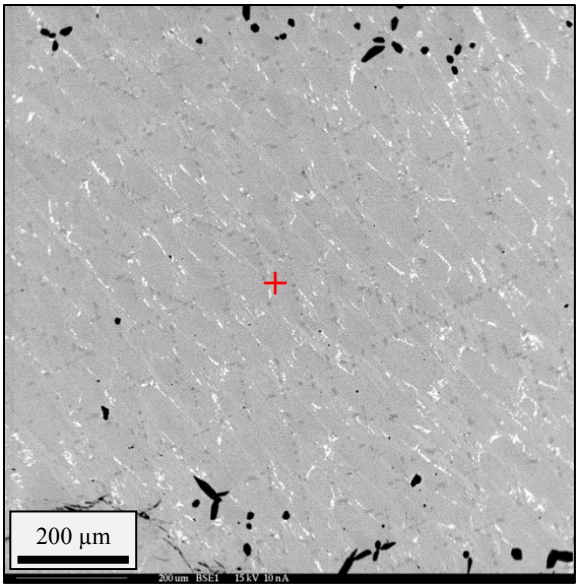

(a) Magnification = ~90x

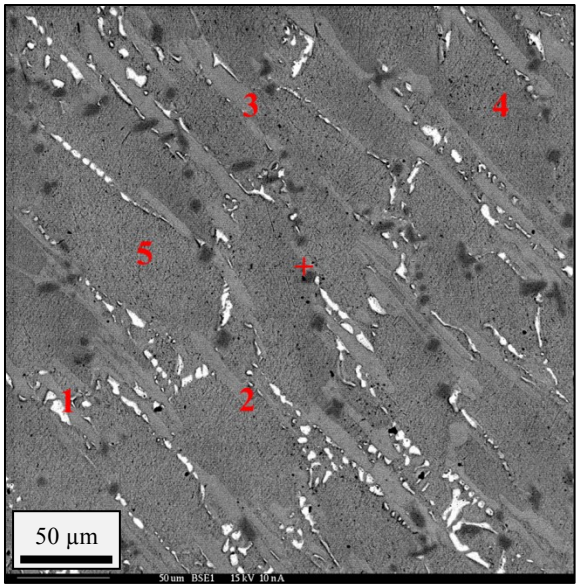

(b) Magnification = ~300x

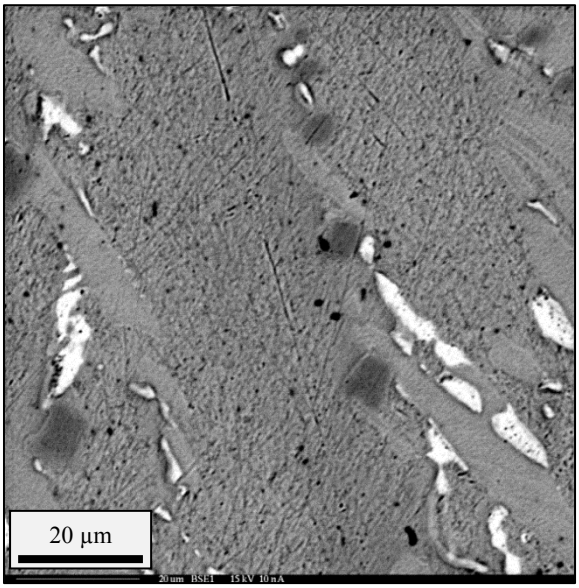

(c) Magnification = ~1000x

Figure 4-8: Backscattered electron images from the axial slice of the Group A Zr-12Fe-15Cu alloy: (a) 90x, (b) 300x, and (c) 1000x.

Table 4-6: Phase composition from WDS for Group A Zr-12Fe-15Cu (axial**).**

SPOT (FIG. 4-8B)	COLOR DESCRIPTION	ATOM PERCENT			WEIGHT PERCENT			
		Fe	Cu	Zr	Fe	Cu	Zr	Total
1[7]	White	-	-	-	-	-	-	-
2	Gray	4.64	28.36	67.00	3.23	22.43	76.06	101.72
3	Gray	4.20	28.85	66.95	2.91	22.75	75.79	101.45
4	Bulk Gray	20.48	12.52	67.00	14.44	10.04	77.15	101.63
5	Bulk Gray	20.35	12.68	66.97	14.36	10.18	77.17	101.70

From Table 4-6 and Fig. 4-8 it was apparent that the 3 phases observed in the axial images correspond well to the following:

SPOT 1: Zr solution phase with limited solubility for Fe and Cu

SPOTS 2-3: Apparent Zr_2M intermetallic (M = Fe and Cu)

SPOTS 4-5: Apparent Zr_2M intermetallic (M = Fe and Cu)

Table 4-7: Phase composition from WDS for Group A Zr-12Fe-15Cu (radial).

SPOT (FIG. 4-9B)	COLOR DESCRIPTION	ATOM PERCENT			WEIGHT PERCENT			
		Fe	Cu	Zr	Fe	Cu	Zr	Total
1	Light Gray	20.24	13.05	66.72	14.20	10.42	76.48	101.10
2	Light Gray	20.08	13.00	66.93	14.09	10.38	76.73	101.20
3	Dark Gray	19.46	30.02	50.53	14.54	25.52	61.67	101.74
4	Dark Gray	19.49	30.01	50.50	14.43	25.28	61.07	100.78

From Table 4-7 and Fig. 4-9 it was apparent that the radial section selected has a different morphology which corresponds well to the following:

SPOTS 1-2: Apparent Zr_2M intermetallic (M = Fe and Cu)

SPOTS 3-4: Apparent ZrM intermetallic (M = Fe and Cu)

[7] *Point 1 was taken using EDS and exhibited a large Zr peak with negligible Fe and Cu peaks. The spectrum obtained was consistent with other EDS data taken for similar phases in which WDS data was measured.*

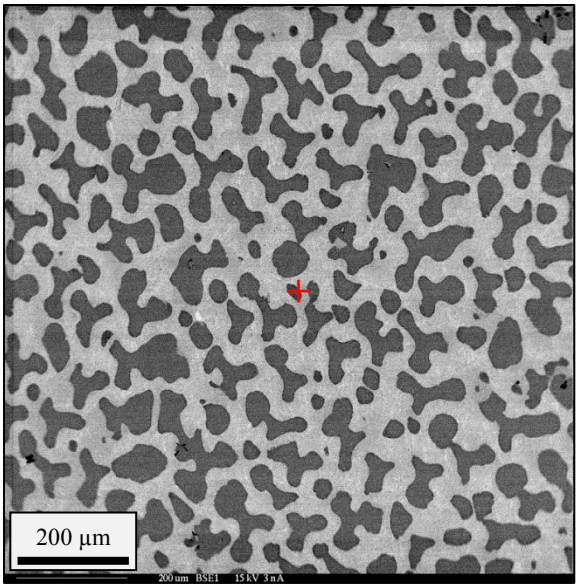

(a) Magnification = ~90x

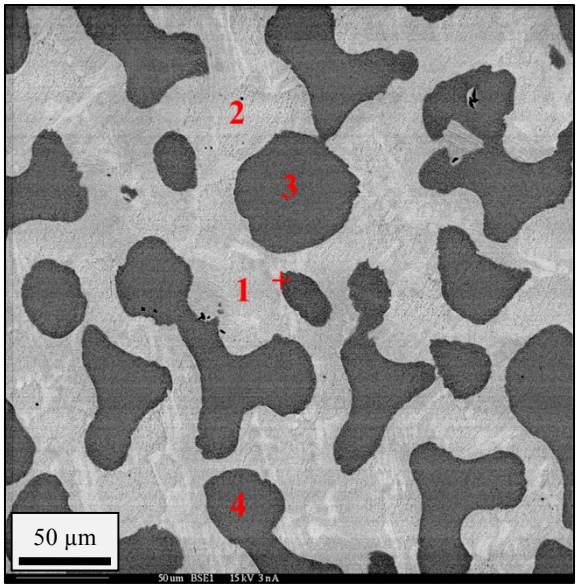

(b) Magnification = ~300x

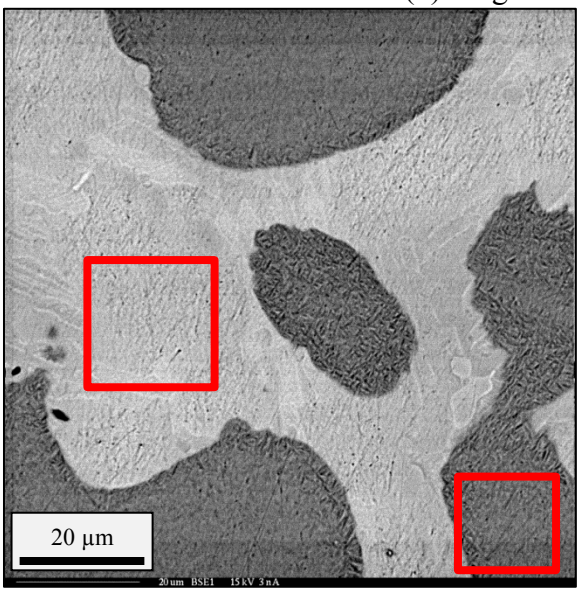

(c) Magnification = ~1000x

Figure 4-9: Backscattered electron images from the radial slice of the Group A Zr-12Fe-15Cu alloy: (a) 90x, (b) 300x, and (c) 1000x.

Due the preliminary nature of these alloys (they were sectioned for examination after a single initial casting), a full WDS analysis was not performed. However it was clear from the BSE images that the alloy did not cast uniformly as there were large differences in the phase structure between the top and bottom of the samples. WDS was performed for the key bulk phases shown in both sections. For the minor phases seen in the axial section, EDS data

for Points 1 and 6 indicated that the bright phases (Spot 1) had a composition similar to the Zr solution phase noted in the other samples while the dark phase (Spot 6) had a composition similar to the bulk intermetallic phase (Spots 4-5). The values for points 2 and 3 would be consistent with a Zr_2Cu intermetallic with some Fe on the Cu lattice sites. In contrast for points 4 and 5 would be consistent with a $FeZr_2$ intermetallic with some Cu on the Fe lattice sites.

Only two distinct phases were evident in the images from the radial section (Fig. 4-9), with the darker phase, marked by points 3 and 4, being uniformly dispersed within the light gray matrix phase, marked by points 1 and 2. This morphology was unique to this group as it did not appear in any of the other alloys nor was it expected at high temperature (Fig. 3-2) Additionally there appeared to be a third phase present made up of light gray precipitates, nevertheless, this features were not measure with either EDS or WDS once the decision was made to modify the casting procedure. It was evident that the alloy structures were not representative of equilibrium. It was also apparent that both the matrix phase and the islands had textural features that were possibly artifacts of the polishing cloth used in the final polish as highlighted in red in Fig. 4-9c.

4.1.1.4. Summary Group A

The principal observation from the sections above is that each of the alloys was indeed melted, with all components well mixed, and the solidified structure were not uniform. All of the expected phases were observed as well as an unexpected variant (i.e., the ZrM phase), but the relative amounts of the phases and their morphologies were inconsistent. This indicated inhomogeneous mixing and the need for a modified fabrication procedure. When it became evident that the alloys had not formed homogeneous structures, WDS and EDS characterization was halted, the casting procedures were adjusted according to Section 3.1 and a fresh casting was initiated.

4.1.2. Group B As-cast Alloys

Three changes were implemented as a result of the analyses in Section 4.1.1. First, the new alloys were held in the molten state for a longer time to enable further mixing. Second, the initial cast alloys were cleaned, inverted and re-melted in a second crucible. As noted in Section 3.1.2, the second melting was performed at 1200°C. Finally, the copper composition of the mid-level alloy was changed from 8 wt % to 10 wt% since the morphologies in the Zr-12Fe-5Cu and Zr-12Fe-8Cu appeared to be were so similar and the phase distinction predicted by Figure 3-2 was not realized.

The Zr-12Fe-(5,10,15)Cu alloys were sectioned and prepared for microprobe analysis in the same manner as Group A. In an effort to reduce both the amount of preparation time as well as time at the EPMA, as opposed to mounting each alloy in its own epoxy mount producing three mounts, all of the axial and radial sections were mounted together, thus reducing the number of mounts needed to analyze. Low magnification optical images from the microprobe are show in Figs. 4-10 and 4-11. It is notable that Zr-12Fe-5Cu and Zr-12Fe-10Cu were again found to be brittle with multiple cracks. The marker (+) in each of the images represents the general position for the backscattered electron (BSE) images taken at higher magnification. Just as in Group A, the radial section was cut from the bottom half of the sample while the axial section was cut from the top half of the samples.

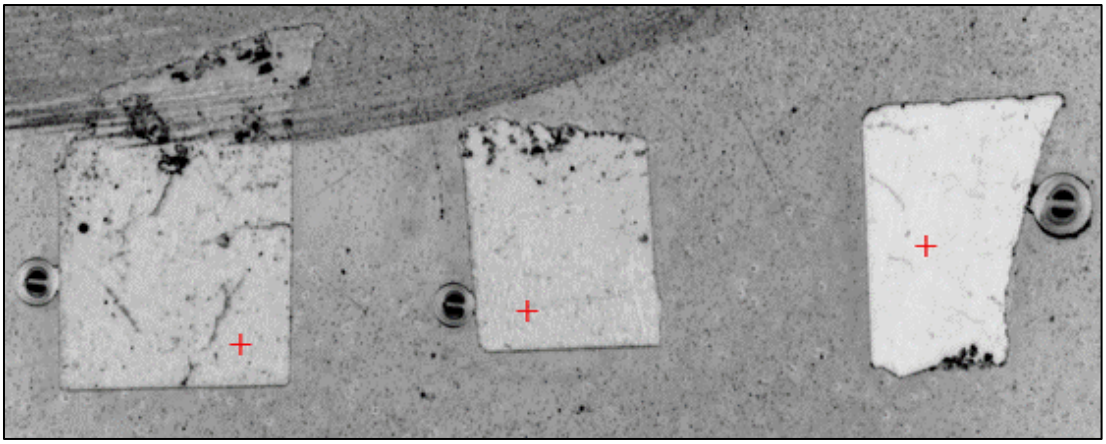

Figure 4-10: Optical scan of all three Group B axial sections: Zr-12Fe-5Cu (left), Zr-12Fe-10Cu (middle), and Zr-12Fe-15Cu (right).

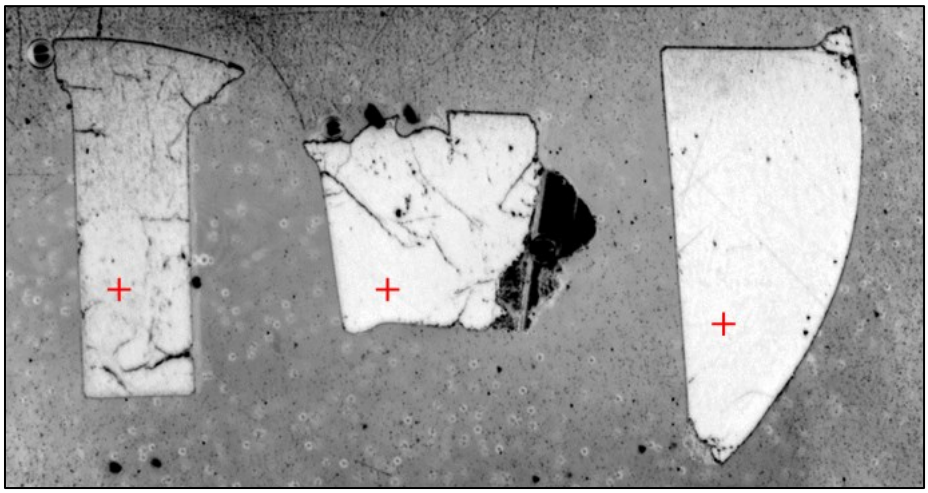

Figure 4-11: Optical scan of all three Group B radial sections: Zr-12Fe-5Cu (left), Zr-12Fe-10Cu (middle), and Zr-12Fe-15Cu (right)

4.1.2.1. Zr-12Fe-5Cu Alloy

Images from the axial and radial sections of the Zr-12Fe-5Cu alloy are presented in Figs. 4-12 and 4-13. The images were recorded at nominal magnifications of 90x, 300x, and 1000x and WDS was completed to determine nominal phase compositions. Table 4-8 summarizes the WDS data from the axial sample in Fig. 4-12 and Table 4-9 summarizes the WDS data from the radial sample in Fig. 4-13.

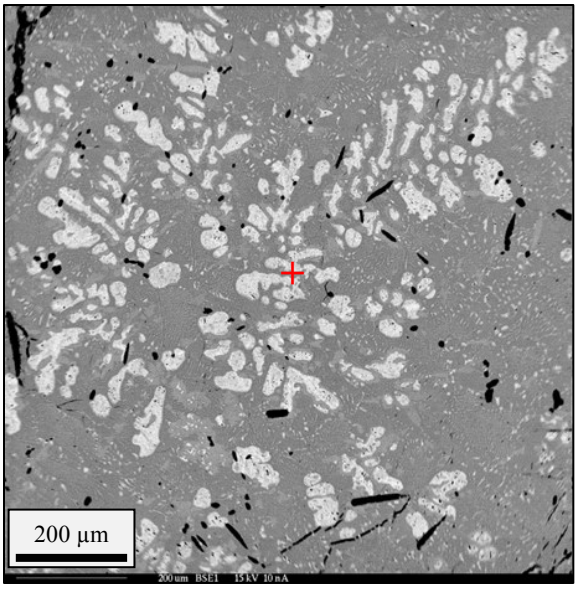

(a) Magnification = ~90x

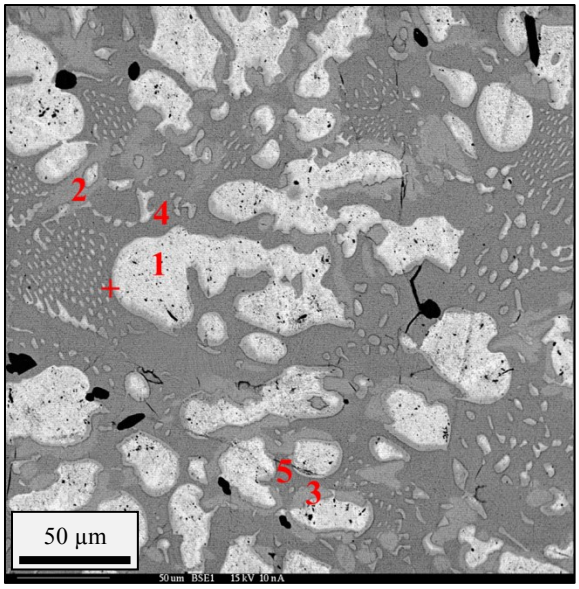

(b) Magnification = ~300x

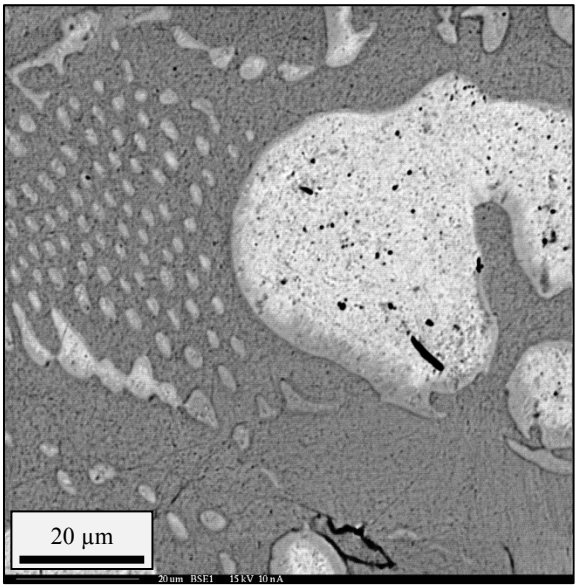

(c) Magnification = ~1000x

Figure 4-12: Backscattered electron images from the axial slice of the Group B Zr-12Fe-5Cu alloy: (a) 90x, (b) 300x, and (c) 1000x.

Table 4-8: Phase composition from WDS for Group B Zr-12Fe-5Cu (axial)

SPOT (FIG. 4-12B)	COLOR DESCRIPTION	ATOM PERCENT			WEIGHT PERCENT			
		Fe	Cu	Zr	Fe	Cu	Zr	Total
1	White	3.00	2.28	94.72	1.88	1.62	96.91	100.41
2	Light Gray	20.85	3.64	75.51	14.14	2.81	83.61	100.56
3	Light Gray	20.75	3.64	75.61	14.02	2.80	83.44	100.26
4	Bulk Gray	22.34	10.11	67.55	15.69	8.07	77.47	101.23
5	Bulk Gray	23.97	8.41	67.61	16.85	6.73	77.62	101.20

From Table 4-8 and Fig. 4-12 it was apparent that there are three phases observed in the axial images corresponded well to the following:

SPOT 1: Zr solution phase with limited solubility for Fe and Cu

SPOTS 2-3: Apparent Zr_3M intermetallic (M = Fe and Cu)

SPOTS 4-5: Apparent Zr_2M intermetallic (M = Fe and Cu)

Table 4-9: Phase composition from WDS for Group B Zr-12Fe-5Cu (radial)

SPOT (FIG. 4-13B)	COLOR DESCRIPTION	ATOM PERCENT			WEIGHT PERCENT			
		Fe	Cu	Zr	Fe	Cu	Zr	Total
1	White	1.21	2.41	96.39	0.76	1.72	98.82	101.30
2	Light Gray	20.33	4.20	75.47	13.72	3.23	83.19	100.14
3	Light Gray	20.10	4.48	75.42	13.64	3.46	83.60	100.70
4	Bulk Gray	20.50	12.30	67.20	14.44	9.85	77.29	101.58
5	Bulk Gray	22.75	9.83	67.42	16.01	7.87	77.50	101.38
6	Bulk Gray	23.64	9.15	67.21	16.67	7.34	77.37	101.38

From Table 4-9 and Fig. 4-13 it was apparent that there are (again) three phases observed in the axial images corresponded well to the following:

SPOT 1: Zr solution phase with limited solubility for Fe and Cu

SPOTS 2-3: Apparent Zr_3M intermetallic (M = Fe and Cu)

SPOTS 4-6: Apparent Zr_2M intermetallic (M = Fe and Cu)

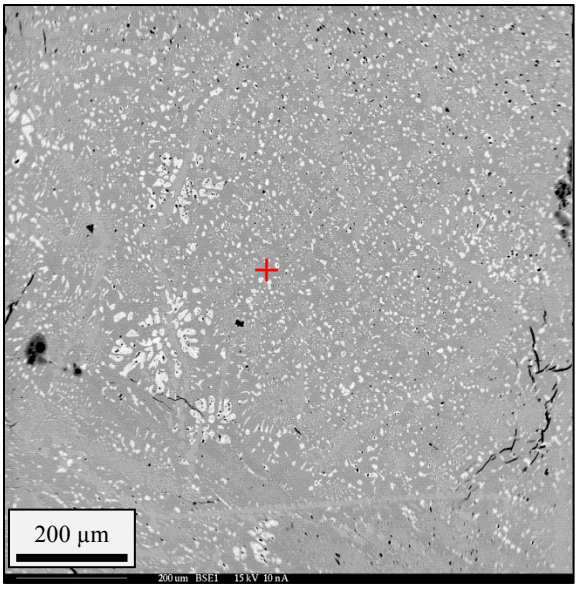

(a) Magnification = ~90x

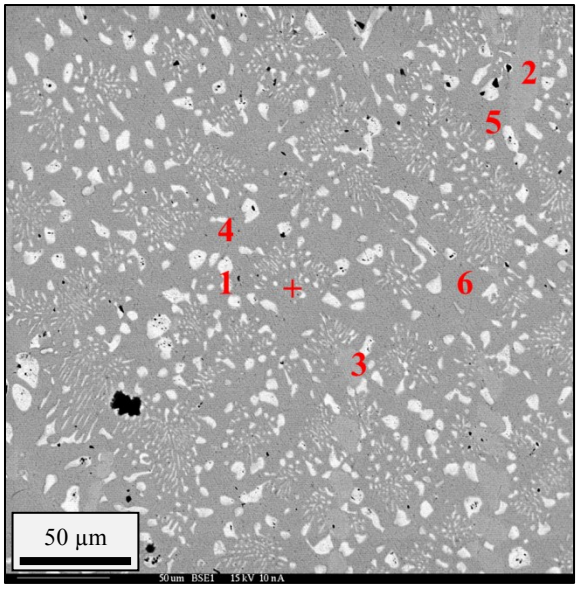

(b) Magnification = ~300x

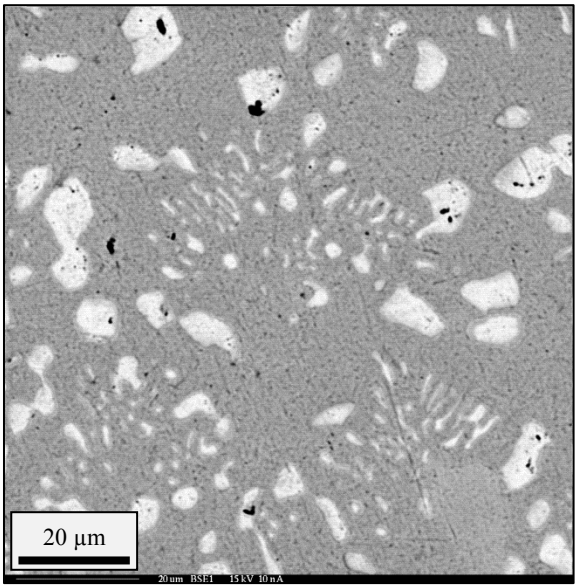

(c) Magnification = ~1000x

Figure 4-13: Backscattered electron images from the radial slice of the Group B Zr-12Fe-5Cu alloy: (a) 90x, (b) 300x, and (c) 1000x.

During characterization, it was initially observed that the axial and radial samples had slightly different morphologies due to the size and contrast differences. However, the WDS data indicated that each section consisted of the same three phases, a Zr solution phase with two intermetallic phases, Zr_3M and Zr_2M. The shape differences are likely to be due to

differing solidification rates observed during the cool-down stage of fabrication. As with Group A, there also appeared to a 4th phase which appeared around the edge of the Zr precipitates, however, this again was shown to be rounding of the Zr as a result of polishing. These findings were confirmed with EDS.

Again, it is of note that there is a sizeable difference in the morphology of the zirconium-rich phases (coarse in Fig. 4-12a and fine in Fig. 4-13a). Other than the difference in size of the Zr precipitates, each section seemed to exhibit the same basic phase morphologies as well as the resulting elemental compositions. The light grey precipitates and bulk gray matrix phase each appeared to form the two basic intermetallic phase seen in the Fe-Zr phase diagram. The WDS results indicate that the two phases resemble Zr_3Fe and Zr_2Fe in which some of the lattice points are filled by Cu, a feature noted in the previous alloys. The large black structures are yttria oxide particles which migrated into the sample during casting. This was confirmed with EDS.

4.1.2.2. Zr-12Fe-10Cu Alloy

Images from the axial and radial sections of the Zr-12Fe-10Cu alloy are presented in Figs. 4-14 and 4-15. The images were recorded at nominal magnifications of 90x, 300x, and 1000x and WDS was completed to determine nominal phase compositions. Table 4-10 summarizes the WDS data from the axial sample in Fig. 4-15 and Table 4-11 summarizes the WDS data from the radial sample in Fig. 4-16.

It is significant to note that there were large differences between the axial and radial section of this alloy despite the double-melt procedure employed with extended hold times at the melt temperatures. This apparent tendency toward component segregation along with the brittle nature evident from the macro-cracks in Fig. 4-10 and 4-11 indicates that this alloy may have challenges performing as the metal matrix for the fuel concept under discovery.

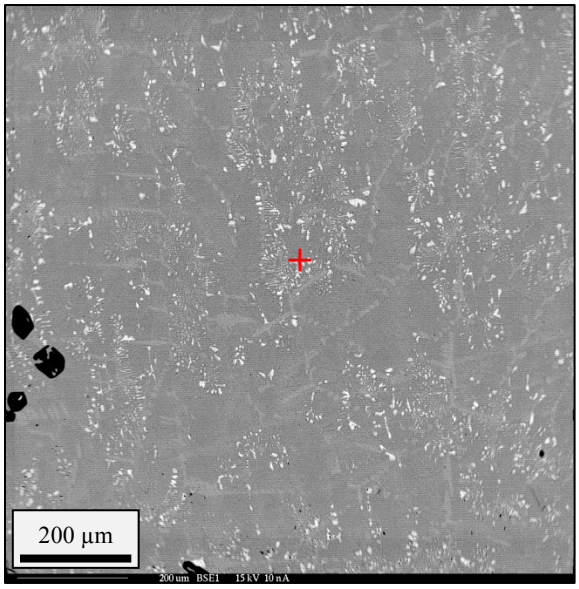

(a) Magnification = ~90x

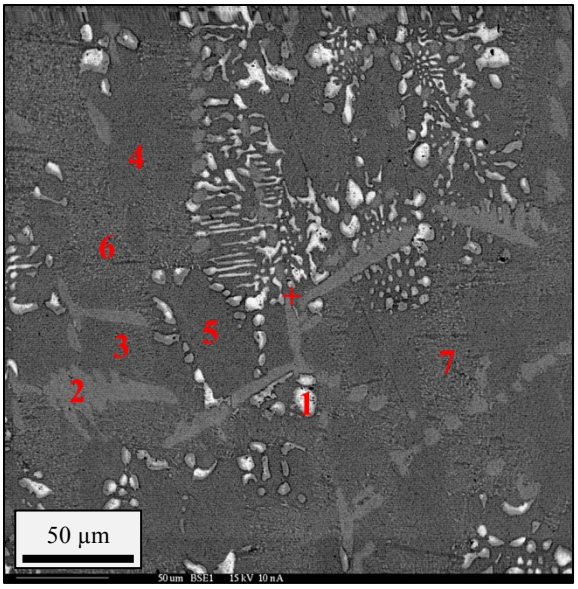

(b) Magnification = ~300x

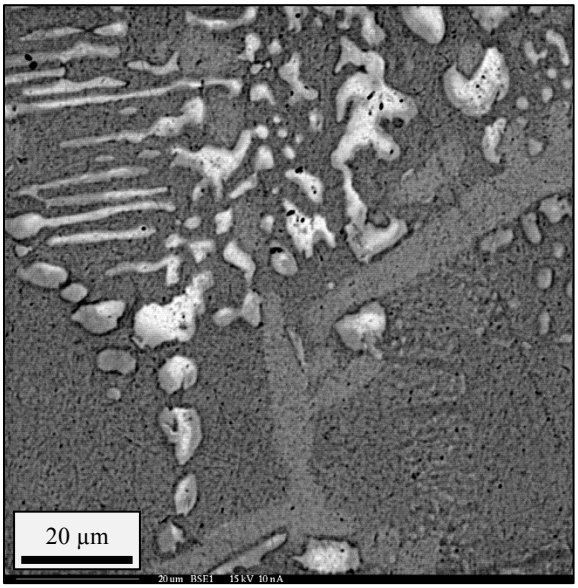

(c) Magnification = ~1000x

Figure 4-14: Backscattered electron images from the axial slice of the Group B Zr-12Fe-10Cu alloy: (a) 90x, (b) 300x, and (c) 1000x.

Table 4-10: Phase composition from WDS for Group B Zr-12Fe-10Cu (axial).

SPOT (FIG. 4-14B)	COLOR DESCRIPTION	ATOM PERCENT			WEIGHT PERCENT			
		Fe	Cu	Zr	Fe	Cu	Zr	Total
1	White	0.59	0.95	98.46	0.37	0.68	100.76	101.81
2	Light Gray	18.04	7.03	74.92	12.24	5.43	83.03	100.70
3	Bulk Gray	20.67	12.11	67.23	14.50	9.67	77.04	101.21
4	Bulk Gray	15.27	14.70	70.03	10.57	11.58	79.17	101.31
5	Bulk Gray	20.99	11.84	67.17	14.75	9.47	77.13	101.36
6	Intermediate Gray	11.95	16.32	71.73	8.15	12.66	79.86	100.66
7	Intermediate Gray	12.93	15.52	71.56	8.88	12.12	80.26	101.26

From Table 4-10 and Fig. 4-14 it appeared that there are three phases observed in the axial images roughly corresponded well to the following:

SPOT 1: Zr solution phase with limited solubility for Fe and Cu

SPOTS 2 & 6-7: Apparent Zr_3M intermetallic (M = Fe and Cu)

SPOTS 3-5: Apparent Zr_2M intermetallic (M = Fe and Cu)

Table 4-11: Phase composition from WDS for Group B Zr-12Fe-10Cu (radial)

SPOT (FIG. 4-15B)	COLOR DESCRIPTION	ATOM PERCENT			WEIGHT PERCENT			
		Fe	Cu	Zr	Fe	Cu	Zr	Total
1	Bulk Gray	19.68	13.20	67.12	13.87	10.58	77.22	101.67
2	Bulk Gray	20.66	12.53	66.82	14.59	10.07	77.10	101.75
3	Intermediate Gray	4.60	28.42	66.99	3.19	22.43	75.88	101.50
4	Intermediate Gray	4.49	28.90	66.61	3.14	23.00	76.08	102.22
5	Dark Gray	20.55	28.78	50.67	15.41	24.55	62.06	102.02

From Fig. 4-15, one can clearly see that the features found in the axial section were not the same as those seen in those found in Fig. 14. From Table 4-11 and Fig. 4-15 it was apparent that the phases observed in the axial images corresponded well to the following:

SPOTS 1-2: Apparent Zr_2M intermetallic (M = Fe and Cu, Fe-rich)

SPOTS 3-4: Apparent Zr_2M intermetallic (M = Fe and Cu, Cu-rich)

SPOTS 5: Apparent ZrM intermetallic (M = Fe and Cu)

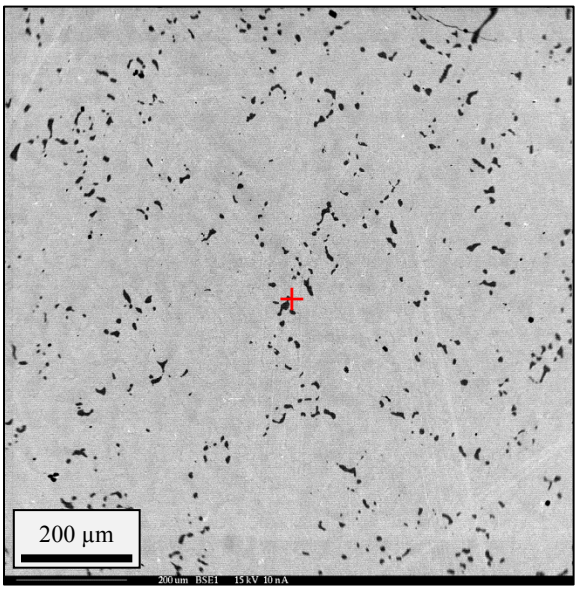

(a) Magnification = ~90x

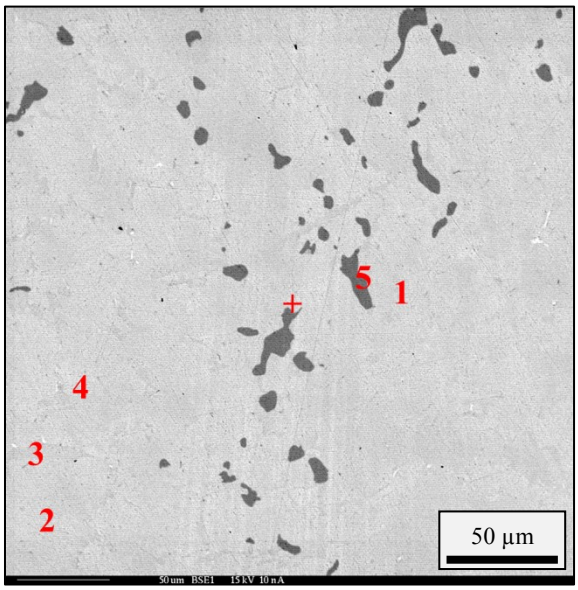

(b) Magnification = ~300x

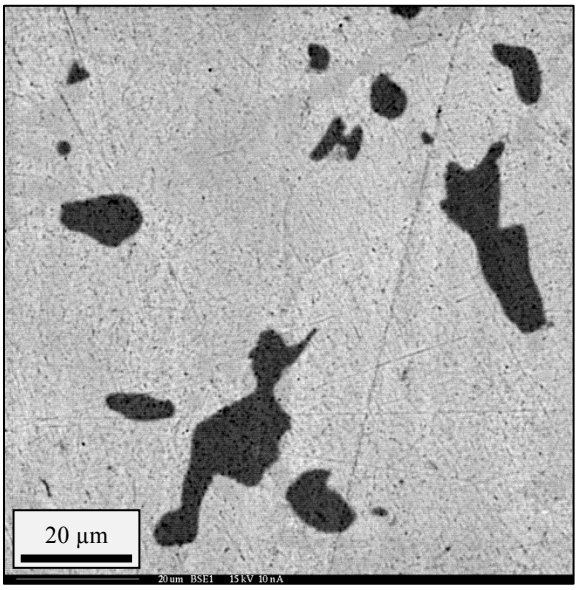

(c) Magnification = ~1000x

Figure 4-15: Backscattered electron images from the radial slice of the Group B Zr-12Fe-10Cu alloy: (a) 90x, (b) 300x, and (c) 1000x.

The axial section appeared to have very similar observed features as those found in the Zr-12Fe-5Cu alloy (Figs. 4-12 and 4-13) but their relative volume fraction is different. After enhancing the image, it was apparent that the axial section contained several different intermetallic phases each containing varying amounts of Fe and Cu. For instance, although Spots 3-5 appear to be Zr_2M, each phase contained differing amounts of Fe, Cu, and Zr, varying by as much as 8.5%. These variations could be the result of features that are too fine for the spatial resolution of the EMPA-WDS. Therefore the numbers appearing in Table 4-10 are estimates of the elemental composition rather than true values.

As apparent from Fig. 4-15, the radial section did not contain the same features as the axial section, namely the absence of any Zr precipitates. Where the top half of the sample appeared to share similar features to Zr-12Fe-5Cu, the bottom portion of the sample appeared to share similar features to the Zr-12Fe-15Cu alloy, which will be discussed in the proceeding section. The radial section was made up entirely of intermetallics and as was seen in the axial section, each of the three intermetallic phases exhibited variations in elemental composition; the variations were far less extreme however, varying by 1-2% rather than upwards of 8% seen in the axial section. Two of the intermetallic phases present appeared to have the same structure, but one was Cu rich and the other was Fe rich.

4.1.2.3. Zr-12Fe-15Cu Alloy

Images from the axial and radial sections of the Zr-12Fe-15Cu alloy are presented in Figs. 4-16 and 4-17. The images were recorded at nominal magnifications of 90x, 300x, and 1000x and WDS was completed to determine nominal phase compositions. Table 4-12 summarizes the WDS data from the axial sample in Fig. 4-16 and Table 4-13 summarizes the WDS data from the radial sample in Fig. 4-17. Additionally, this appeared to be the least brittle of the three alloys, showing very little cracking, even after polishing as seen in Figs. 4-10 and 4-11 which was remarkable given that it is composed entirely of intermetallic compounds.

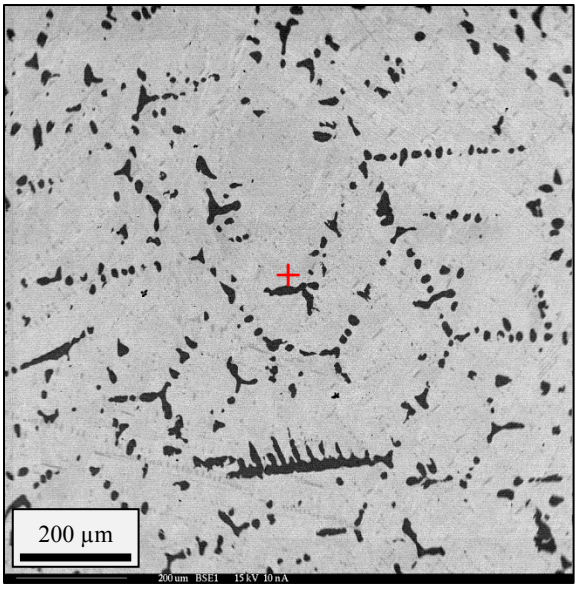

(a) Magnification = ~90x

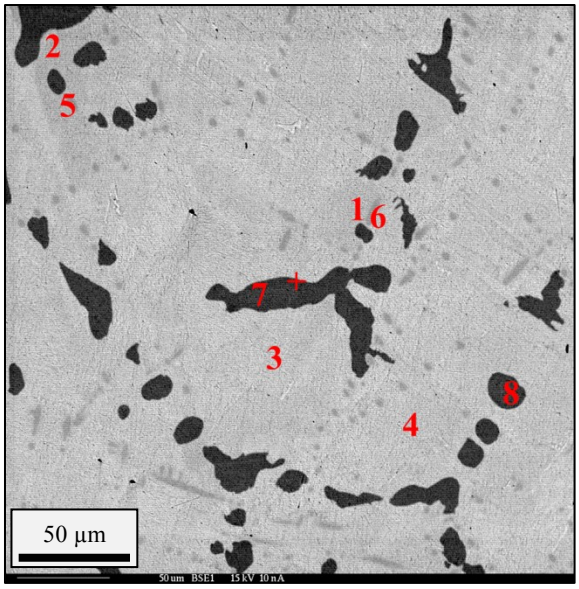

(b) Magnification = ~300x

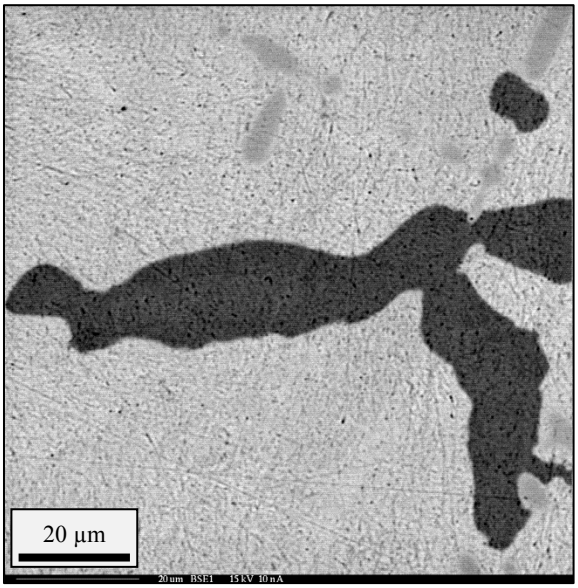

(c) Magnification = ~1000x

Figure 4-16: Backscattered electron images from the axial slice of the Group B Zr-12Fe-15Cu alloy: (a) 90x, (b) 300x, and (c) 1000x.

Table 4-12: Phase composition from WDS for Group B Zr-12Fe-15Cu (axial).

SPOT (FIG. 4-16B)	COLOR DESCRIPTION	ATOM PERCENT			WEIGHT PERCENT			
		Fe	Cu	Zr	Fe	Cu	Zr	Total
1	Light Gray	19.29	13.87	66.84	13.65	11.16	77.24	102.05
2	Light Gray	19.17	14.06	66.77	13.57	11.33	77.23	102.13
3	Bulk Gray	13.98	18.96	67.06	9.79	15.11	76.69	101.58
4	Bulk Gray	18.30	14.91	66.79	12.90	11.96	76.87	101.73
5	Intermediate Gray	18.97	13.21	67.82	13.07	10.35	76.28	99.69
6	Intermediate Gray	19.03	13.24	67.73	13.14	10.41	76.40	99.95
7	Dark Gray	18.58	30.39	51.04	13.85	25.78	62.17	101.80
8	Dark Gray	18.68	30.47	50.86	13.94	25.88	62.01	101.84

From Table 8 and Fig. 18 it appeared that there are two phases observed in the axial images roughly corresponded well to the following:

SPOTS 1-6: Apparent Zr_2M intermetallic (M = Fe and Cu) with variations in Fe and Cu causing image variations.

SPOTS 7-8: Apparent ZrM intermetallic (M = Fe and Cu)

Table 4-13: Phase composition from WDS for Group B Zr-12Fe-15Cu (radial).

SPOT (FIG. 4-17B)	COLOR DESCRIPTION	ATOM PERCENT			WEIGHT PERCENT			
		Fe	Cu	Zr	Fe	Cu	Zr	Total
1	Bulk Gray	19.29	13.57	67.14	13.53	10.84	76.95	101.32
2	Bulk Gray	20.55	12.66	66.79	14.53	10.19	77.15	101.87
3	Intermediate Gray	21.10	11.69	67.22	14.62	9.22	76.10	99.94
4	Intermediate Gray	20.94	11.76	67.30	14.53	9.29	76.28	100.10
5	Dark Gray	20.11	29.28	50.61	15.11	25.02	62.09	102.22
6	Dark Gray	20.18	29.31	50.51	15.21	25.13	62.18	102.51

From Table 4-13 and Fig. 4-17, it appeared that there are two phases observed in the axial images roughly corresponded well to the following:

SPOTS 1-4: Apparent Zr_2M intermetallic (M = Fe and Cu) with variations in Fe and Cu causing image variations

SPOTS 5-6: Apparent ZrM intermetallic (M = Fe and Cu)

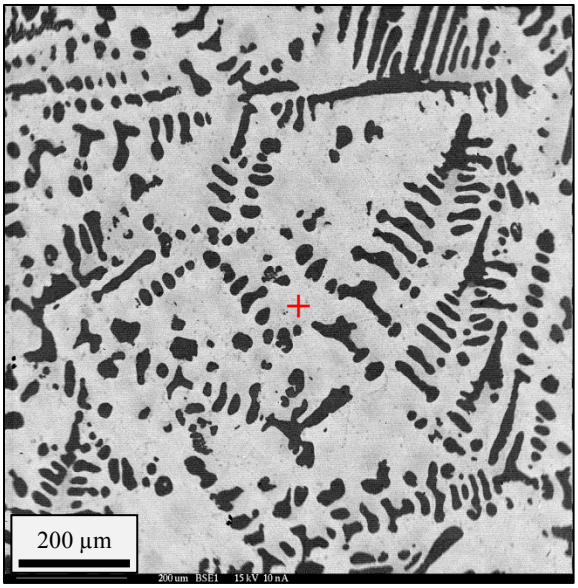

(a) Magnification = ~90x

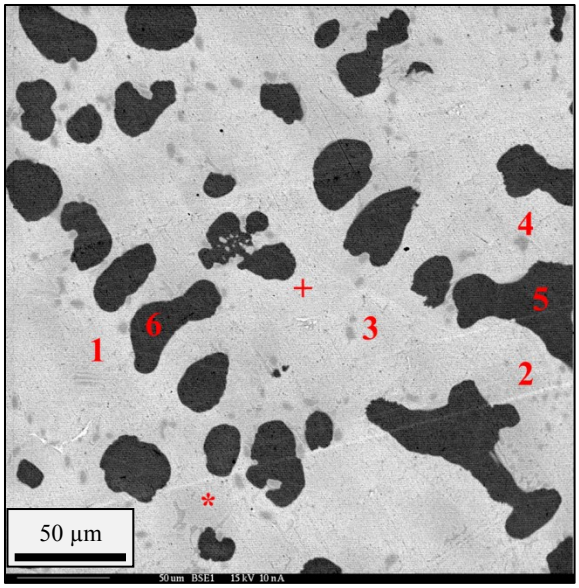

(b) Magnification = ~300x

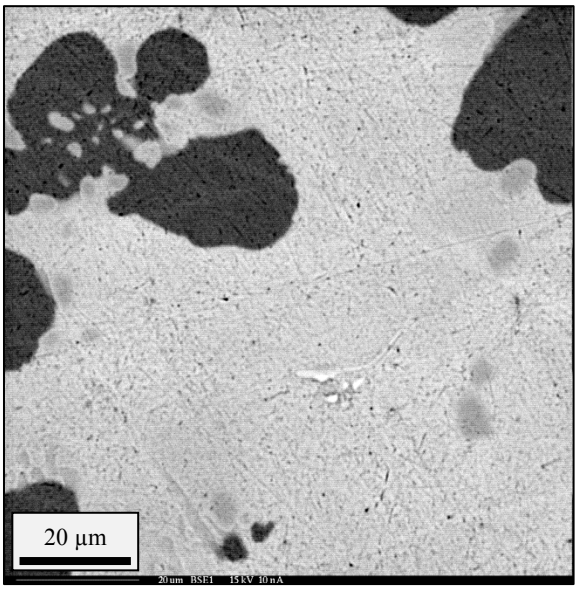

(c) Magnification = ~1000x

Figure 4-17: Backscattered electron images from the radial slice of the Group B Zr-12Fe-15Cu alloy: (a) 90x, (b) 300x, and (c) 1000x.

From the BSE images it appears that homogenous mixing was achieved as many of the features seen in the axial section are also present the in radial section; the two phases seen in the axial section (ZrM and Zr_2M) were also present in the radial section. Upon further examination, there were slight differences, namely a lack of Fe & Cu composition variations in the bulk phase in the radial section. Whereas the bulk phase in the axial section contained several different Fe and Cu compositions, the bulk light gray phase in the radial section appeared to be much more uniform. The radial slice also lacked a third Zr_2(Fe,Cu) phase seen in the axial section. This however may not have actually been the case given further analysis of the BSE images; there appears to be a fourth phase within the bulk intermetallic phase marked by the asterisks which were very difficult to distinguish from the bulk matrix phase. Because of this subtle change in contrast, during initial imaging, these structures weren't seen. Therefore, this phase may have been present in the sample and just wasn't measured.

4.1.2.4. Summary of Group B As-cast Alloys

The principal observation from the Group B casting was that each of the alloys prepared and examined were indeed mixed and cast. The Zr-12Fe-5Cu and Zr-12Fe-15Cu alloys were homogenous, but the Zr-12Fe-10Cu alloy was heterogeneous and brittle when prepared under the same conditions. The expected combination of phases was observed in part in the Zr-12Fe-10Cu alloy, however, the relative amounts of the phases and their morphologies were inconsistent, indicating inhomogeneous mixing yet again. The predicted phases were observed for both 5Cu and 15Cu with the exception of the $ZrFe_2$ Laves phase. Additionally, it was apparent that non-equilibrium phases formed under the casting conditions and that annealing the samples would need to be done in order to homogenize the samples.

4.1.3. Group B Annealed Alloys[8]

In an effort to homogenize the samples before thermophysical analysis, section from each of the three alloys was heat treated in a sealed quartz vacuum tube for 1 week at 700°C (according to the procedure described in Section 3.1.4). In order to avoid composition shifts, the heat treated samples were sectioned from the top half of each of the alloy slugs. The final homogenized microstructural morphologies and compositions for each alloy are documented in the following sections.

The annealed Zr-12Fe-(5,10,15)Cu alloys were sectioned and prepared for microprobe analysis under the same conditions as the as-cast samples. All three samples were mounted in a single epoxy mount as shown in Fig. 4-18. It is notable that all three alloys exhibited multiple brittle cracks and pitting which appeared only after polishing. This is interesting to note because the polishing conditions remained unchanged, however after heat treating the samples they became even more brittle and prone to not only cracking but also pitting during polishing. The marker (+) in each of the images represents the general position for the backscattered electron (BSE) images taken at higher magnification.

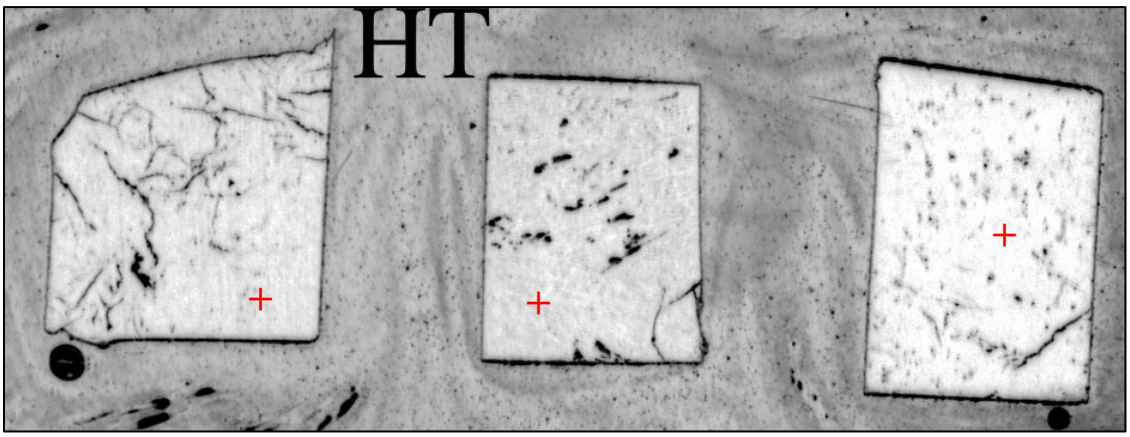

Figure 4-18: Optical scan of all three Group BHT alloys: Zr-12Fe-5Cu (left), Zr-12Fe-10Cu (middle), and Zr-12Fe-15Cu (right).

[8] *Denoted as Group BHT*

4.1.3.1. Zr-12Fe-5Cu Heat Treated Alloy

Images from the heat treated Zr-12Fe-5Cu alloy are presented in Fig 4-19. The images were recorded at nominal magnifications of 90x, 300x, and 1000x and WDS was completed to determine nominal phase compositions. Table 4-14 summarizes the WDS data.

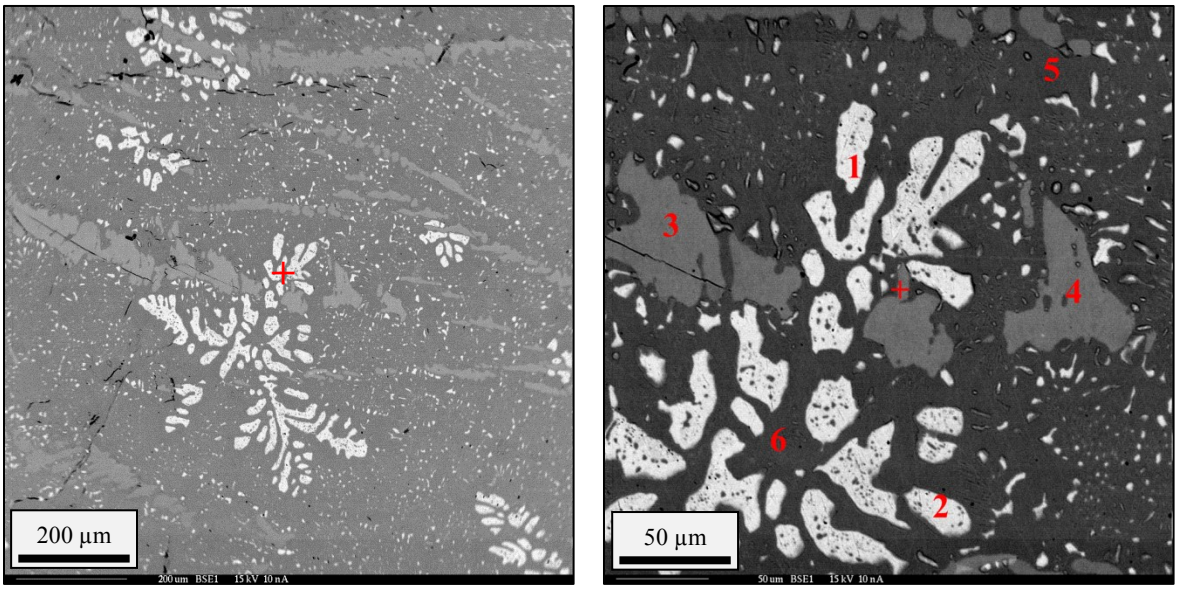

(a) Magnification = ~90x (b) Magnification = ~300x

Figure 4-19: Backscattered electron images from Group BHT Zr-12Fe-5Cu alloy: (a) 90x, (b) 300x, and (c) 1000x.

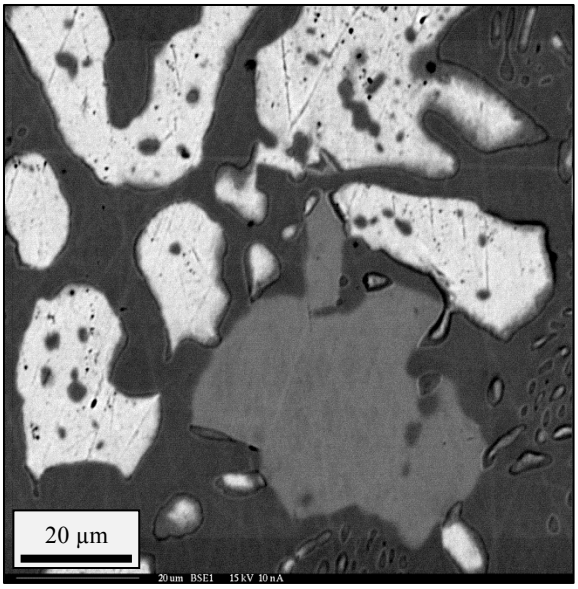

(c) Magnification = ~1000x

Figure 4-19: Continued.

Table 4-14: Phase composition from WDS for Group BHT Zr-12Fe-15Cu.

SPOT (FIG. 4-19B)	COLOR DESCRIPTION	ATOM PERCENT			WEIGHT PERCENT			
		Fe	Cu	Zr	Fe	Cu	Zr	Total
1	White	0.62	0.52	98.86	0.39	0.37	100.17	100.92
2	White	0.61	0.53	98.86	0.38	0.38	100.29	101.05
3	Light Gray	20.01	4.51	75.48	13.50	3.46	83.20	100.16
4	Light Gray	20.35	4.09	75.55	13.79	3.16	83.60	100.55
5	Bulk Gray	22.10	10.62	67.28	15.47	8.46	76.93	100.86
6	Bulk Gray	21.98	10.87	67.16	15.39	8.66	76.84	100.90

From Table 4-14 and Fig. 4-19 it was apparent that there are three phases observed in the axial images corresponded well to the following:

SPOT 1: Zr solution phase with limited solubility for Fe and Cu

SPOTS 3-4: Apparent Zr_3M intermetallic (M = Fe and Cu)

SPOTS 5-6: Apparent Zr_2M intermetallic (M = Fe and Cu)

Results from the WDS show that after annealing the sample appeared to be more uniform across the bulk intermetallic phase compared to the as-cast samples. The same three

phase morphologies were present as listed above. There were significantly more cracks in both the low magnification optical scan, Fig. 4-18, and in the 90x BSE images, Fig. 4-19. The larger black spots were yttria oxide impurities as a result of the molten Zr alloy consuming the yttrium oxide crucibles during initial casting. The thermodynamic mechanism for dissolving the very-stable yttrium oxide into the Zr liquid is not well understood, but it has been observed repeatedly in this study. The primary Zr solution phase formed two distinct structures, the first were large dendritic structures, while smaller (~1-5 μm) Zr precipitates formed within the bulk matrix phase. Once again, rounding of the softer Zr solution phases was observed, however there was a distinct grain boundary between the Zr solution phase and the matrix phase as seen in the BSE images. This confirmed that the appearance of a dark gray structure around the bright white spots was in fact the result of rounding and not the formation of another phase. Additionally, in contrast to the axial as-cast section, Fig. 4-12, (from which this sample was also sectioned), the second intermetallic phase formed both large precipitates approximately 50 μm in size and large linear structures which spanned across the entire samples, a feature first seen in the radial section of the Group A alloy.

4.1.3.2. Zr-12Fe-10Cu Heat Treated Alloy

Images from the heat treated Zr-12Fe-10Cu alloy are presented in Fig 4-20. The images were recorded at nominal magnifications of 90x, 300x, and 1000x and WDS was completed to determine nominal phase compositions. Table 4-15 summarizes the WDS data.

Table 4-15: Phase composition from WDS for Group BHT Zr-12Fe-10Cu.

SPOT (FIG. 4-20B)	COLOR DESCRIPTION	ATOM PERCENT			WEIGHT PERCENT			
		Fe	Cu	Zr	Fe	Cu	Zr	Total
1	White	0.53	1.47	98.01	0.33	1.04	99.86	101.23
2	White	0.24	0.80	98.96	0.15	0.56	100.36	101.07
3	Light Gray	19.32	5.04	75.64	13.11	3.89	83.81	100.81
4	Light Gray	19.46	5.18	75.36	13.21	4.00	83.56	100.77
5	Bulk Gray	21.04	11.52	67.44	14.67	9.14	76.81	100.62
6	Bulk Gray	20.99	11.48	67.54	14.70	9.15	77.28	101.13
7	Intermediate Gray	3.29	27.31	69.39	2.25	21.19	77.27	100.70
8	Intermediate Gray	4.37	27.96	67.67	3.01	21.91	76.12	101.04
9	Intermediate Gray	21.12	10.64	68.24	14.49	8.30	76.44	99.23

From Table 4-15 and Fig. 4-20 it was apparent that there are three phases observed in the axial images corresponded well to the following:

SPOTS 1-2: Zr solution phase with limited solubility for Fe and Cu

SPOTS 3-4: Apparent Zr_3M intermetallic (M = Fe and Cu)

SPOTS 5-6,9: Apparent Zr_2M intermetallic (M = Fe and Cu, Fe-rich)

SPOT 7-8: Apparent Zr_2M intermetallic (M = Fe and Cu, Cu-rich)

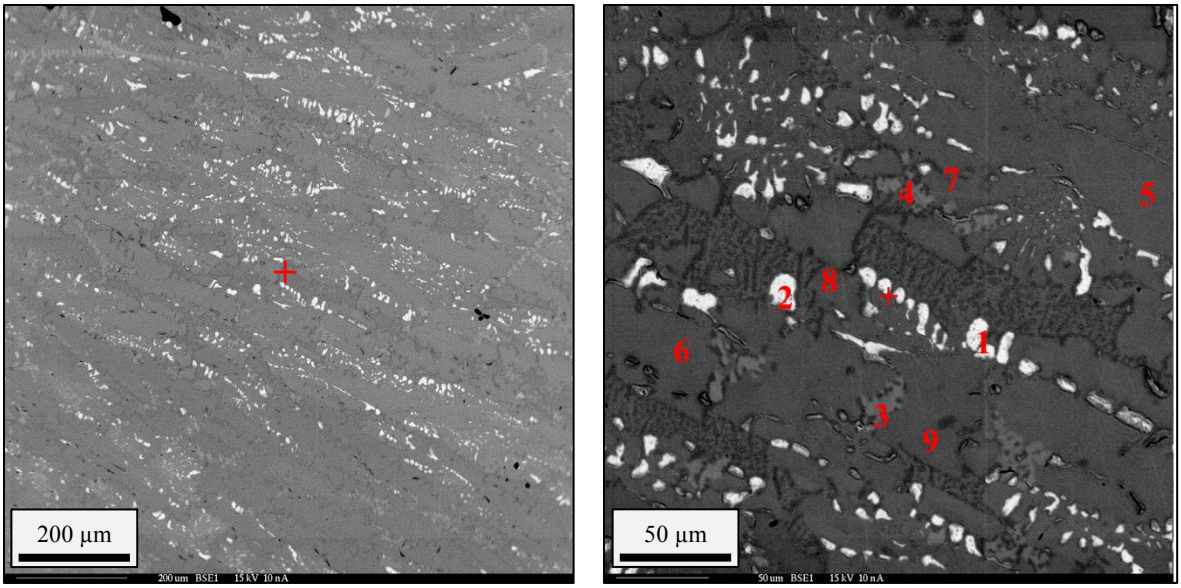

(a) Magnification = ~90x (b) Magnification = ~300x

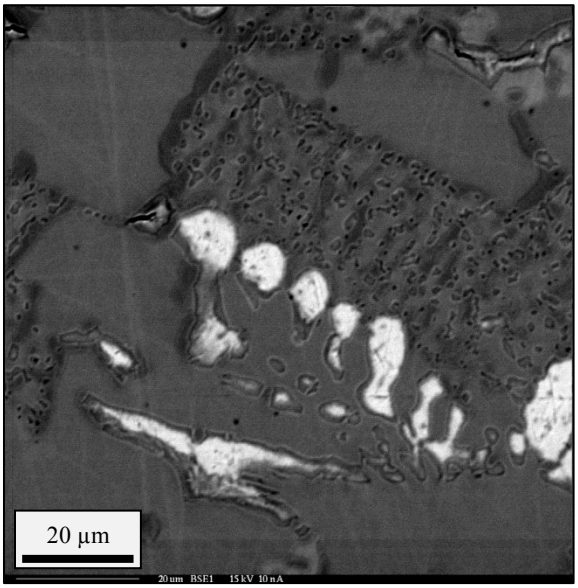

(c) Magnification = ~1000x

Figure 4-20: Backscattered electron images from Group BHT Zr-12Fe-10Cu alloy: (a) 90x, (b) 300x, and (c) 1000x.

From the BSE images it is apparent that this alloy had the most complex microstructure of all three of the alloys, even more so after annealing. The annealed alloy appeared to have six different phases present, however, only four were measured with WDS. First there was the Zr solution phase which appeared as bright white spots ranging in size

from smaller than 1 μm to upwards of 10 μm. Next, there was the light gray phase which has an apparent Zr_3M structure based on of the atomic percent given by WDS analysis. The third and most prevalent phase was the bulk Zr_2M intermetallic phase. Within this bulk matrix phase, there is Cu rich zones wherein the Cu concentrations increase from below 6 at% to above 25 at%. These Cu rich zones are present on the border of the light gray intermetallic precipitates and formed a web like structure. They have the same apparent structure (Zr_2M) as the larger intermediate gray precipitates shown by Spot 9, however, the larger precipitates have a different elemental composition and are Fe rich rather than Cu rich. The Cu rich intermetallic phase appeared to be part of the decomposition of another phase. The break up formed the Cu rich intermediate phase in addition to the small black structures within the web (Fig. 4-20c). These precipitates were less than a micron in size and thus their composition was not analyzed.

4.1.3.3. Zr-12Fe-15Cu Heat Treated Alloy

Images from the heat treated Zr-12Fe-15Cu alloy are presented in Fig. 4-21. The images were recorded at nominal magnifications of 90x, 300x, and 1000x and WDS was completed to determine nominal phase compositions. Table 4-16 summarizes the WDS data.

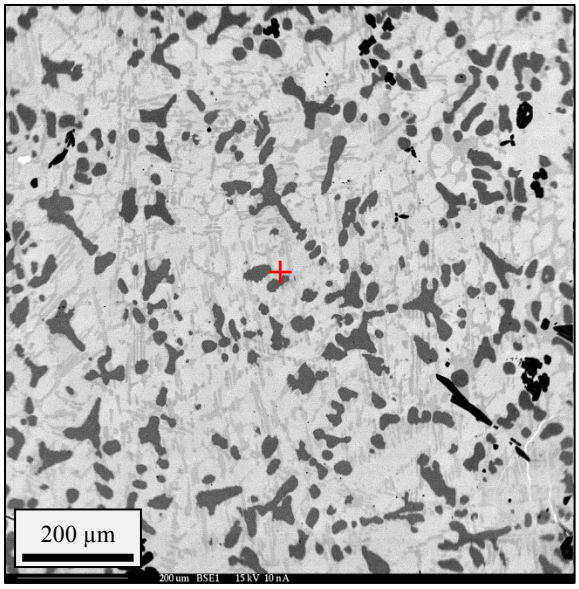

(a) Magnification = ~90x

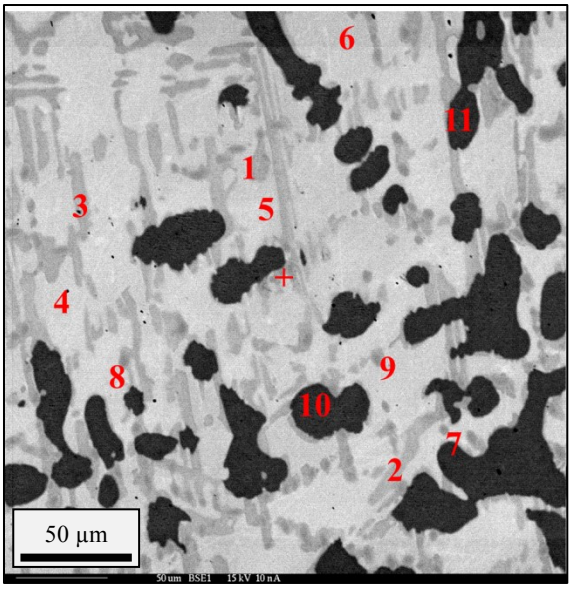

(b) Magnification = ~300x

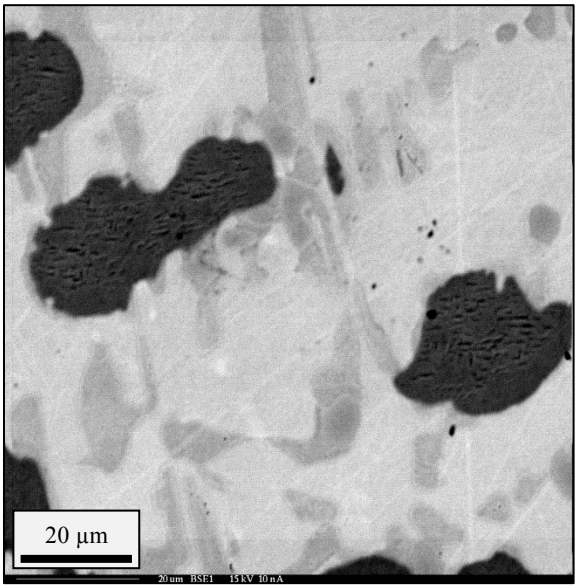

(c) Magnification = ~1000x

Figure 4-21: Backscattered electron images from Group BHT Zr-12Fe-15Cu alloy: (a) 90x, (b) 300x, and (c) 1000x.

Table 4-16: Phase composition from WDS for Group BHT Zr-12Fe-15Cu.

SPOT (FIG. 4-21B)	COLOR DESCRIPTION	ATOM PERCENT			WEIGHT PERCENT			
		Fe	Cu	Zr	Fe	Cu	Zr	Total
1	Light Gray	3.84	29.03	67.13	2.65	22.76	75.55	100.96
2	Light Gray	3.87	28.95	67.18	2.66	22.68	75.53	100.87
3	Light Gray	3.93	29.33	66.74	2.71	23.08	75.39	101.19
4	Bulk Gray	21.64	11.43	66.93	15.13	9.09	76.44	100.66
5	Bulk Gray	20.66	12.14	67.20	14.48	9.68	76.95	101.11
6	Bulk Gray	20.81	12.25	66.94	14.56	9.75	76.51	100.82
7	Intermediate Gray	20.26	12.51	67.23	13.94	9.79	75.54	99.26
8	Intermediate Gray	21.31	11.02	67.67	14.65	8.62	75.95	99.21
9	Intermediate Gray	20.94	11.79	67.27	14.37	9.21	75.42	99.01
10	Dark Gray	19.74	29.25	51.01	14.63	24.66	61.74	101.03
11	Dark Gray	19.55	29.42	51.03	14.46	24.76	61.65	100.87

From Table 4-16 and Fig. 4-21 it was apparent that there are three phases observed in the axial images corresponded well to the following:

SPOTS 1-3: Apparent Zr_2M intermetallic (M = Fe and Cu, Cu-rich)

SPOTS 4-6: Apparent Zr_2M intermetallic (M = Fe and Cu, Fe-rich)

SPOTS 7-9: Apparent Zr_2M intermetallic (M = Fe and Cu, Fe-rich)

SPOTS 10-11: Apparent ZrM intermetallic

This alloy, like the 10Cu alloy, had a complex microstructure consisting of 4 different intermetallic phases, including three apparent Zr_2M phases, two of which were compositionally identical but had distinct morphologies. The first was a Cu rich intermetallic phases which formed a coarse matrix of precipitates, forming a web within the bulk intermetallic phase which also had an seeming Zr_2M structure. The bulk intermetallic phase was much more Fe rich with a 2:1 ratio between the Fe and Cu concentrations. The third phase consisted of roughly the same elemental composition of the bulk matrix phase, however appeared as much darker intermediate gray precipitates represented by spots 7-9 in Fig. 4-21b. Additionally, this intermediate gray phase appeared to form exclusively within the light gray Cu rich phases and not within the bulk phases. Finally, there was a dark gray

phase which consisted of a roughly 1:1 ratio of Fe and Cu to Zr and a roughly 2:3 ratio of Fe to Cu.

4.1.3.4. Summary of B Heat Treated Alloys

Overall the annealed alloys exhibited much more uniform phase structures as compared to the as-cast alloys. Although still complex and with multiple structures present in each alloy, the variations within those structures was much smaller. The first alloy which had a Cu concentration of 5 wt% was the least complex consisting of only 3 different phases. The Zr-12Fe-10Cu alloy shared many of the same features as the alloy with 5Cu, but was much more complex and consisted of no less than five different phases with the possibility of a sixth phase present. The particle size of the unidentified phase was less than a micron, therefore, WDS analysis could not be performed. The third alloy (15Cu) appeared just as complex as and consisted of 4 different intermetallic phases, three of which appeared to have the same structure. One feature present in all three of the alloys was increased brittleness as shown in the increased cracking and pitting as a result of polishing seen in the optical scans at the beginning of the section. Many of the cracks and holes seen in the optical scans were not present in the samples prior to polishing.

4.1.4. Group C As-cast Alloys

Due to specific sample dimension requirements, this third casting was performed (Group C) in order to use LFA for analysis. No changes were made in the casting procedure or alloy compositions as the results from the Group B casting were satisfactory. Therefore, Groups B and C should be relatively identical.

The figures in the following sections present backscattered electron (BSE) images. As with Groups A and B, the radial section was cut from the bottom half of the sample while the axial section was cut from the top half of the samples. This was done to determine whether the samples morphologies were uniform. The low magnification “optical scans” from the electron microprobe are show in Figs. 4-22 and 4-23. It is notable that all three

alloys exhibited multiple brittle cracks in both the axial and radial section with the exception of the Zr-12Fe-15Cu alloy radial sections which held up much better under polishing.

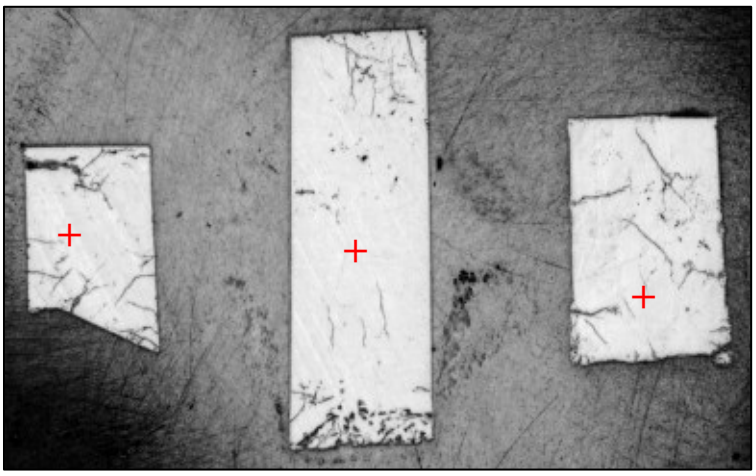

Figure 4-22: Optical scan of all three Group C axial sections: Zr-12Fe-5Cu (left), Zr-12Fe-10Cu (middle), and Zr-12Fe-15Cu (right).

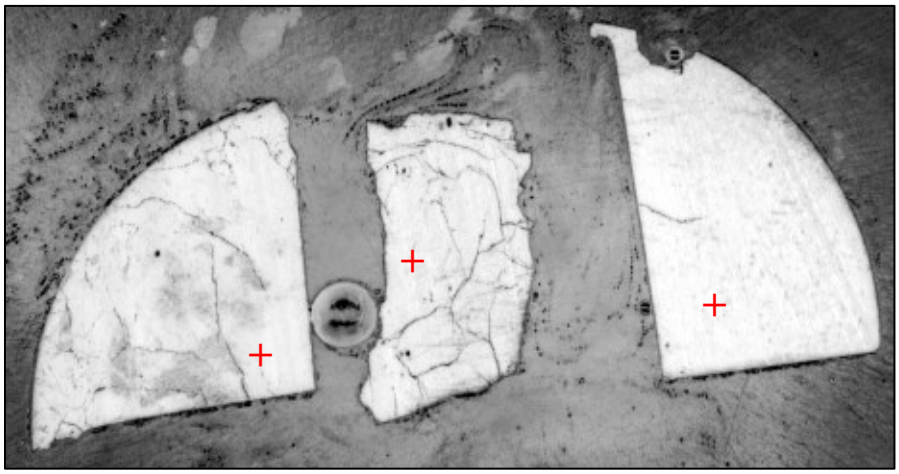

Figure 4-23: Optical scan of all three Group C radial sections: Zr-12Fe-5Cu (left), Zr-12Fe-10Cu (middle), and Zr-12Fe-15Cu (right).

4.1.4.1. Zr-12Fe-5Cu Alloy

Images from the axial and radial sections of the Zr-12Fe-5Cu alloy are presented in Figs. 4-24 and 4-25. The images were recorded at nominal magnifications of 90x, 300x, and 1000x. From Figs. 4-24 and 4-25, one can easily see that it appeared that there was uniformity as the same features seen in the axial section of the sample are also seen in the radial section of the sample.

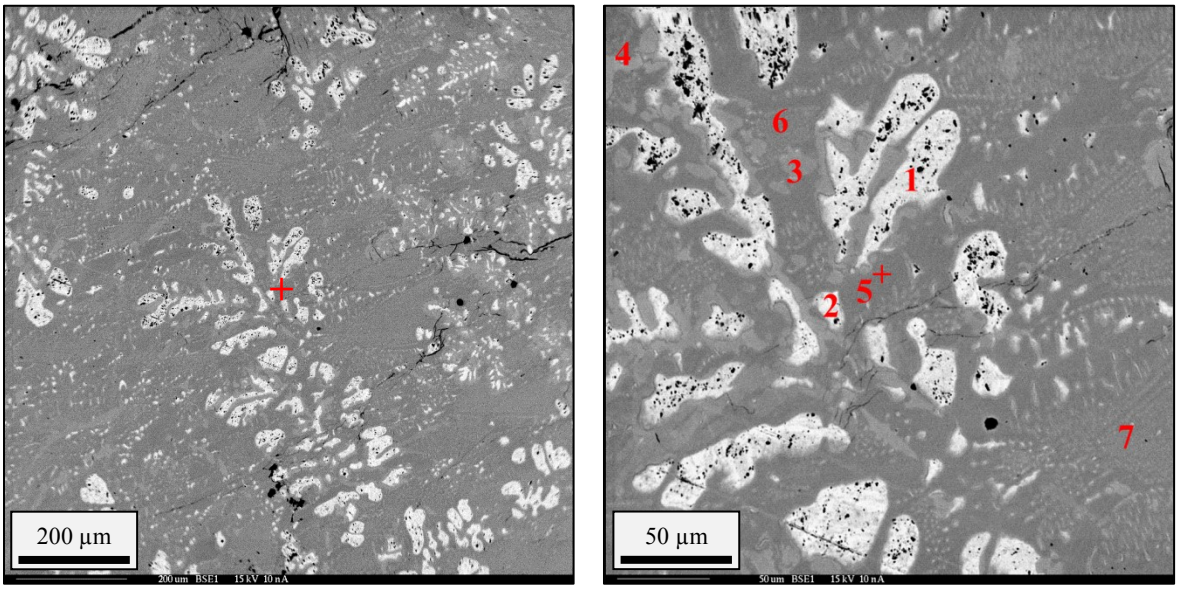

(a) Magnification = ~90x (b) Magnification = ~300x

Figure 4-24: Backscattered electron images from the axial slice of the Group C Zr-12Fe-5Cu alloy: (a) 90x, (b) 300x, and (c) 1000x.

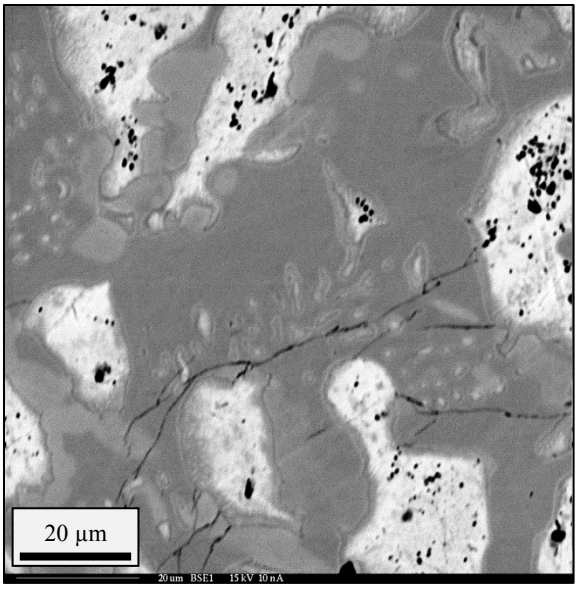

(c) Magnification = ~1000x

Figure 4-24: Continued.

Table 4-17: Phase composition from WDS for Group C Zr-12Fe-5Cu (axial).

SPOT (FIG. 4-24B)	COLOR DESCRIPTION	ATOM PERCENT			WEIGHT PERCENT			
		Fe	Cu	Zr	Fe	Cu	Zr	Total
1	White	3.25	2.09	94.66	2.03	1.48	96.53	100.04
2	White	0.65	1.59	97.76	0.41	1.12	98.99	100.51
3	Light Gray	21.33	3.61	75.06	14.47	2.79	83.18	100.44
4	Light Gray	21.09	3.63	75.28	14.26	2.80	83.15	100.21
5	Bulk Gray	25.45	7.35	67.21	17.91	5.88	77.27	101.07
6	Bulk Gray	25.02	7.03	67.95	17.57	5.62	77.95	101.14
7	Bulk Gray	21.12	6.21	72.67	14.44	4.83	81.12	100.39

From Table 4-17 and Fig. 4-24 it was apparent that there are three phases observed in the axial images corresponded well to the following:

SPOTS 1-2: Zr solution phase with limited solubility for Fe and Cu

SPOTS 3-4: Apparent Zr_3M intermetallic (M = Fe and Cu)

SPOTS 5-7: Apparent Zr_2M intermetallic (M = Fe and Cu)

Table 4-18: Phase composition from WDS for Group C Zr-12Fe-5Cu (radial).

SPOT (FIG. 4-25B)	COLOR DESCRIPTION	ATOM PERCENT			WEIGHT PERCENT			
		Fe	Cu	Zr	Fe	Cu	Zr	Total
1	White	3.84	2.47	93.69	2.40	1.76	95.73	99.90
2	White	3.01	2.17	94.82	1.88	1.54	96.68	100.10
3	Light Gray	20.75	4.04	75.21	14.08	3.12	83.34	100.54
4	Light Gray	20.69	3.84	75.48	14.00	2.95	83.43	100.38
5	Bulk Gray	23.93	8.83	67.24	16.80	7.05	77.09	100.94
6	Bulk Gray	25.45	7.34	67.20	17.94	5.89	77.37	101.20
7	Bulk Gray	24.00	8.56	67.45	16.92	6.86	77.65	101.43

From Table 4-18 and Fig. 4-25 it was apparent that there are three phases observed in the axial images corresponded well to the following:

SPOTS 1-2: Zr solution phase with limited solubility for Fe and Cu

SPOTS 3-4: Apparent Zr_3M intermetallic (M = Fe and Cu)

SPOTS 5-7: Apparent Zr_2M intermetallic (M = Fe and Cu)

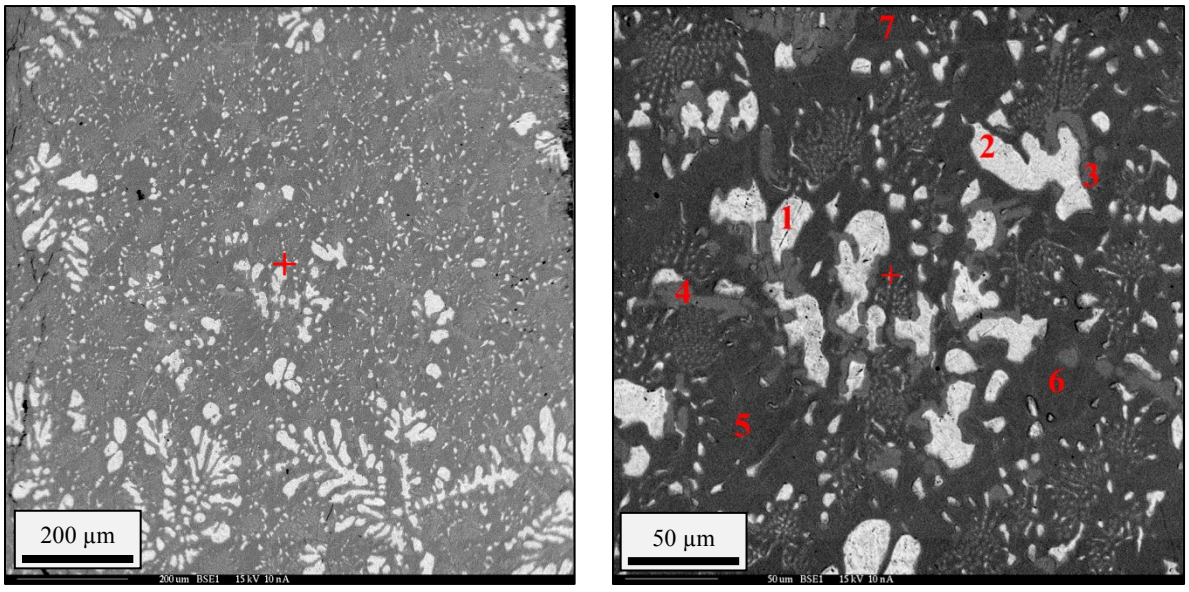

(a) Magnification = ~90x (b) Magnification = ~300x

Figure 4-25: Backscattered electron images from the radial slice of the Group C Zr-12Fe-5Cu alloy: (a) 90x, (b) 300x, and (c) 1000x.

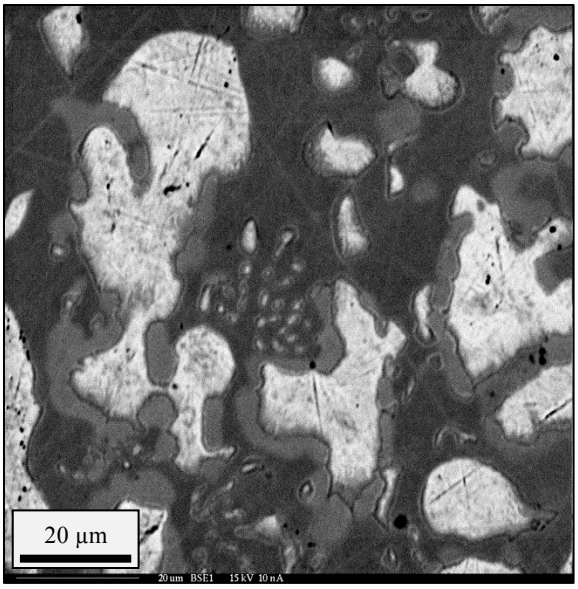

(c) Magnification = ~1000x

Figure 4-25: Continued.

Each of the two sections consisted of the same three phase morphologies listed above. The size and distribution of the Zr solution phases appeared to be more uniform across the top and bottom of the samples as compared to Group B which exhibited a variation in the size of the Zr precipitates. Both sections consisted of large dendritic structures accompanied by smaller Zr precipitates on the order of sub-micron. The sub-micron Zr structures could only be seen when zoomed in to 1000x as shown in Figs. 4-24c and 4-25c. Cracking was ubiquitous in each sample, however it was much more difficult to find a position on the axial section which didn't contain any cracking. The black particles which appear in the axial section are not another phase but rather SiC particles which were artifacts from polishing trapped in the softer Zr precipitates. Surrounding the Zr solution phase was the second phase made up of the Fe rich intermetallic Zr_3M phase. Finally, the third phase was the bulk Zr_2M intermetallic phase which had moderate variations in the Fe and Cu concentrations. The bulk Zr_2M in the axial section (Fig. 4-24) also showed a variation in the elemental composition of Zr, as noted in Spot 7. As noted in Section 3.2.2, the interaction area formed by the electron beam penetrates approximately 1 µm into the surface. Therefore the sudden increase in Zr

concentration may have been the result of a Zr precipitate just below the surface of the measured area contributing to the WDS measurement.

4.1.4.2. Zr-12Fe-10Cu Alloy

Images from the axial and radial sections of the Zr-12Fe-10Cu alloy are presented in Figs. 4-26 and 4-27. The images were recorded at nominal magnifications of 90x, 300x, and 1000x. From Figs. 4-26 and 4-27, one can easily see that it appeared that alloy was uniform as the same features seen in the axial section of the sample are not seen in the radial section of the sample. Again it seems that the sample was Zr rich in the top half of the sample. This was consistent with the two previous castings. LFA analysis was done on both ends of the sample to determine whether there was a significant difference between the thermal properties of the two halves of the sample.

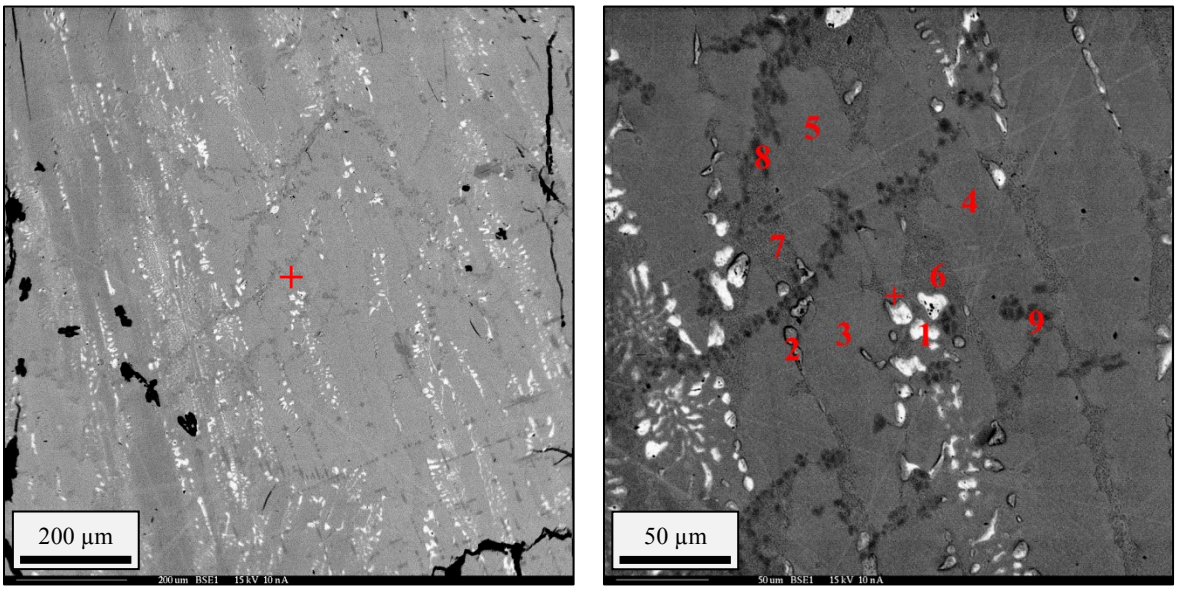

(a) Magnification = ~90x (b) Magnification = ~300x

Figure 4-26: Backscattered electron images from the axial slice of the Group C Zr-12Fe-10Cu alloy: (a) 90x, (b) 300x, and (c) 1000x

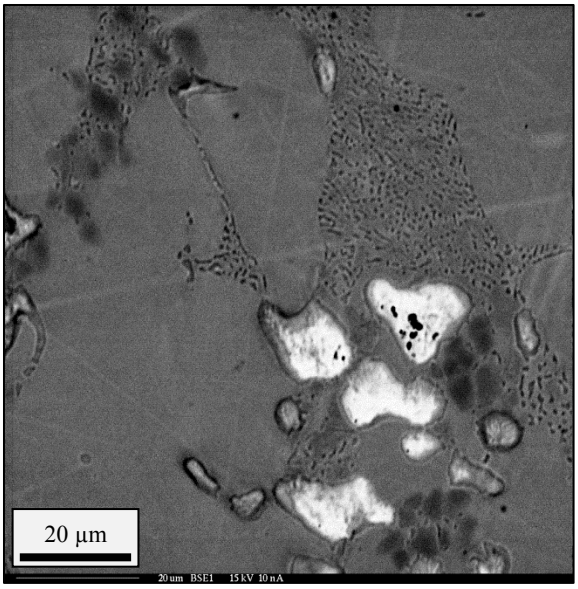

(c) Magnification = ~1000x

Figure 4-26: Continued.

Table 4-19: Phase composition from WDS for Group C Zr-12Fe-10Cu (axial).

SPOT (FIG. 4-26B)	COLOR DESCRIPTION	ATOM PERCENT			WEIGHT PERCENT			
		Fe	Cu	Zr	Fe	Cu	Zr	Total
1	White	0.58	0.94	98.48	0.36	0.66	99.37	100.38
2	White	2.64	1.93	95.43	1.58	1.31	93.30	96.19
3	Bulk Gray	19.10	14.02	66.88	13.42	11.22	76.79	101.43
4	Bulk Gray	22.15	11.05	66.81	15.59	8.85	76.81	101.24
5	Bulk Gray	21.24	11.99	66.77	15.03	9.65	77.14	101.82
6	Intermediate Gray	12.81	15.97	71.22	8.74	12.39	79.32	100.45
7	Intermediate Gray	13.55	15.51	70.94	9.27	12.08	79.29	100.64
8	Dark Gray	21.71	10.28	68.01	14.96	8.06	76.57	99.59
9	Dark Gray	21.59	10.57	67.83	14.91	8.31	76.50	99.72

From Table 4-19 and Fig. 4-26 it was apparent that there are three phases observed in the axial images corresponded well to the following:

SPOTS 1-2: Zr solution phase with limited solubility for Fe and Cu

SPOTS 3-5: Apparent Zr_2M intermetallic (M = Fe and Cu)

SPOTS 6-7: Apparent Zr_3M intermetallic (M = Fe and Cu)

SPOTS 8-9: Apparent Zr_2M intermetallic (M = Fe and Cu)

Table 4-20: Phase composition from WDS for Group C Zr-12Fe-10Cu (radial).

SPOT (FIG. 4-27B)	COLOR DESCRIPTION	ATOM PERCENT			WEIGHT PERCENT			
		Fe	Cu	Zr	Fe	Cu	Zr	Total
1	Bulk Gray	21.53	11.09	67.38	15.15	8.88	77.42	101.45
2	Bulk Gray	21.32	11.44	67.24	15.06	9.20	77.58	101.83
3	Bulk Gray	20.36	12.33	67.31	14.35	9.89	77.51	101.76
4	Intermediate Gray	4.74	27.69	67.57	3.28	21.82	76.44	101.54
5	Intermediate Gray	4.50	28.29	67.21	3.10	22.21	75.76	101.08
6	Dark Gray	21.71	10.22	68.07	14.98	8.03	76.72	99.73
7	Dark Gray	21.94	10.19	67.88	15.15	8.01	76.57	99.73

From Table 4-20 and Fig. 4-27 it was apparent that there are three phases observed in the axial images corresponded well to the following:

SPOTS 1-3: Apparent Zr_2M intermetallic (M = Fe and Cu, Fe-rich)

SPOTS 4-5: Apparent Zr_2M intermetallic (M = Fe and Cu, Cu-rich)

SPOTS 6-7: Apparent Zr_2M intermetallic (M = Fe and Cu, Fe-rich)

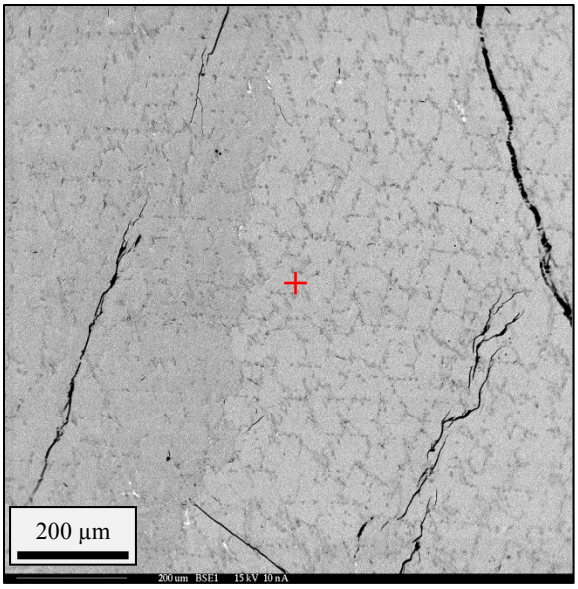

(a) Magnification = ~90x

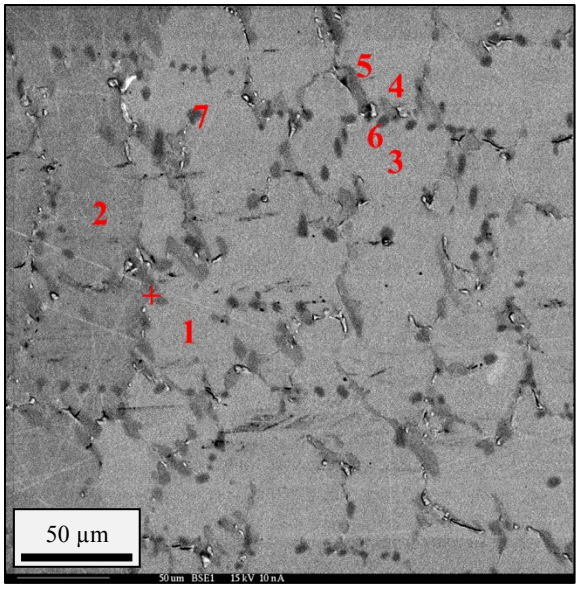

(b) Magnification = ~300x

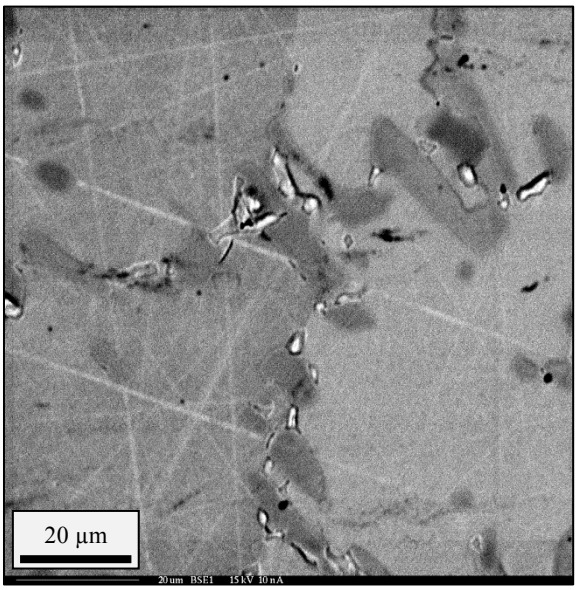

(c) Magnification = ~1000x

Figure 4-27: Backscattered electron images from the radial slice of the Group C Zr-12Fe-10Cu alloy: (a) 90x, (b) 300x, and (c) 1000x

Two complex phase morphologies were present in the sample, one which appeared to exhibit some of the same features as the Zr rich Zr-12Fe-5Cu alloy and one containing some of the same features as the Cu rich Zr-12Fe-15Cu alloy. The axial section consisted of four distinct phases listed above. The size and distribution of the Zr precipitates was consistent

with that of Group B with particles on the order of a few microns. The large black spots are yttria inclusions stemming from the highly reactive molten Zr consuming at the yttria oxide crucibles. The bulk intermetallic showed the same variations in the Fe and Cu concentrations while remaining consistent in the Zr concentration as seen in the previous alloys. The third phase had a roughly 1:1 Fe to Cu ratio differing by ~1-2 at% with slightly more Cu present. Additionally when expanded (Fig 4-26c), one can see that this phase is made up of extremely small black particles which couldn't be analyzed individually due to the spatial resolution of the EPMA. Finally, there were dark gray spots which contained the same Fe and Cu concentrations as the bulk gray phase. The size of the dark gray spots was on the order of 3-4 μm.

The radial section of the Zr-12Fe-10Cu alloys exhibited features not seen in any previous castings. The radial section was made up of 3 different intermetallics all having the same Zr_2M structure. The first was the bulk matrix phase which had a 2:1 ratio of Fe to Cu. There appeared to be two different bulk intermetallic phases (Spots 1 and 2 in Fig. 4-27b), however WDS determined that both shades of gray contained the same concentrations of all three alloying elements. There also appeared to be a clear grain boundary running down the very center of Fig. 4-27a. Although this was the first time this phenomenon was seen, it was also observed in later EMPA sessions and was seen in the Zr-12Fe-15Cu alloy and was indeed physical and not an artifact of polishing or carbon coating. The other two phases existed as small oval structures with the diameters between 5-10 μm. Together the two phase morphologies formed a course web within the bulk matrix phases. The dark gray phases, Spots 6-7, shared the same alloy compositions as the bulk matrix phase.

4.1.4.3. Zr-12Fe-15Cu Alloy

Images from the axial and radial sections of the Zr-12Fe-15Cu alloy are presented in Figs. 4-28 and 4-29. The images were recorded at nominal magnifications of 90x, 300x, and 1000x. This alloy continued to be the toughest of the three alloys in that it sustained the least amount of cracking and pitting during polishing. Additionally, it showed the least amount of scratching, especially at high magnification (1000x).

There were 4 different intermetallic phases, including three variations of the Zr_2M phase. The first was a light gray Cu rich phase which formed long strands throughout the bulk phase. The Cu to Fe ratio was 7:1 which was consistent to previous castings. The next two phases shared the same compositional features, however differed greatly in physical characteristics. Both have a 2:1 ratio of Fe to Cu, however of the two phases, the first phase forms the bulk matrix of the alloy microstructure, while the second, darker phase, existed as small cruciform or square structures within the bulk matrix in the axial section. The size and shape of the intermediate gray phase changed in the radial half of the sample. In the bottom half, the intermediate gray phase was much smaller and were circular in shape with diameters between 1 and 3 μm. Finally, the last phase had a 2:3 ratio of Fe to Cu and had irregular shapes of varying sizes ranging from tens of microns to a just few microns across. The distribution of the fourth phase differed between the top and bottom of the alloy slug. In the top half of the sample, the dark gray islands were sparser as compared to the bottom half suggesting that the top half was more Zr rich. This was consistent with what was seen in the past as the Zr seemed to preferentially migrate to the top of the sample even after inverting the slug for the second casting.

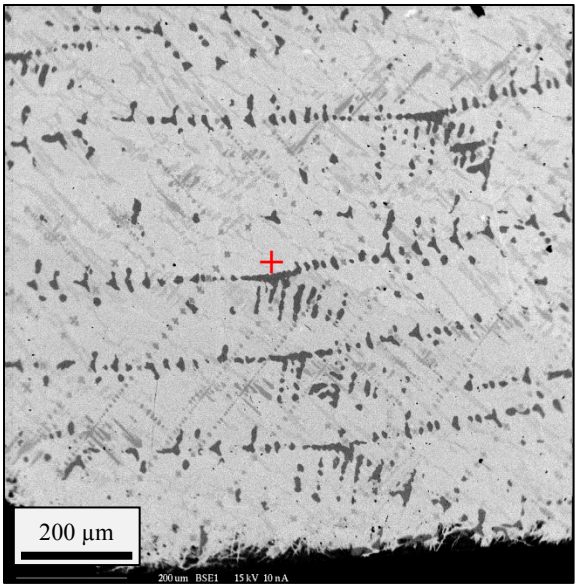

(a) Magnification = ~90x

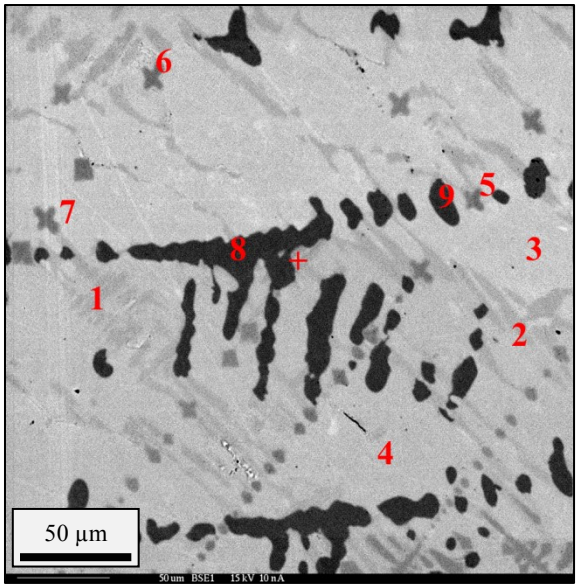

(b) Magnification = ~300x

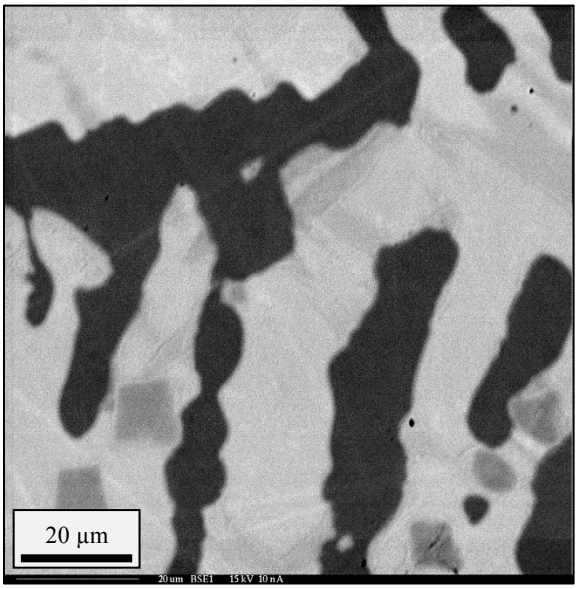

(c) Magnification = ~1000x

Figure 4-28: Backscattered electron images from the axial slice of the Group C Zr-12Fe-15Cu alloy: (a) 90x, (b) 300x, and (c) 1000x

Table 4-21: Phase composition from WDS for Group C Zr-12Fe-15Cu (axial).

SPOT (FIG. 4-28B)	COLOR DESCRIPTION	ATOM PERCENT			WEIGHT PERCENT			
		Fe	Cu	Zr	Fe	Cu	Zr	Total
1	Light Gray	4.28	28.82	66.91	2.95	22.63	75.44	101.02
2	Light Gray	4.42	28.75	66.83	3.05	22.60	75.38	101.03
3	Bulk Gray	20.97	12.06	66.97	14.69	9.62	76.66	100.97
4	Bulk Gray	20.19	12.92	66.89	14.18	10.33	76.73	101.24
5	Intermediate Gray	20.50	11.81	67.69	14.02	9.19	75.61	98.82
6	Intermediate Gray	20.41	11.91	67.69	13.93	9.25	75.47	98.65
7	Intermediate Gray	20.67	11.80	67.53	14.15	9.19	75.53	98.87
8	Dark Gray	20.43	28.86	50.71	15.28	24.56	61.94	101.78
9	Dark Gray	20.48	28.93	50.59	15.32	24.63	61.82	101.77

From Table 4-21 and Fig. 4-28 it was apparent that there are three phases observed in the axial images corresponded well to the following:

SPOTS 1-2: Apparent Zr_2M intermetallic (M = Fe and Cu, Cu-rich)

SPOTS 3-4: Apparent Zr_2M intermetallic (M = Fe and Cu, Fe-rich)

SPOTS 5-7: Apparent Zr_2M intermetallic (M = Fe and Cu, Fe-rich)

SPOTS 8-9: Apparent ZrM intermetallic (M = Fe and Cu)

Table 4-22: Phase composition from WDS for Group C Zr-12Fe-15Cu (radial).

SPOT (FIG. 4-29B)	COLOR DESCRIPTION	ATOM PERCENT			WEIGHT PERCENT			
		Fe	Cu	Zr	Fe	Cu	Zr	Total
1	Light Gray	4.42	28.65	66.93	3.06	22.60	75.80	101.46
2	Light Gray	4.26	28.87	66.87	2.97	22.89	76.13	102.00
3	Bulk Gray	19.38	13.51	67.10	13.67	10.85	77.31	101.83
4	Bulk Gray	19.21	13.69	67.10	13.52	10.97	77.17	101.66
5	Intermediate Gray	19.68	12.68	67.64	13.56	9.94	76.12	99.62
6	Intermediate Gray	19.56	12.84	67.60	13.47	10.06	76.04	99.57
7	Dark Gray	19.19	30.06	50.75	14.42	25.71	62.31	102.44
8	Dark Gray	19.02	30.12	50.86	14.24	25.65	62.18	102.06

From Table 4-22 and Fig. 4-29 it was apparent that there are three phases observed in the axial images corresponded well to the following:

SPOTS 1-2: Apparent Zr_2M intermetallic (M = Fe and Cu, Cu-rich)

SPOTS 3-4: Apparent Zr_2M intermetallic (M = Fe and Cu, Fe-rich)

SPOTS 5-6: Apparent Zr_2M intermetallic (M = Fe and Cu, Fe-rich)

SPOTS 7-8: Apparent ZrM intermetallic (M = Fe and Cu)

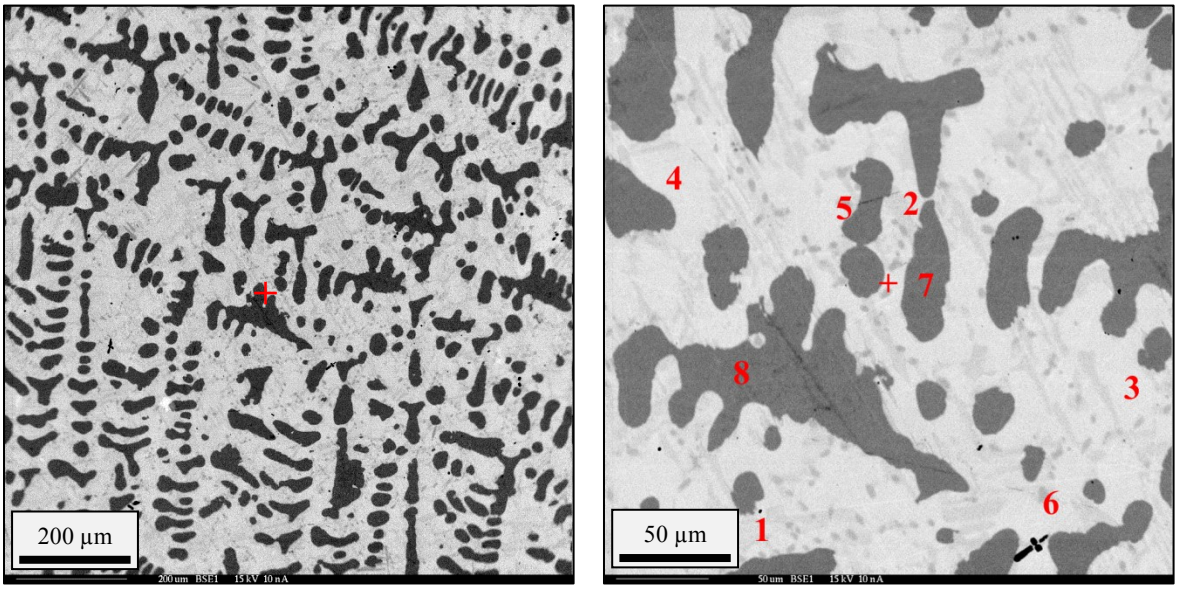

(a) Magnification = ~90x (b) Magnification = ~300x

Figure 4-29: Backscattered electron images from the radial slice of the Group C Zr-12Fe-15Cu alloy: (a) 90x, (b) 300x, and (c) 1000x

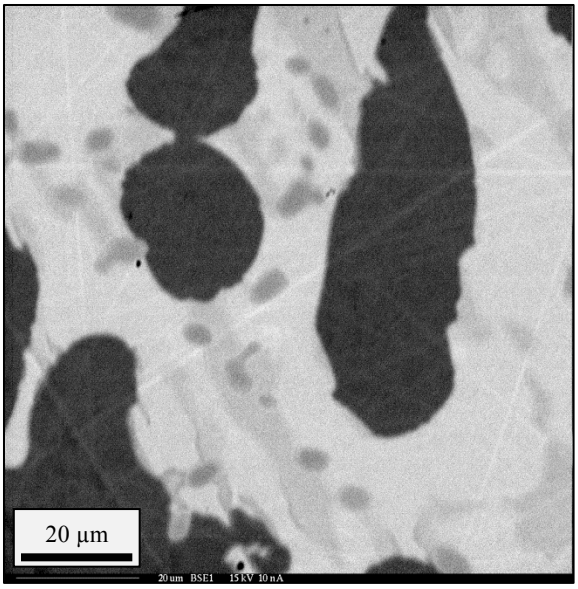

(c) Magnification = ~1000x

Figure4-29: Continued.

4.1.4.4. Summary from Group C As-cast Alloys

The principal observation from the sections above was that each of the alloys prepared and examined were indeed mixed and cast. The expected combination of phases was observed, and it appeared that relative amounts of the phases and their morphologies were more consistent, indicating homogeneous mixing, except for 10Cu, which still appeared to vary greatly between the top and bottom halves of the samples. The Zr-12Fe-5Cu alloy appeared to have more complete mixing as compared to the Group B as-cast sample. The size and distribution of the Zr solution phase was more consistent between the top and bottom of the sample. Conversely, the Zr-12Fe-15Cu alloy varied between the top and bottom half. The Zr depleted dark phase was much more dominant in the bottom half of the alloy slug, suggesting that Zr migrated to the top of the sample, a phenomena seen in all three alloys.

4.1.5. Group C Annealed Alloys[9]

In order to homogenize the samples before moving onto thermophysical analysis, each of the three alloys was heat treated in a sealed quartz vacuum tube for 1 week at 700°C (according to the procedure described in Section 3.1.4). In order to keep consistency within the testing groups, even though the LFA samples were much larger than the DSC-TGA sectioned samples, the alloys were heat treated under the same conditions. The one change was the samples were left bare inside of the quartz tubes instead of wrapping them in tantalum foil.

The Zr-12Fe-(5,10,15)Cu alloys were sectioned and prepared for microprobe analysis under the same conditions as the as-cast samples. All three samples were mounted in a single mount as shown in Fig. 4-30. Each of the alloys was sectioned from a radial sample that was cut from the middle of the alloy slug. It is notable that all three alloys exhibited multiple brittle cracks and pitting which appeared only after polishing. This is interesting to note because the polishing conditions remained unchanged, however after heat treating the samples, they became even more brittle and prone to not only cracking but also pitting during polishing. Small pieces of the alloy would break off during polishing as seen by the small black spots in Fig. 4-30 which were not present before polishing. The marker (+) in each of the images represents the general position for the backscattered electron (BSE) images taken at higher magnification.

[9] *Denoted as Group CHT*

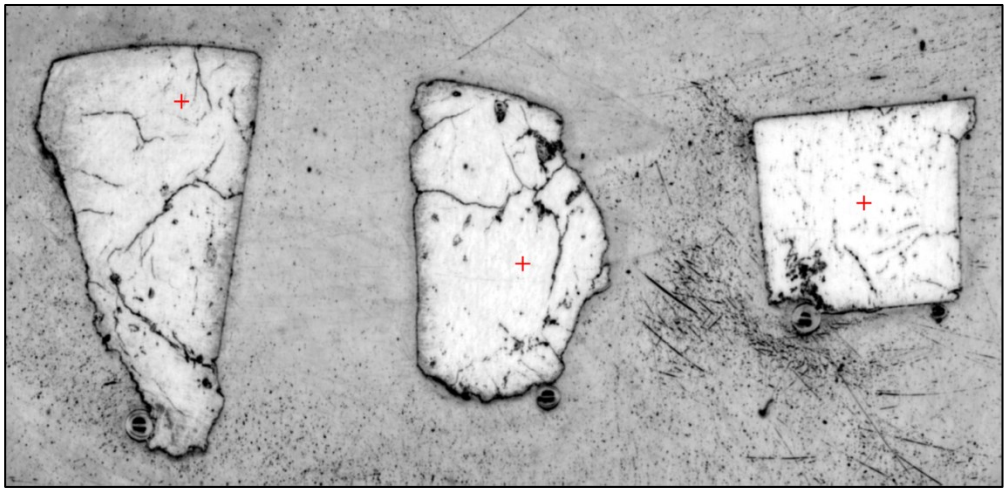

Figure 4-30: Optical scan of all three Group CHT alloys: Zr-12Fe-5Cu (left), Zr-12Fe-10Cu (middle), and Zr-12Fe-15Cu (right).

4.1.5.1. Zr-12Fe-5Cu Heat Treated Alloy

Images from the heat treated Zr-12Fe-5Cu alloy are presented in Fig 4-31. The images were recorded at nominal magnifications of 90x, 300x, and 1000x and WDS was completed to determine nominal phase compositions. Table 4-23 summarizes the WDS data.

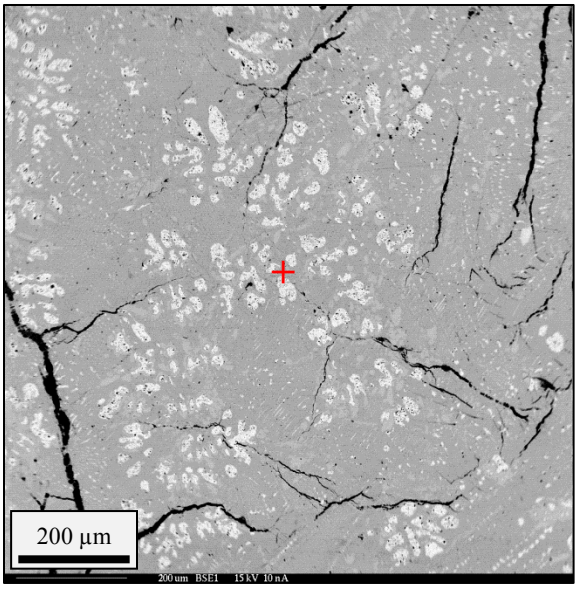

(a) Magnification = ~90x

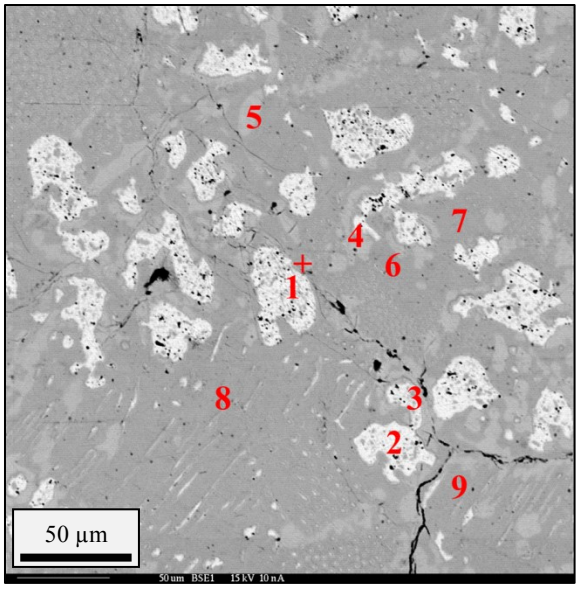

(b) Magnification = ~300x

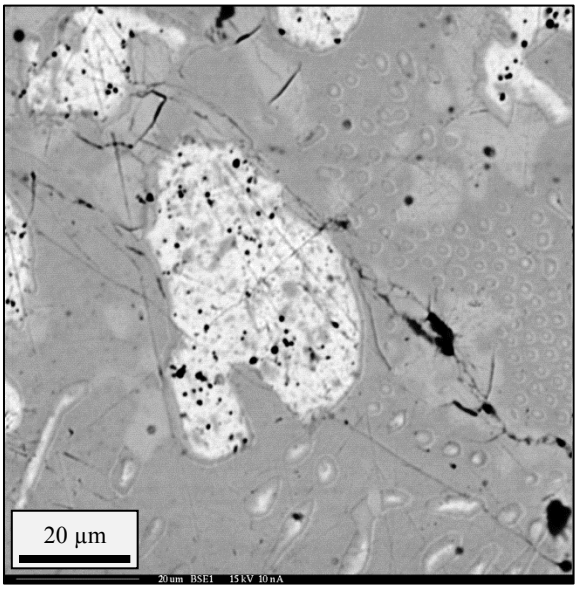

(c) Magnification = ~1000x

Figure 4-31: Backscattered electron images from Group CHT Zr-12Fe-5Cu alloy: (a) 90x, (b) 300x, and (c) 1000x.

Table 4-23: Phase composition from WDS for Group CHT Zr-12Fe-15Cu.

SPOT (FIG. 4-31B)	COLOR DESCRIPTION	ATOM PERCENT			WEIGHT PERCENT			
		Fe	Cu	Zr	Fe	Cu	Zr	Total
1	White	0.30	0.23	99.48	0.18	0.16	100.65	100.99
2	White	0.40	0.46	99.14	0.25	0.33	100.82	101.40
3	White	22.10	9.20	68.70	15.35	7.28	77.95	100.58
4	Light Gray	20.75	3.84	75.41	14.07	2.96	83.53	100.57
5	Light Gray	20.08	4.28	75.64	13.64	3.31	83.95	100.90
6	Bulk Gray	23.96	8.44	67.59	16.79	6.73	77.34	100.85
7	Bulk Gray	23.21	9.09	67.70	16.25	7.24	77.42	100.91
8	Bulk Gray	19.14	13.58	67.28	13.42	10.84	77.05	101.30
9	Bulk Gray	22.84	9.25	67.91	15.98	7.36	77.60	100.93

From Table 4-23 and Fig. 4-31 it was apparent that there are three phases observed in the axial images corresponded well to the following:

SPOTS 1-2: Zr solution phase with limited solubility for Fe and Cu

SPOTS 4-5: Apparent Zr_3M intermetallic (M = Fe and Cu)

SPOTS 6-9: Apparent Zr_2M intermetallic (M = Fe and Cu)

The annealed Group C samples appeared unchanged from the as-cast samples in both quantitative WDS analysis as well as in appearance (Fig. 4-31). Cracks were dominant throughout the entire sample and as mentioned in previous sections, many of the larger cracks appeared after annealing the samples in the quarts tubes. Many of the cracks which appeared in Fig 4-30 did however only become visible after polishing and seem to have been the direct result of EPMA sample preparation.

At first glance there appeared to only be one type of the Zr solution phase structure. However, at higher and higher magnifications (i.e. 1000x) the formation of small (< 1 μm) Zr precipitates were observed in the bulk matrix phases (Fig. 4-31c). In fact, at 300x it was hard to distinguish between the bulk matrix phase and the area where these Zr precipitates were formed. Once again, there were black SiC artifact particles trapped in the soft primary Zr precipitates as a result of polishing. Additionally, during annealing, Fe and Cu began to precipitate out of the Zr solution phase as evidenced by the small gray structures (Spot 3) present within the Zr islands. Next was the light gray intermetallic phase consisting of a

roughly 5:1 ratio of Fe to Cu forming almost exclusively in and around the Zr precipitates. The final phase to note is the bulk matrix phase which had a 2:1 ratio of Fe to Cu with fairly large variations in both the Fe and Cu concentration while the Zr elemental composition remaining statistically the same.

4.1.5.2. Zr-12Fe-10Cu Heat Treated Alloy

Images from the heat treated Zr-12Fe-10Cu alloy are presented in Fig 4-20. The images were recorded at nominal magnifications of 90x, 300x, and 1000x and WDS was completed to determine nominal phase compositions. Table 4-24 summarizes the WDS data.

Table 4-24: Phase composition from WDS for Group CHT Zr-12Fe-10Cu.

SPOT (FIG. 4-32B)	COLOR DESCRIPTION	ATOM PERCENT			WEIGHT PERCENT			
		Fe	Cu	Zr	Fe	Cu	Zr	Total
1	White	0.39	1.11	98.51	0.24	0.79	100.90	101.93
2	White	0.88	2.03	97.09	0.55	1.45	99.15	101.15
3	Light Gray	19.49	5.02	75.49	13.24	3.88	83.77	100.89
4	Light Gray	19.46	5.11	75.43	13.17	3.94	83.39	100.50
5	Light Gray	19.41	4.97	75.62	13.18	3.84	83.87	100.88
6	Bulk Gray	6.89	23.78	69.34	4.77	18.73	78.39	101.88
7	Bulk Gray	20.67	11.75	67.57	14.50	9.38	77.42	101.30
8	Bulk Gray	21.57	11.03	67.40	15.18	8.84	77.49	101.51
9	Bulk Gray	20.90	11.68	67.42	14.65	9.31	77.17	101.13
10	Dark Gray	21.42	9.92	68.66	14.64	7.72	76.65	99.02
11	Dark Gray	22.39	9.41	68.21	15.39	7.36	76.60	99.36

From Table 4-24 and Fig. 4-32 it was apparent that there are three phases observed in the axial images corresponded well to the following:

SPOTS 1-2: Zr solution phase with limited solubility for Fe and Cu

SPOTS 3-5: Apparent Zr_3M intermetallic (M = Fe and Cu)

SPOTS 7-9: Apparent Zr_2M intermetallic (M = Fe and Cu, Fe-rich)

SPOTS 10-11: Apparent Zr_2M intermetallic (M = Fe and Cu, Fe-rich)

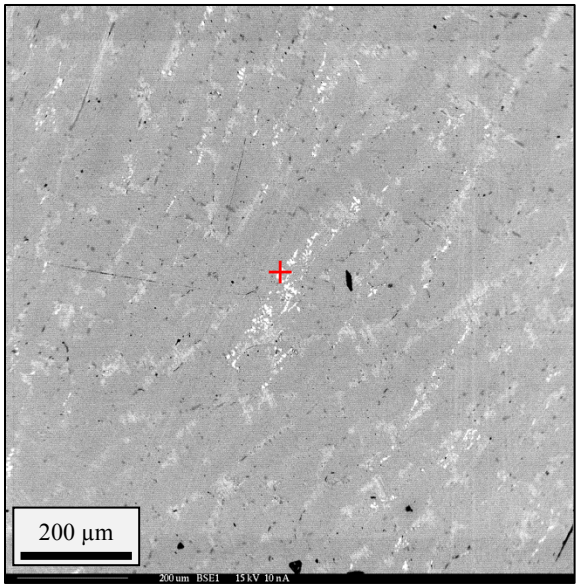

(a) Magnification = ~90x

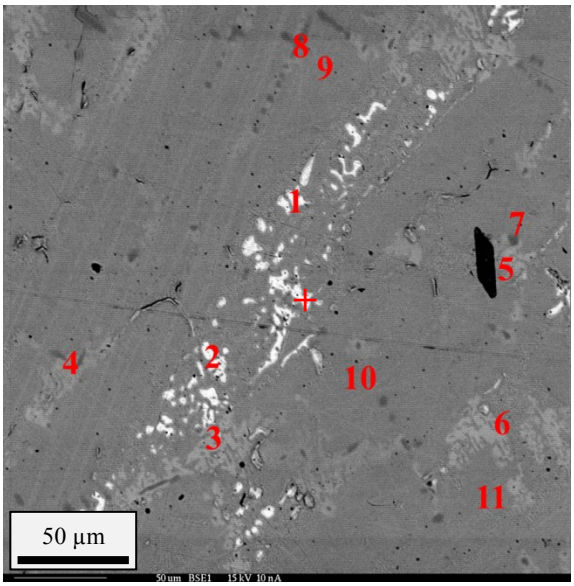

(b) Magnification = ~300x

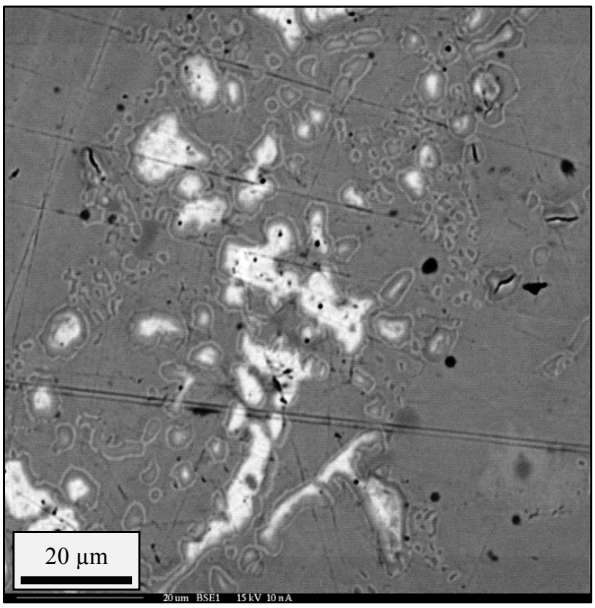

(c) Magnification = ~1000x

Figure 4-32: Backscattered electron images from Group CHT Zr-12Fe-10Cu alloy: (a) 90x, (b) 300x, and (c) 1000x.

Once again, the Zr-12Fe-10Cu alloy exhibited a fairly complex microstructure with several distinct features. There were 4 separate phases based on the four different color variations in the BSE images, however, upon examining the WDS data a Cu rich zone which is indistinguishable between the other phases becomes apparent. This can be seen in Spot 6,

which appeared to be the same as the other light gray phases but contained almost 5 times more Cu than the surrounding area. The Zr precipitates were smaller and a relatively low area fraction which was indicative of the sample coming from the middle section of the sample instead of the Zr rich top half of the samples. The bulk matrix phase had the same 2:1 Fe to Cu ratio as seen in previous samples. Finally there was a small dark gray phase which formed circular structures along the light gray phase as seen previously. The size of the dark gray structures was less than 5 μm across. The large black box next to spot 6 in Fig. 4-32 was an yttria impurity.

4.1.5.3. Zr-12Fe-15Cu Heat Treated Alloy

Images from the heat treated Zr-12Fe-15Cu alloy are presented in Fig 4-21. The images were recorded at nominal magnifications of 90x, 300x, and 1000x and WDS was completed to determine nominal phase compositions. Table 4-20 summarizes the WDS data.

The heat treated Zr-12Fe-15Cu alloy consisted of 4 different intermetallic phases, including three visually different Zr_2M phases. The first was Cu rich precipitates which formed exclusively around the large dark gray islands. Although there was a slight variation in the contrast between the bulk matrix phase and the Cu rich light gray phases, it was difficult to distinguish between the two through BSE imaging. The Cu rich zones were identified using X-ray maps of specific areas of the sample. The bulk intermetallic phase was much more Fe rich with a 2:1 ratio between the Fe and Cu concentrations. The third phase consisted of roughly the same elemental compositions of the bulk matrix phase, however appeared as much darker intermediate gray spots represented by spots 9 and 10 in Fig. 4-33b. Finally, there was a dark gray phase which consists of a roughly 1:1 ratio of Fe and Cu to Zr and a roughly 2:3 ratio of Fe to Cu. Once again the large black structures were yttria impurities that were confirmed using EDS.

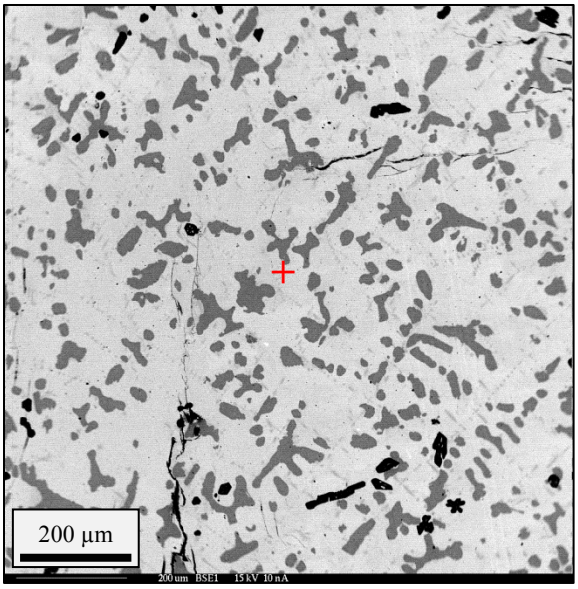

(a) Magnification = ~90x

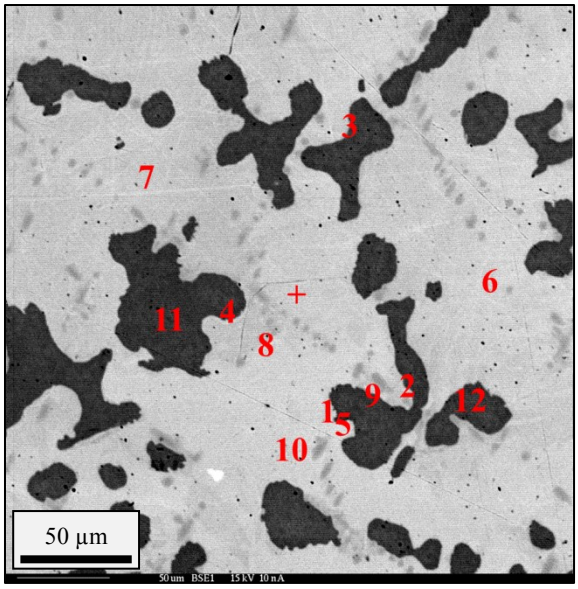

(b) Magnification = ~300x

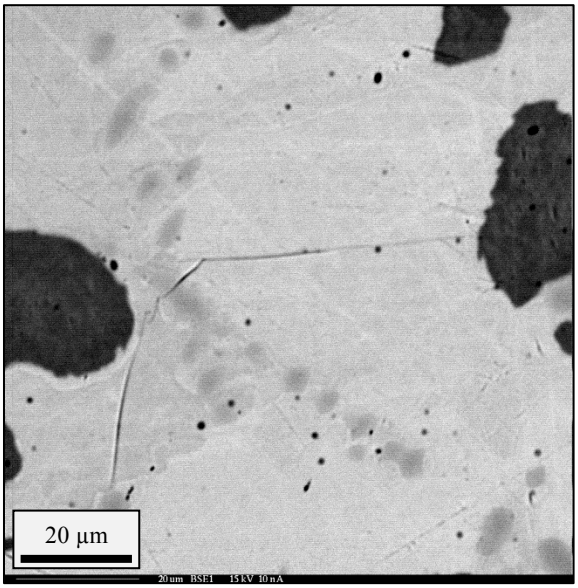

(c) Magnification = ~1000x

Figure 4-33: Backscattered electron images from Group CHT Zr-12Fe-15Cu alloy: (a) 90x, (b) 300x, and (c) 1000x.

Table 4-25: Phase composition from WDS for Group CHT Zr-12Fe-15Cu.

SPOT (FIG. 4-33B)	COLOR DESCRIPTION	ATOM PERCENT			WEIGHT PERCENT			
		Fe	Cu	Zr	Fe	Cu	Zr	Total
1	Light Gray	3.66	29.33	67.01	2.54	23.14	75.87	101.54
2	Light Gray	3.60	29.47	66.93	2.49	23.20	75.64	101.34
3	Light Gray	3.90	29.48	66.62	2.71	23.27	75.50	101.48
4	Light Gray	4.37	29.38	66.25	3.03	23.19	75.07	101.29
5	Bulk Gray	19.75	13.43	66.82	13.96	10.80	77.14	101.90
6	Bulk Gray	20.64	12.01	67.36	14.42	9.55	76.90	100.87
7	Bulk Gray	21.22	11.55	67.23	14.92	9.24	77.20	101.36
8	Bulk Gray	22.10	10.74	67.16	15.50	8.57	76.96	101.03
9	Intermediate Gray	20.36	11.90	67.74	13.96	9.29	75.89	99.14
10	Intermediate Gray	20.60	11.56	67.85	14.10	9.00	75.87	98.98
11	Dark Gray	19.68	29.38	50.94	14.63	24.84	61.84	101.31
12	Dark Gray	19.89	28.83	51.28	14.66	24.18	61.74	100.57

From Table 4-25 and Fig. 4-33 it is apparent that there are three phases observed in the axial images correspond well to the following:

SPOTS 1-4: Apparent MZr_2 intermetallic (M = Fe and Cu, Cu-rich)

SPOTS 5-8: Apparent MZr_2 intermetallic (M = Fe and Cu, Fe-rich)

SPOTS 9-10: Apparent MZr_2 intermetallic (M = Fe and Cu Fe-rich)

SPOTS 10-11: Apparent MZr intermetallic (M = Fe and Cu)

4.1.5.4. Summary of Group C Heat Treated Alloys

Overall the annealed alloys resembled the as-cast alloys in both structure and composition. It didn't appear that annealing the samples had much effect on the compositional variations in the Zr_2M phase as seen in the Group B annealing. The first which had a Cu concentration of 5 wt% was the least complex consisting of only 3 different phases. The Zr-12Fe-10Cu alloy shared many of the same features as the first alloy, but much more complex and consisted five different phases. The Zr-12Fe-15Cu sample consisted of 4 different intermetallic phases, three of which were variations of the Zr_2M phase. One feature present in all three of the alloys was increased brittleness as shown in the increased cracking and pitting as a result of polishing seen in the optical scans at the

beginning of the section. Many of the cracks and holes seen in the optical scans were not present in the samples prior to polishing. The annealing didn't appear to homogenize the samples. The samples were likely too large for the complete homogenization to occur, however, in order to keep consistency across all of the testing groups no further annealing was carried out and the heat treated alloys were tested alongside the as-cast samples using the LFA.

4.2. Melting Point and Phase Transformation Properties of Zr-Fe-Cu Alloys

Differential Scanning Calorimetry (DSC) and Thermal Gravimetric Analysis (TGA) were performed to determine the melting point and onset of phase transformations for all three alloys. Data was generated using both the as-cast and annealed Group B samples whose phase morphologies were summarized in the previous sections. First however, a set of preliminary measurements were completed to determine a suitable annealing temperature. After a suitable annealing temperature was determined the phase transformation behavior of the Zr-12-(5,10,15)Cu alloys was observed from 25°C to 1200°C. The results of the DSC-TGA are summarized in the following sections.

4.2.1. Preliminary Annealing Temperature Measurements

Preliminary DSC-TGA measurements were carried out in order to determine the max temperature that the for sample annealing, that is, these measurements were set up to determine the minimum phase transition temperature of all three alloys which would act as the limiting factor for annealing. For these runs, the DSC furnace was heated up from ambient to 875°C at a rate of 5 °C/min (as per the calibration file) and then slowly cooled back down to room temperature at 5 °C/min. The max temperature was based off the 890°C isotherm pictured in Fig. 3-2 in which all three alloys are solid.

From Fig. 4-34, it is evident that there was a phase transformation that occurred at approximately 778°C. The vertical line seen at ~ 820°C isn't physical, but seems to be a result of an anomaly that occurred during the baseline crucible measurement. Additionally, there also appeared to be multiple phase transitions within the first transition, however, since

these transitions appear at a higher temperature they were not investigated further at the time. The artificial vertical line also appeared in the 10Cu and 15Cu alloys at the exact same temperature.[10] From Figs. 4-35 and 4-36, one can see that both alloys didn't appear to contain any phase transformations below 890°C, thus the minimum phase transition temperature was 778°C. As a result, it was determine that a suitable annealing temperature was 700°C.

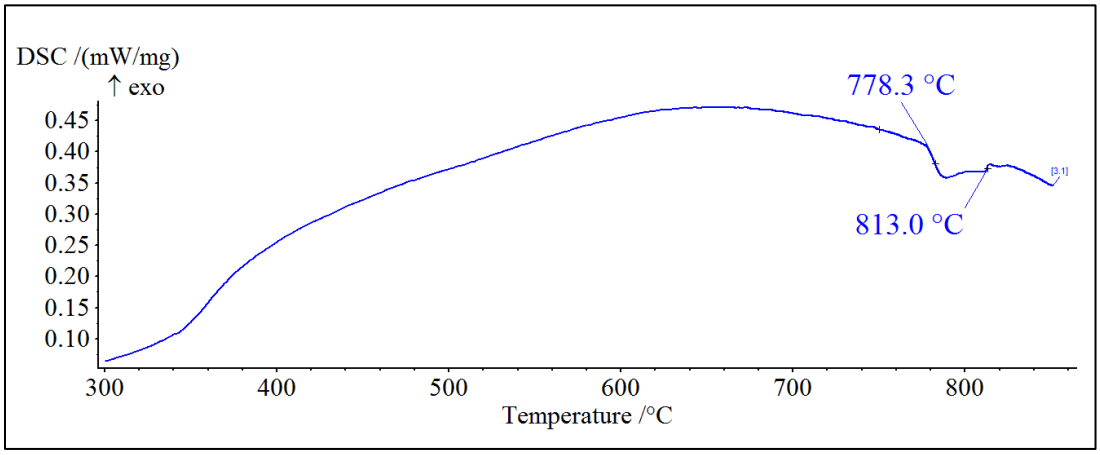

Figure 4-34: DSC curve for Zr-12Fe-5Cu alloy to determine minimum phase transformation temperature.

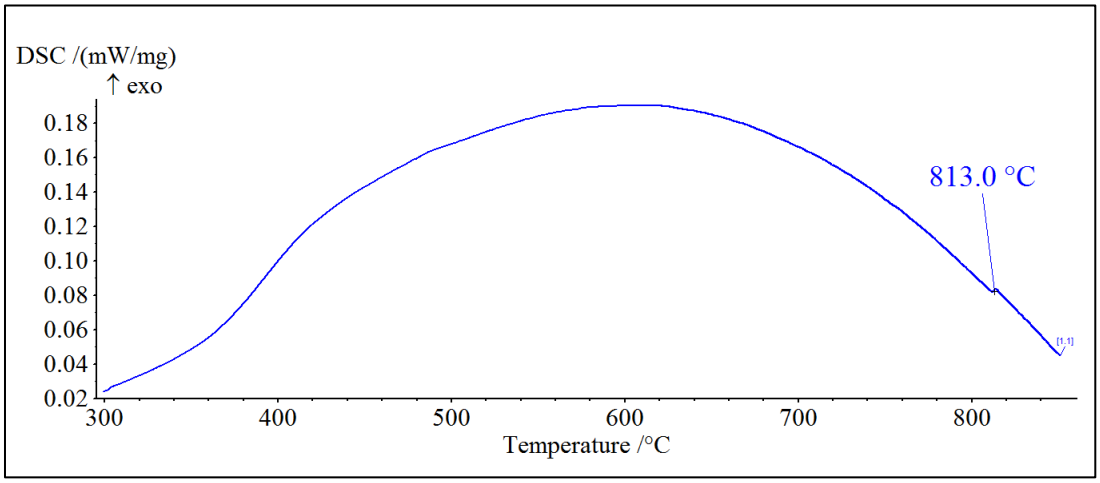

Figure 4-35: DSC curve for Zr-12Fe-10Cu alloy to determine minimum phase transformation temperature.

[10] *The same crucible was used for each run, thus the same crucible baseline was also used*

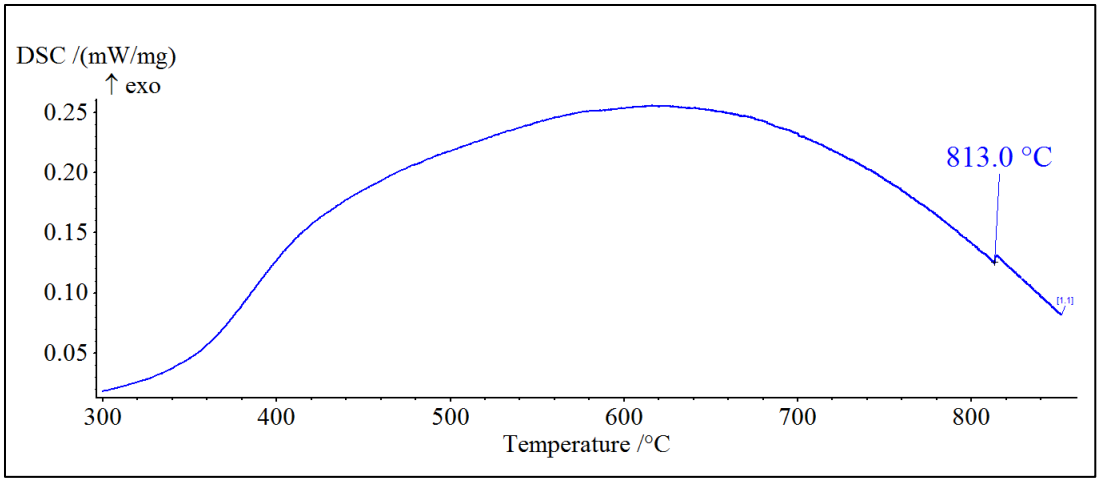

Figure 4-36: DSC curve for Zr-12Fe-15Cu alloy to determine minimum phase transformation temperature.

4.2.2. As-cast Alloys[11]

The as-cast alloys were measured as a reference for the annealed alloys. As outlined in the results, these alloys exhibited some variation in phase morphology between the top half and bottom half of the alloy slugs. In an effort to reduce the phase variation between measurements, all samples were sectioned from the same radial section from the top half of the alloy slugs. For all DSC measurements, the solid blue line represents the DSC signal curves (mW/mg) while the dashed blue line is for the Differential DSC curve which represents the change of slope in the DSC curve. Only the initial heating curve from 700°C to 1000°C is shown in each of the DSC measurements. A few of the initial alloy measurements were selected to be repeatedly cycled from 600°C to 1200°C in order to determine if the same transitions could be observed and to determine the oxidation effects and cooling behavior of the alloys. Due to those same oxidation effects, it was deemed that thermal cycling would not produce suitable and accurate data from the cooling curves as a result of hysteresis and thus only the initial heating data is reported.

[11] *Melting transitions were identified by much deeper and sharper transitions relative to the other transitions; the apparent melting transitions produced DSC signals an order of magnitude larger.*

4.2.2.1. Zr-12Fe-5Cu As-cast Alloy

There were three different transition temperatures observed as depicted in Figs. 4-37 and 4-38. The first was a very subtle transition with an onset temperature of ~782°C. The transition was very shallow and board ranging from ~782°C to ~810°C. The second exceptionally minor transition is not clearly visible in Fig. 4-37, but when the scale is expanded to view the transition more precisely, Fig. 4-38, it is evident from the DDSC curve that a transformation was observed. The transition once again was very shallow (note the x-axis units are now in 10^{-3} mW/mg), however it was not nearly as broad as the first observed transition. This is perhaps a transition within a minor component phase within the alloy. The final transition was the melt transition and had an onset temperature of 883.0°C.

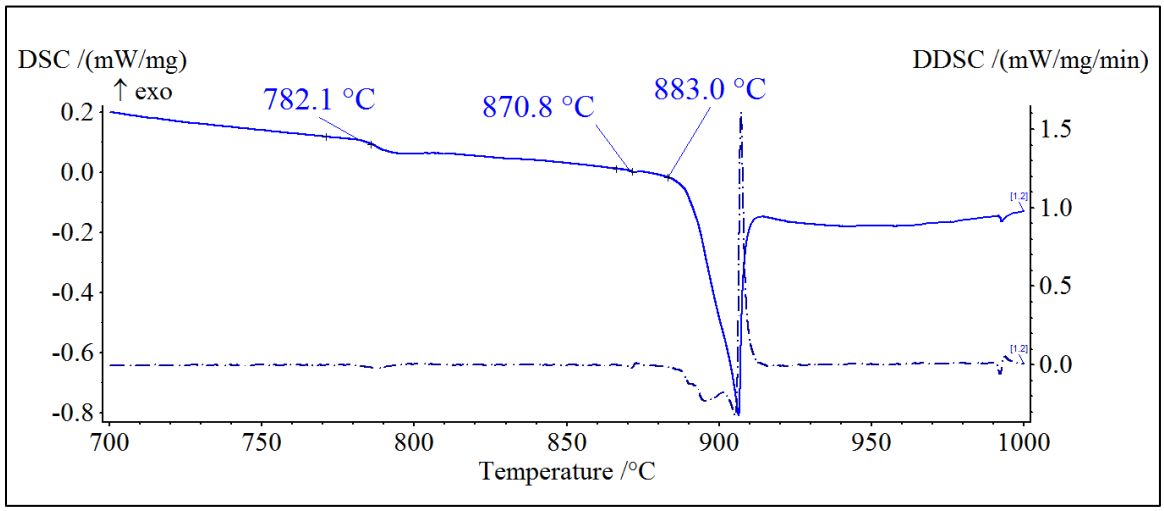

Figure 4-37: DSC heating curve for Zr-12Fe-5Cu as-cast alloy.

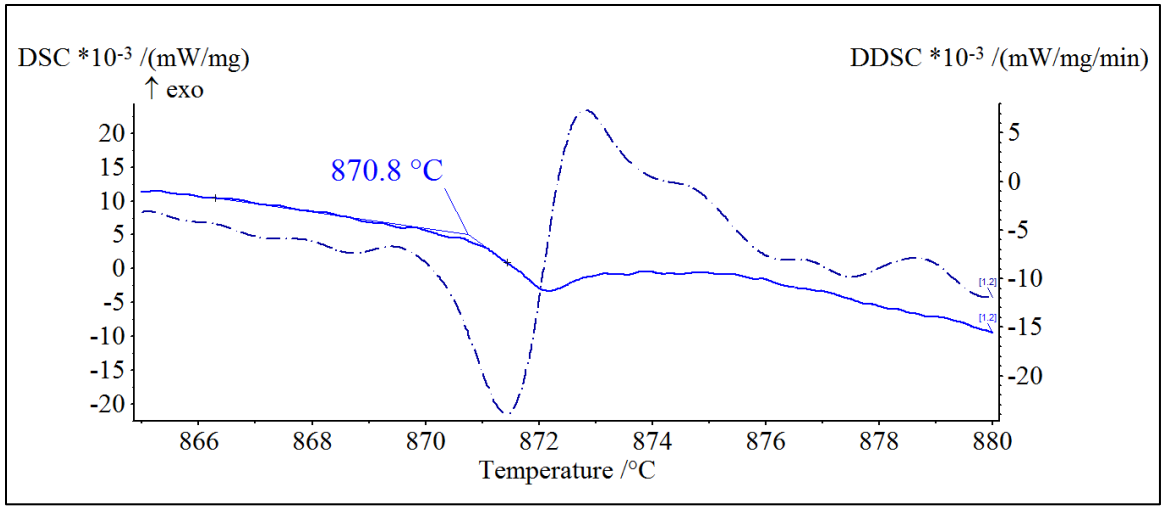

Figure 4-38: Highlight of the second transformation transition for Zr-12Fe-5Cu as-cast alloy.

4.2.2.2. Zr-12Fe-10Cu As-cast Alloy

Figure 4-39 shows the DSC heating curve for as-cast Zr-12Fe-10Cu. There were three different phase transition temperatures observed. The first was, again, a very subtle transition with an onset temperature of ~788°C. The transition was very shallow and broad ranging from ~788°C to ~810°C. The DDSC curve is not clear in this region indicating minor fluctuations at the onset only. However from the figure, there was a clear depression in the DSC curve starting at 788.0°C. There did appear to be a transition occurring before this temperature based on the DDSC curve, however no transition was observed on the actual DSC curve except a very small exothermic transition. This small exothermic transition was not seen in any of the other measurements. The second transition was the melt transition and has an onset temperature of 870.0°C. Within the melt transition was a third transition which began at 881.1°C. From the DSC curve, one can see a slight deflection at this temperature which is confirmed from the DDSC curve. This may represent a 2-step transition due to the presence of the multiple phases in the alloy.

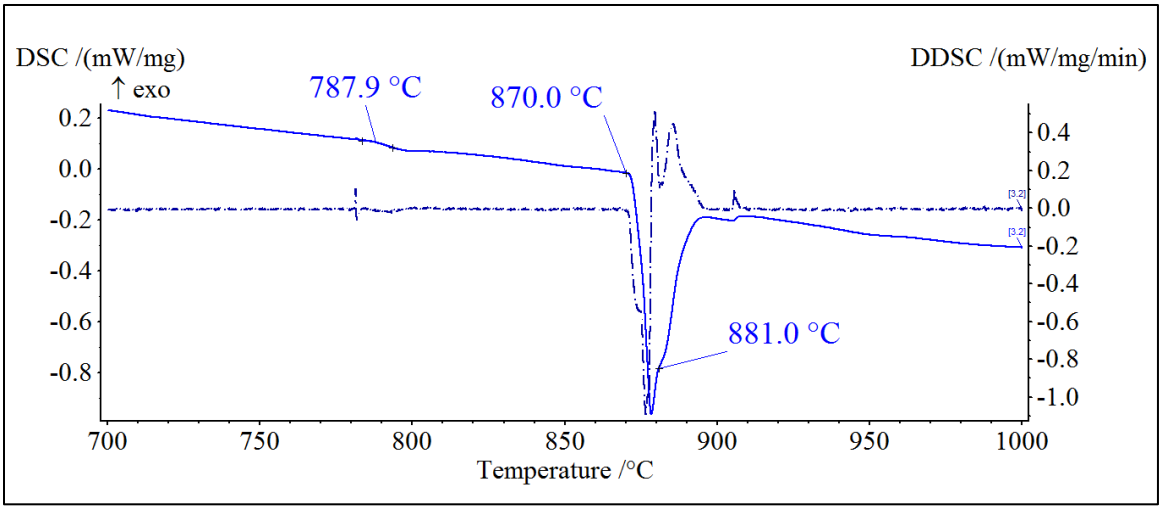

Figure 4-39: DSC heating curve for Zr-12Fe-10Cu as-cast alloy.

4.2.2.3. Zr-12Fe-15Cu As-cast Alloy

The DSC measurements from the as-cast Zr-12Fe-15Cu are shown in Figs. 4-40. There were once again three different transition temperatures observed. The first was a small transition which occurred just before melting at ~872.4°C. The second transition was the melt transition and had an onset temperature of 884.0°C. The third transition occurred at 896.5°C. The final transition once again occurred after the bulk of the alloy was presumed molten, but happened at a higher temperature than in the Zr-12Fe-10Cu alloy (Fig. 4-39) and was much clearer. From the DDSC curve, it was clear that there were three different transitions which transpired between 700°C and 1000°C.

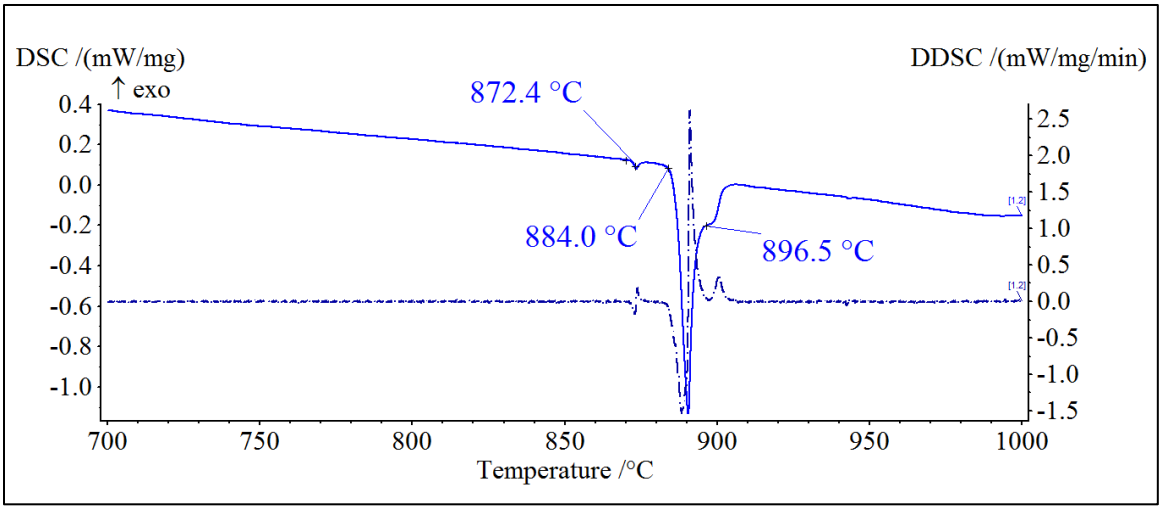

Figure 4-40: DSC heating curve for Zr-12-15Cu as-cast alloy.

4.2.2.4. Summary of As-cast DSC Measurement

The DSC measurements for the as-cast Group B alloys gave a generally good picture of the phase transitions occurring in each of the three alloys. All three alloys exhibited three transitions based on deflections and transitions seen in both the DSC and DDSC curves. The Zr-12Fe-5Cu alloy had three transitions, two of which occurred prior to melting. The first, which occurred at ~782°C, was very broad and shallow. The second transition occurred just before melting at ~871°C and like the first transition was very shallow, however it occurred much more sharply and distinctly than the first. The onset for melting in the 5Cu alloy began at 883.0°C. The 10Cu alloy also had three transitions. The first was a broad, shallow, transition starting at ~788°C and lasting until ~810°C. The second transition indicates the melting transition and occurred at 870.0°C. The final transition occurred within the melt transition and occurred 11 degrees later at 881.0°C. Similarly, in the third alloy, there were three clear transitions, one of which occurred during melting. However, the broad and shallow transition evident at ~782°C and ~788°C was not present in this alloy at all. The first transition occurred just before melting at ~872°C. Melting began at 884.0°C. Like the second alloy, there appeared to be a third transitions occurring after melting at 896.5°C.

4.2.3. Annealed Alloys

In an effort to homogenize the DSC samples to determine the true phase transition temperatures of each of the alloys, they were heat treated in a manner similar to the EPMA samples in Sections 4.1.3 and 4.1.5. Each of the alloys was heat treated at 700°C in a sealed quartz vacuum tube for 1 week (according to the procedure described in Section 3.1.4). In order to avoid sampling-generated composition variations, the heat treated samples were sectioned from the top half of each of the alloy slugs. The results of the DSC measurements are documented in the following sections.

4.2.3.1. Zr-12Fe-5Cu Annealed Alloy

There were three different phase transition temperatures observed and can be seen in Fig. 4-41. The first was again very subtle transition with an onset temperature of ~795°C. The transition was very shallow and board ranging from ~795°C to ~830°C. The transition was too gradual to be noted by the DDSC curve but from the figure there was a clear depression in the DSC curve starting at 795.0°C. There was also a second transition occurring at ~873°C right before melting. Although small, from the DDSC curve, there was a clear transition at this temperature. Like the first transition, the second transition was very shallow; however, it was also much sharper and more distinct. The final transition was the melt transition and had an onset temperature of 886.3°C.

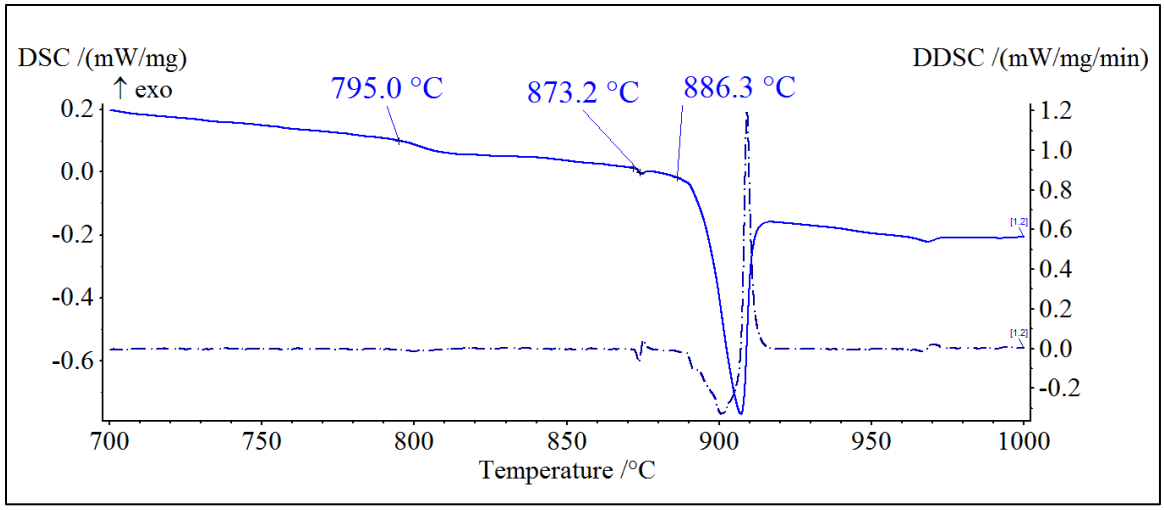

Figure 4-41: DSC heating curve for Zr-12Fe-5Cu annealed alloy.

4.2.3.2. Zr-12Fe-10Cu Annealed Alloy

The DSC measurements from the annealed Zr-12Fe-10Cu alloy is depicted in Figs. 4-42. There were three different phases transition temperatures observed. The first was again a very subtle transition with an onset temperature of ~788°C. The transition was very shallow and board ranging from ~788°C to ~810°C. The transition again was too gradual and was not noted by the DDSC curve however, there was a clear depression in the DSC curve starting at 788.0°C. The second transition was melting and had an onset temperature of 870.0°C. Within the melt transition, a third transition which occurred at 881.1°C. From the DSC curve, one can see a slight deflection at this temperature which was confirmed from the DDSC curve.

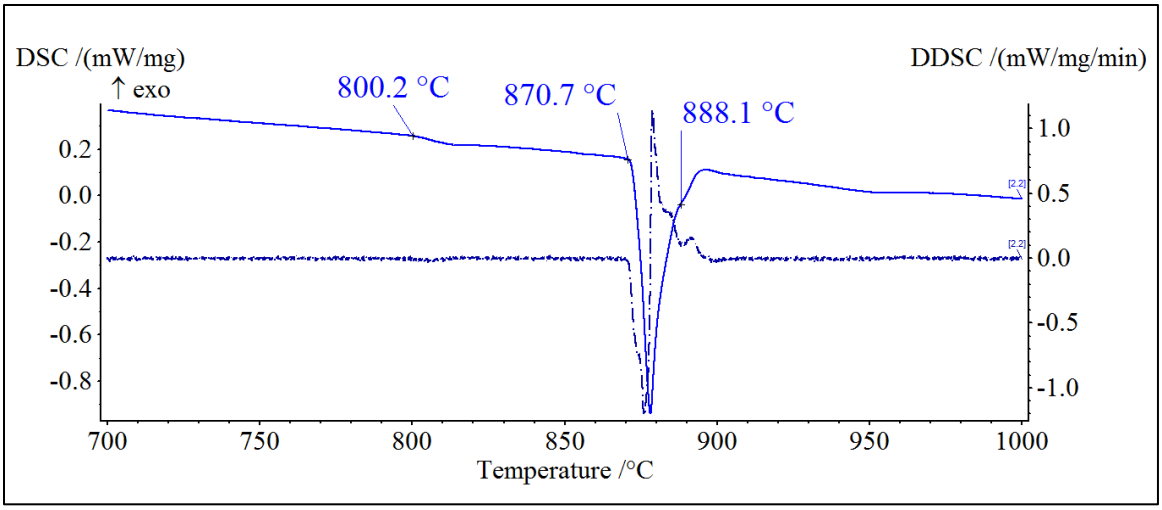

Figure 4-42: DSC heating curve for Zr-12Fe-10Cu annealed alloy.

4.2.3.3. Zr-12Fe-15Cu Annealed Alloy

The DSC measurements for the annealed Zr-12Fe-15Cu alloy are depicted in Fig. 4-43. There were only two different phase transition temperatures observed. The first transition was actually the melt transition and had an onset temperature of 884.0°C. The second transition occurred after the presumed melting transformation at 896.2°C. From the DDSC curve, it was clear that there were two different transitions which occurred between 700°C and 1000°C.

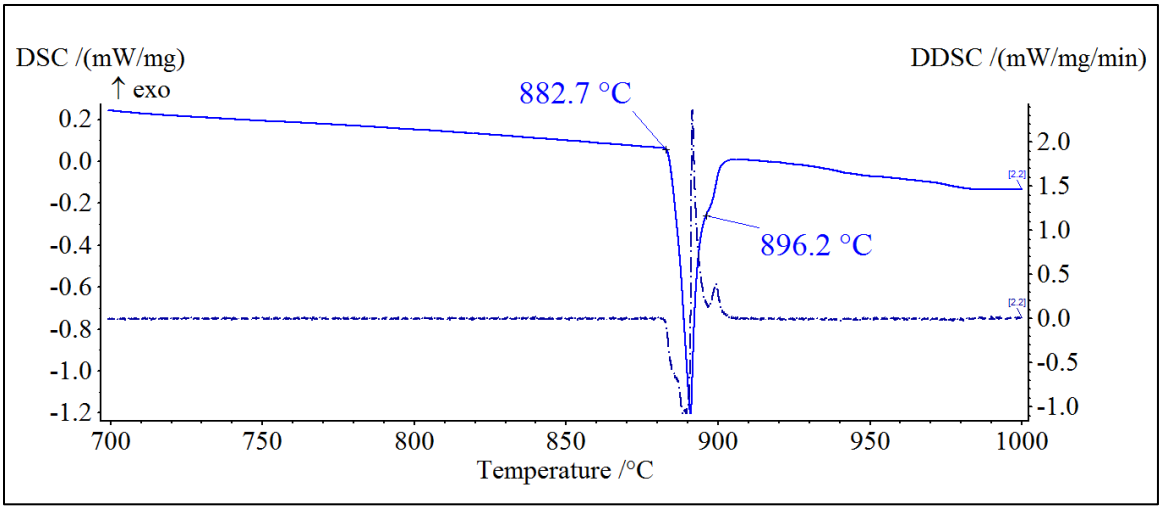

Figure 4-43: DSC heating curve for Zr-12Fe-15Cu annealed alloy.

4.2.3.4. Summary of Annealed DSC Measurements

There appeared to be little change between the as-cast alloys and the heat treated alloys. The Zr-12Fe-5Cu alloy had three transitions, two of which occurred before melting. The first, which occurred at ~795°C (shifted higher after annealing), was very broad and shallow. The second transition occurred just before melting at ~873°C and like the first transition was very shallow, however it occurred much more quickly and distinctly than the first. The onset for melting in began at 886.0°C. The second alloy, which contained 10wt% Cu, also had three transitions. The first was a broad, shallow, transition starting at ~800°C (again higher after annealing) and lasted until ~830°C. The second transition was the melt transition and occurred at 870.7°C. The final transition occurred within the melt transition and occurred approximately 11 degrees later at 881.0°C. For the Zr-12Fe-15Cu alloy, only two clear transitions were present as opposed to three in the as-cast alloy. The small pre-melting transition at ~871°C was not present in the annealed sample. Melting began at 882.7°C. Similar to the 10Cu alloy, there appeared to be another transition occurring after melting at 896.2°C.

4.3. Thermal Diffusivity Measurements of Zr-Fe-Cu Alloys

Light Flash Analysis was used to measure the thermal diffusivity of all three alloys using both the as-cast and annealed Group C samples whose phase morphologies were summarized in the Section 4.1.4 and 4.1.5. The annealed samples outlined in Section 4.1.5 were sectioned from the middle of the ingot. The LFA measurements consisted of multiple samples taken from different sections of the alloy slug, as a result the phase morphology of each of the measured samples may have varied based on the changes in Zr content noted in Section 4.1. Thermal diffusivity values were measured from ambient to 260°C. The results of the analysis are summarized in the following sections.

4.3.1. As-Cast Alloys

4.3.1.1. Zr-12Fe-5Cu As-cast Alloy

A sample was sectioned from the top, middle, and bottom of the alloy slug. All three of the measured sections had relatively the same thermal diffusivity as a function of temperature. The average thermal diffusivity vs. temperature is plotted in Figure 4-44. The thermal diffusivity was calculated by taking the average of five different measurements at each temperature. In each case, the diffusivity increased linearly from ambient to 260°C. Each of the three samples exhibited approximately the same slope and the thermal diffusivity values were nearly identical. This is indicative of the similar phase morphologies present as outlined in Section 4.1.4. The largest and smallest values came from the middle section and were 4.539 ± 0.16 mm^2/s 3.54 ± 0.08 mm^2/s, respectively.

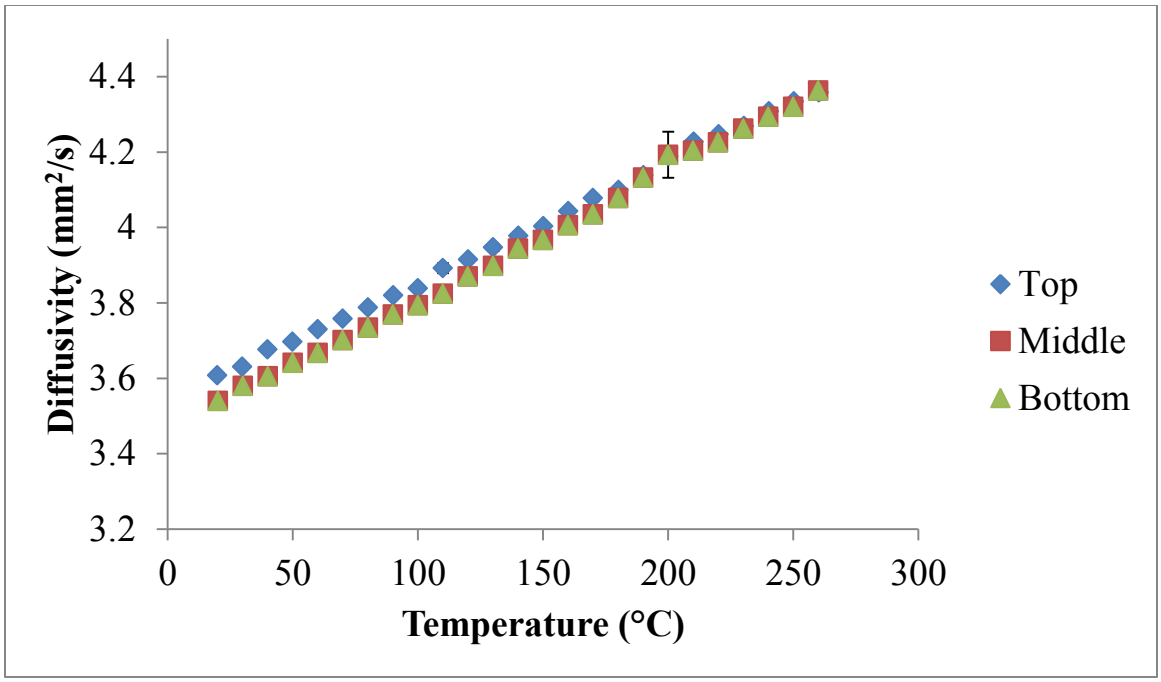

Figure 4-44: Thermal properties of as-cast Zr-12Fe-5Cu.

4.3.1.2. Zr-12Fe-10Cu As-cast Alloy

The average thermal diffusivity vs. temperature for as-cast Zr-12Fe-10Cu is plotted in Figure 4-45. Once again, the thermal diffusivity was calculated by averaging five different measurements at each temperature step. Three different samples were measured, two from the top of the ingot, denoted as top 1 and top 2, and one from the middle section. Due to the brittleness of this alloy, a bottom sample with the suitable sample dimensions, noted in Section 3.4.1, was not obtained. The top 1 section of the alloy had the lowest diffusivity measurements of the three samples, while the top 2 and middle sections shared similar diffusivity values and were generally 0.3 mm^2/s larger than top 1. Again, because the nomenclature only refers to the relative position of the section within the alloy slug, it's possible that the phase morphology between top 2 and middle were more similar than the phase morphology of top 1and top 2. In each case, the diffusivity increased linearly from ambient to 260°C. The measurement for top 1 at 220°C did not produce useful data and was

discarded. The diffusivity values for the as-cast Zr-12Fe-10Cu alloy ranged from 2.985 ± 0.013 mm^2/s at 20°C to 4.321 ± 0.019 mm^2/s at 260°C.

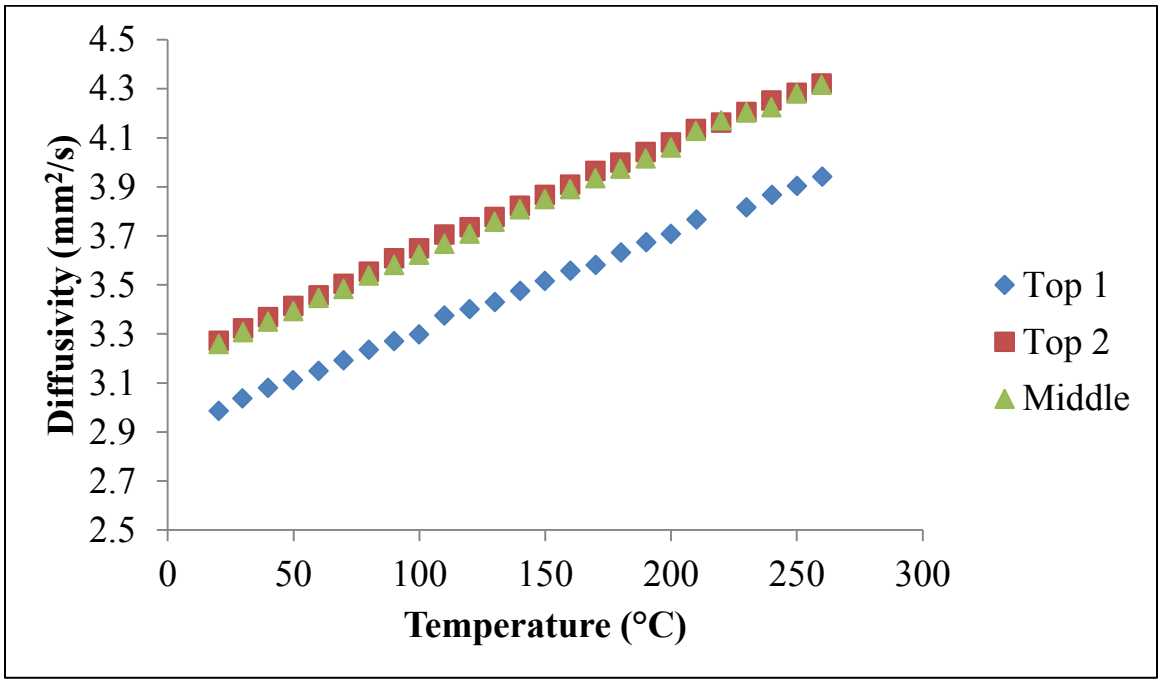

Figure 4-45: Thermal properties of as-cast Zr-12Fe-10Cu.

4.3.1.3. Zr-12Fe-15Cu As-cast Alloy

There were only two sections measured for the as-cast Zr-12Fe-15Cu, coming from the middle and bottom portions of the alloy slugs. The average of five different thermal diffusivity measurements is plotted against temperature and is depicted in Figure 4-46. Both sections had relatively the same thermal diffusivity as a function of temperature, differing by on average ~0.2 mm^2/s with the middle section being consistently lower. In each case, the diffusivity increased linearly from ambient to 260°C with roughly the same slope. The diffusivity values for the as-cast Zr-12Fe-15Cu alloy ranged from 3.416 ± 0.024 mm^2/s at 20°C to 4.759 ± 0.018 mm^2/s at 260°C.

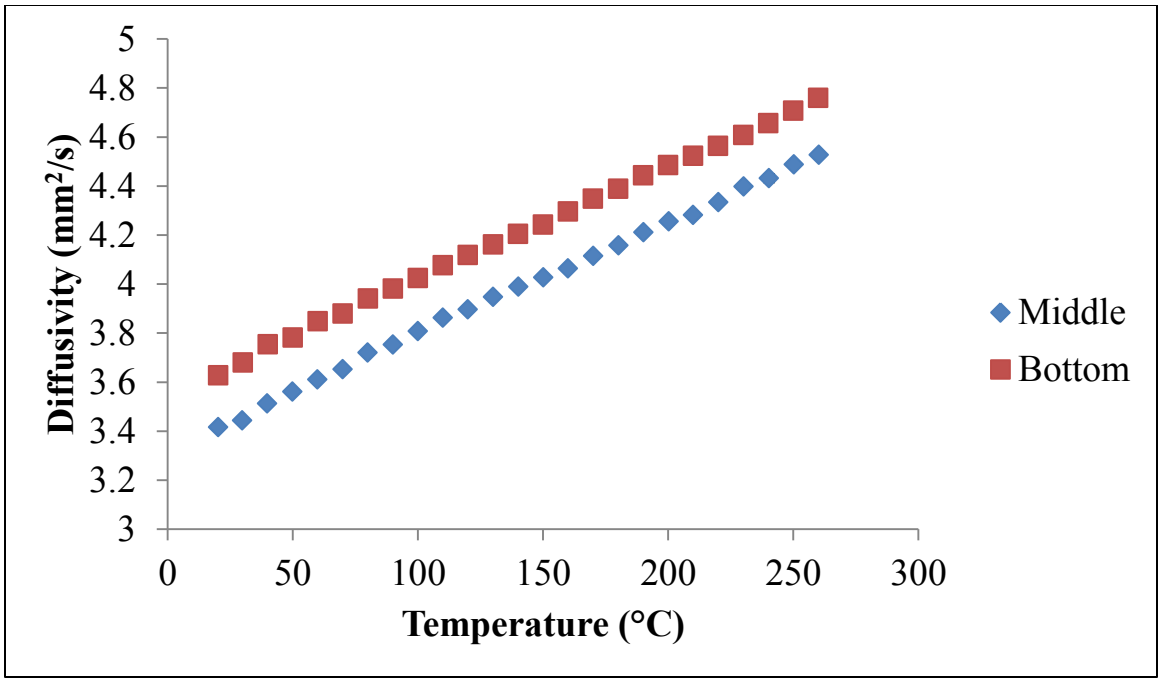

Figure 4-46: Thermal properties of as-cast Zr-12Fe-15Cu.

4.3.1.4. Summary of As-Cast Alloys LFA Measurements

In general, the LFA data from the Group C as-cast alloys provided preliminary diffusivity values. In all three alloys, the diffusivity increased linearly with temperature from ambient to 260°C. The Zr-12Fe-5Cu values were nearly identical between each of the three portions of the alloy. The values ranged from 3.54 ± 0.008 mm^2/s at 20°C to 4.539 ± 0.16 mm^2/s 260°C. The Zr-12Fe-10Cu alloy had more variation in the measured values. Two the of sections, top 2 and middle, were within error of each other, while the top 1 section of the alloy was smaller by ~0.35 mm^2/s. The diffusivity increased from 2.985 ± 0.013 mm^2/s at 20°C to 4.321 ± 0.019 mm^2/s at 260°C. The Zr-12Fe-15Cu alloy followed the same general trend of the other two alloys. The bottom portion of the alloy exhibited larger diffusivity values compared to the middle section by an average of ~2 mm^2/s. The diffusivity values for the as-cast Zr-12Fe-15Cu alloy ranged from 2.416 ± 0.013 mm^2/s at 20°C to 4.759 ± 0.019 mm^2/s at 260°C.

4.3.2. Annealed Alloys

In an effort to homogenize the LFA samples to determine the true thermal diffusivity of each of the alloys, they were heat treated. Each of the alloys was heat treated in a sealed quartz vacuum tube for 1 week at 700°C (according to the procedure described in Section 3.1.4). In order to avoid composition shifts, the heat treated samples were sectioned from the approximately the same section as their as-cast counterpart, that is the as-cast and annealed sections were cut in succession. The results of the LFA measurements are documented in the following sections.

4.3.2.1. Zr-12Fe-5Cu Annealed Alloy

Three different samples were measured for the Zr-12Fe-5Cu annealed alloy. A section was taken from the top, middle, and bottom of the ingot. All three measured sections where within 0.4 mm^2/s of each other. The average of five different thermal diffusivity measurements was plotted versus temperature and is shown in Figure 4-47. In each case, the diffusivity increased linearly from ambient to 260°C. The middle section of the alloy slug exhibited the smallest values for diffusivity ranging from 3.317 ± 0.023 mm^2/s 4.125 ± 0.016 mm^2/s, while the bottom portion of the sample had the highest values ranging from 4.539 ± 0.16 mm^2/s 4.528 ± 0.015 mm^2/s. In general, each of the three graphs had the same slope with each sample experiencing an increase of ~0.9 mm^2/s in thermal diffusivity from 20°C to 260°C. The largest and smallest values were 4.528 ± 0.008 mm^2/s and 3.317 ± 0.023 mm^2/s, respectively, a difference of 1.211 ± 0.0275 mm^2/s.

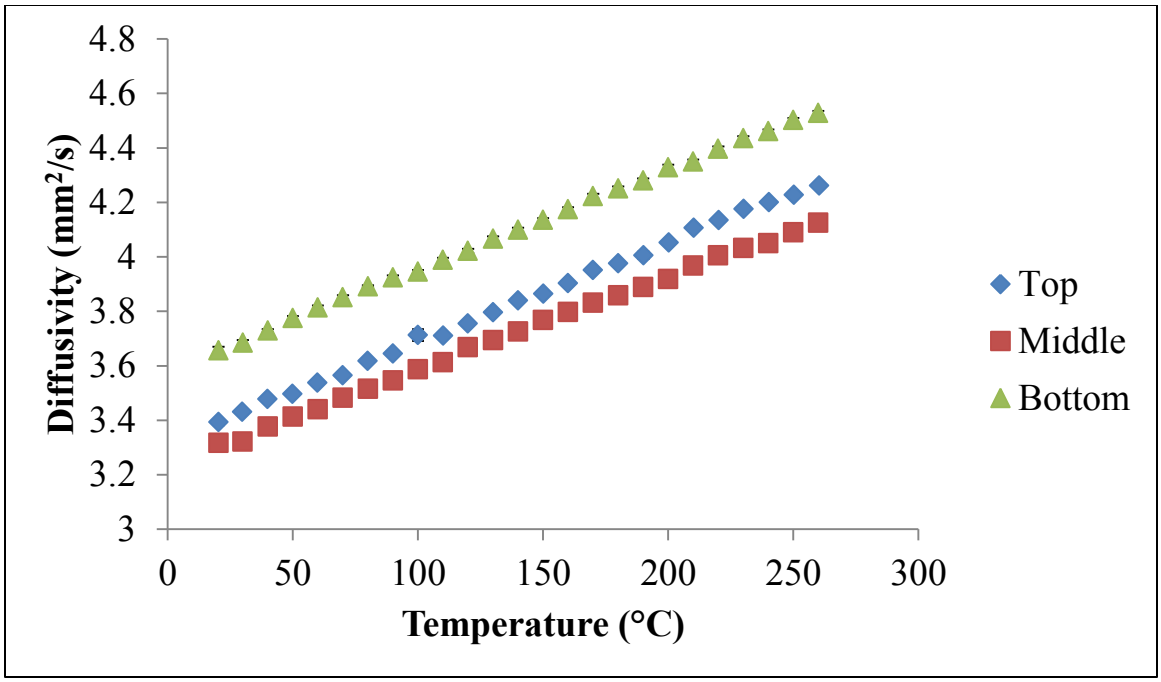

Figure 4-47: Thermal properties of annealed Zr-12Fe-5Cu.

4.3.2.2. Zr-12Fe-10Cu annealed Alloy

Three different measurements were taken, one from the top third of the slug, one from the middle third, and one from the bottom third. The average thermal diffusivity vs. temperature of each of the three samples is plotted in Figure 4-48. The values for thermal diffusivity were calculated by taking the average of 5 distinct measurements at each temperature step. In each case, the diffusivity increased linearly from 20°C to 260°C at relatively the same rate. The diffusivity values for the annealed Zr-12Fe-10Cu alloy ranged from 2.763 ± 0.017 mm^2/s at 20°C for the bottom, to 4.709 ± 0.015 mm^2/s at 260°C in the middle. The diffusivity values exhibited much greater variation compared to as-cast samples and differed by almost 1 mm^2/s in some instances.

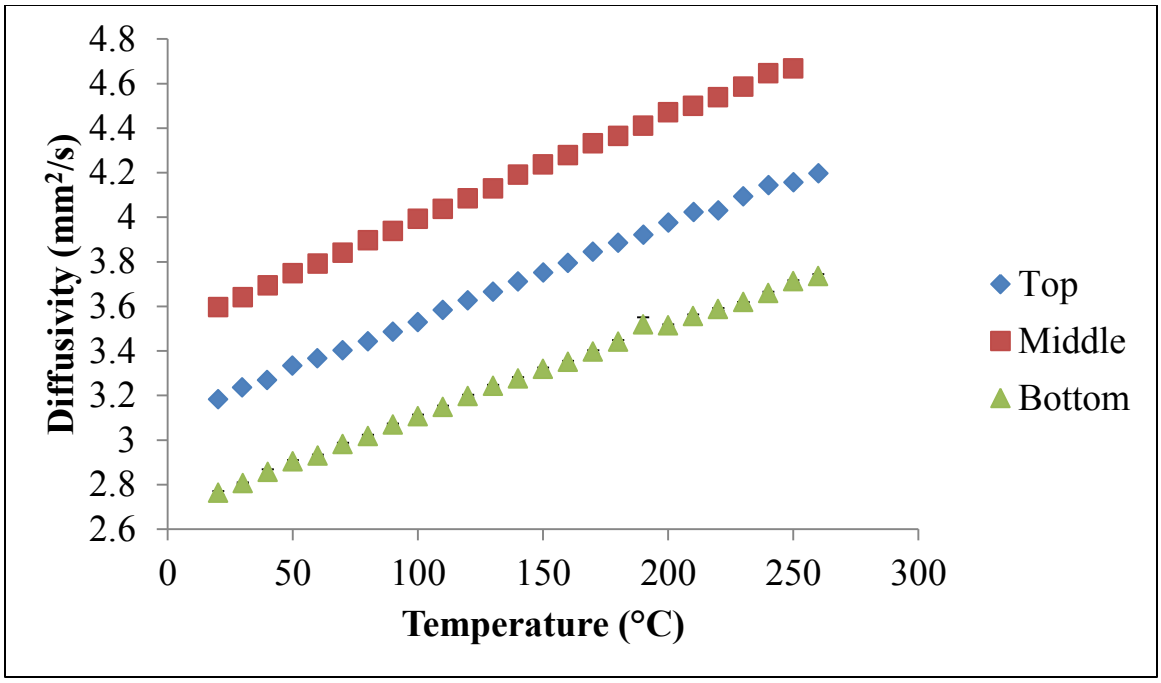

Figure 4-48: Thermal properties of annealed Zr-12Fe-10Cu.

4.3.2.3. Zr-12Fe-15Cu annealed Alloy

Three different sections of Zr-12Fe-15Cu alloy were measured each from a different section of the alloy slug. Like Zr-12Fe-5Cu and Zr-12Fe-10Cu, samples were section from the top, middle, and bottom of the ingot. The average of 5 different thermal diffusivity measurements is plotted against temperature depicted in Figure 4-49. All three sections had relatively the same thermal diffusivity as a function of temperature. The bottom section had consistently larger values for diffusivity, differing by an average ~0.4 mm^2/s with the top having the lowest values of the three sections. In each case, the diffusivity increased linearly from ambient to 260°C at the same rate increase by ~1 mm^2/s. The diffusivity values for the as-cast Zr-12Fe-15Cu alloy ranged from 3.353 ± 0.009 mm^2/s at 20°C to 4.85 ± 0.018 mm^2/s at 260°C.

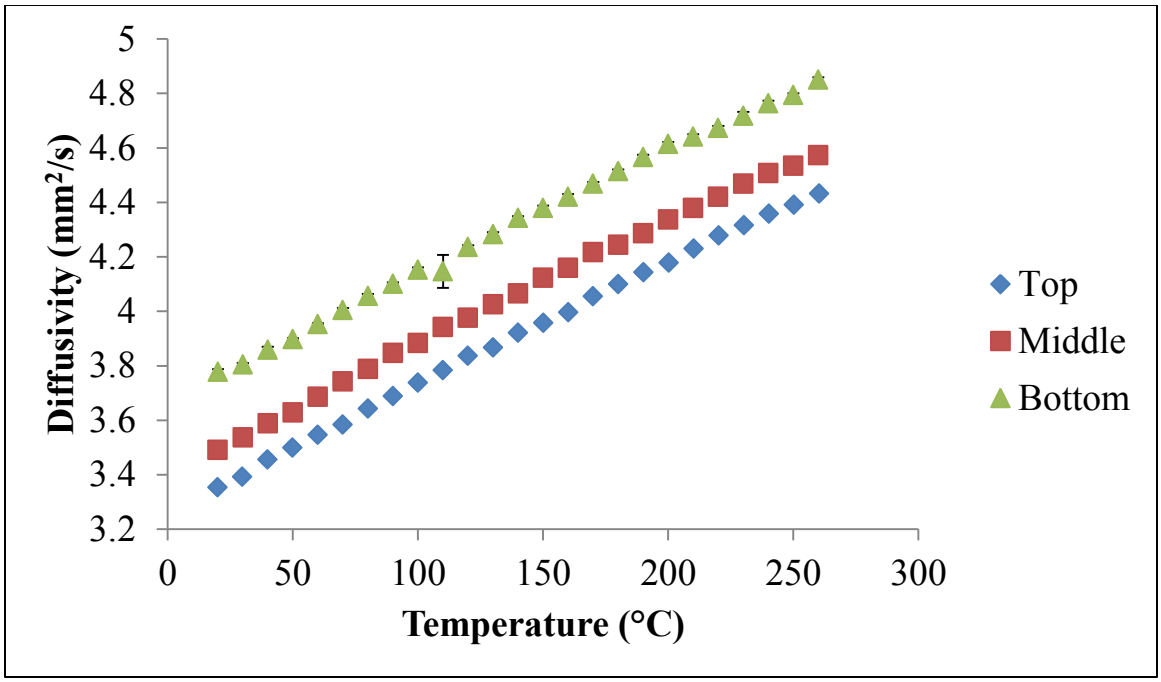

Figure 4-49: Thermal properties of as-cast Zr-12Fe-15Cu.

4.3.2.4. Summary of Annealed Alloys LFA Measurements

The LFA data from each of the Group C annealed alloys had variations in the diffusivity values between the different sections of the alloy slug. In all three alloys, the thermal diffusivity increased linearly with temperature from 20°C to 260°C. Values varied the least in Zr-12Fe-5Cu and had ranged from 3.317 ± 0.023 mm^2/s at 20°C to 4.528 ± 0.015 mm^2/s 260°C. The Zr-12Fe-10Cu alloy varied the most, which was also the case in the as-cast alloys, with diffusivity values differing by as much as ~1 mm^2/s. The diffusivity increased from 2.763 ± 0.013 mm^2/s at 20°C in the bottom section to 4.709 ± 0.015 mm^2/s at 260°C in the middle section, a difference of 1.939 ± 0.908 mm^2/s. The 15wt% Cu alloy followed the same general trend of the other two alloys. The bottom portion of the alloy exhibited larger diffusivity values compared to the middle section by an average of ~4 mm^2/s, double what was seen in the as-cast alloys. The diffusivity values for the as-cast Zr-12Fe-15Cu alloy ranged from 3.353 ± 0.009 mm^2/s at 20°C to 4.85 ± 0.018 mm^2/s at 260°C, a difference of 1.497 ± 0.0201 mm^2/s.

5. DISCUSSION

5.1. Phase Morphology Characteristics of Zr-Fe-Cu Alloys

The Zr-Fe-Cu alloys observed each exhibited relatively complex phase morphologies but they were somewhat consistent with the predicted phases noted in Section 3. The cast alloys showed the expected combination of phases with the exception of the $ZrFe_2$ Laves phase which was expected for the Zr-12Fe-15Cu alloy but was not observed. The following sections discuss the observations found during EPMA analysis.

5.1.1. Group A

Although only one of the cast Group A alloys was homogenous a lot was learned from the phase morphologies and the purpose of the casting exercise was fulfilled. Because of the results documented in Section 4.1.1, it was determined that a single melting stage was insufficient for complete homogenization, with the possible exception of the Zr-12Fe-5Cu alloy. The experience gained from the fabrication and examination of these alloys was used to modify the procedures to generate the more homogenous alloys examined in Section 4.1.2 through 4.1.5 as well as in the DSC and LFA measurements.

Table 5-1 gives a summary of the WDS data measured from these alloys. Limited analysis was done with the Group A alloys because only the alloy containing 5wt% Cu was cast uniformly and showed the same phase morphology across the alloy slug. As seen in Table 5-1 the solubility of Fe and Cu was much larger and varied than what was seen in the phase diagram. [22] [27] The observed solubility of Fe and Cu was 3.14 ± 1.99 and 2.19 ± 1.99, respectively. The high temperature Zr_2Fe that was shown to only be stable above 775°C [22] seemed to have formed a stable compound at room temperature which was consistent with what was seen in literature for similar alloys. [31] In instances where Zr_2Fe was seen to be stable at room temperature it formed as precipitates within a bulk $ZrFe_2$ Laves phase, however in Zr-12Fe-5Cu it formed the bulk matrix. [32]. The other two alloys did not cast uniformly and showed to be Zr rich in the top half. Because of this, the axial and radial sections showed two different phase morphologies in which the top half had Zr precipitates

within a matrix of intermetallic compounds while the bottom half was exclusively intermetallic compounds.

Table 5-1: Summary of Group A EPMA data.

SAMPLE	APPARENT PHASE	SPOTS AVERAGED	FE (AT%)	CU (AT%)	ZR (AT%)
Zr-12Fe-5Cu					
Axial AC*	Zr Solution	1	0.32**	0.24	99.45
Radial AC	Zr Solution	7	3.14 ± 1.99	2.19 ± 0.51	94.67 ± 2.48
Axial AC	Zr_3(Fe,Cu)	2	20.55 ± 0.03	4.23 ± 0.26	75.22± 0.23
Radial AC	Zr_3(Fe,Cu)	2	20.73 ± 0.13	3.69 ± 0.03	75.58 ± 0.16
Axial AC	Zr_2(Fe,Cu)	2	25.84 ± 0.16	7.20 ± 0.06	66.96 ± 0.09
Radial AC	Zr_2(Fe,Cu)	2	23.59 ± 0.87	9.18 ± 0.89	67.24± 0.01
Zr-12Fe-8Cu					
Axial AC	Zr_3(Fe,Cu)	3	2.01 ± 1.94	1.89 ± 1.00	96.10 2.84
Axial AC	Zr_3(Fe,Cu)	2	18.87 ± 0.44	5.98 ± 0.38	75.15 ± 0.06
Axial AC	Zr_2(Fe,Cu)	1	22.67	10.47	66.86
Radial AC	Zr_3(Fe,Cu)	2	15.01 ± 3.01	13.37 ± 1.28	71.62 ± 1.73
Radial AC	Zr_2(Fe,Cu)	2	23.07 ± 0.07	10.14 ± 0.19	66.79 ± 0.12
Radial AC	Zr_2(Fe,Cu)	3	22.28 ± 1.09	9.89 ± 1.19	67.84 ± 0.45
Zr-12Fe-15Cu					
Axial AC	Zr_2(Fe,Cu)	2	20.42 ± 0.09	12.60± 0.11	66.99 ± 0.02
Axial AC	Zr_2(Fe,Cu)	2	4.42 ± 0.31	28.61 ± 0.35	66.97 ± 0.04
Radial AC	Zr_2(Fe,Cu)	2	20.16 ± 0.11	13.02 ± 0.03	66.82 ± 0.15
Radial AC	Zr(Fe,Cu)	2	19.48 ± 0.02	30.01 ± 0.01	50.51 ± 0.02

*AC = As-Cast; ** Data provided without the ± spread values represent single data points

5.1.2. Groups B and C

5.1.2.1. Variations in the Fe and Cu Elemental Compositions

Both Groups B and C experienced variations in the observed phases, namely the bulk intermetallic phases. Table 5-2 and Table 5-3 summarize the average compositional make up of each of the observed phases in Group B and Group C respectively. The changes made to the casting procedure proved important to insure even mixing of the alloys during casting.

The Zr-12Fe-10Cu alloy still did not mix evenly. There was an uneven distribution of Zr, the top half of the sample remained Zr rich even after inverting the sample for the second casting. It is not evident from the materials generated in this study whether or not a homogenous sample can be produced for the Zr-12Fe-10Cu alloy using the tall melt crucibles from this study; the vertical segregation of the zirconium seemed to be unrelated to gravity or casting mechanics which implies a probably solidification-based segregation. As another point of interest, the Zr solution phase showed elevated amounts of Fe and Cu as compared to the solubility of these compounds discussed in the previous section. The solubility did decrease with annealing, however was still larger by a factor of ~4. Each of the alloys sets exhibited the predicted phases based on the phase field shown in Figure 3-2 with exception of the Laves phase.

The Zr-12Fe-5Cu proved to be the most stable of the three alloys having the same three phases present in each of the casting groups, including Group A. According to the Fe-Zr phase diagram (Figure 2-4) a Fe-83Zr alloy would contain only the Zr_3Fe intermetallic. In the Zr-12Fe-5Cu alloy, the addition of copper as an alloying element lead to the formation of three separate phases noted in Table 5-2, similar to what was seen in the alloys studied by Abraham et. al. [31] [32] There were relatively large variations in the elemental composition of Fe and Cu while the relative composition of Zr remained statistically the same in the bulk intermediate phase. The variation in the bulk phase points to non-equilibrium phases most likely the result of uneven cooling during casting. Annealing of the samples produced more homogenous samples. After heat treatment, the bulk intermetallic phase showed little variation in the Fe and Cu compositions. The Group C annealing was not as homogenous as the one done for Group B due to the larger samples needed for LFA analysis. While there was still variation in the intermetallic phase it was less apparent than in the as-cast samples.

As was noted in Section 4.1, Zr-12Fe-10Cu had varying phase morphologies between the axial and radial sections. Additionally, there were distinct variations in the elemental composition of the observed phases. The composition of Zr within each individual phase stayed relatively consistent in both alloying groups, as we the case with the other alloys. There were however large statistical variations in the Fe and Cu concentrations in most of the intermetallic phases. This was especially apparent in the Group B axial section where there was a partial decomposition of the $Zr_3(Fe,Cu)$ phase giving the appearance of two bulk

matrix phases. After annealing it was clear that the Zr_3(Fe,Cu) broke down into multiple phases as seen in Figure 5-1. The dark web-like structure (Fig. 5-1) that appears in the annealed Group B samples was Cu rich and had the same apparent intermetallic structure, $Zr_{2(}$Fe,Cu), as the bulk intermetallic phase. The same Cu rich phase also appeared in the Group C annealed samples (Fig. 5-2) but didn't appear as a dark web but rather was integrated into the light gray intermetallic structures. The apparent difference in contrast between the two samples was most likely the result of partial decomposition of the $Zr_{3(}$Fe,Cu) intermetallic as was noted in Figure 5-1. Figure 5-2 shows a structure similar to what was seen in the as-cast Group B alloy. Due to the larger sample during annealing, the phase wasn't able to decompose completely leaving small Cu rich zones instead of the web seen in the annealed Group B Zr-12Fe-10Cu alloy.

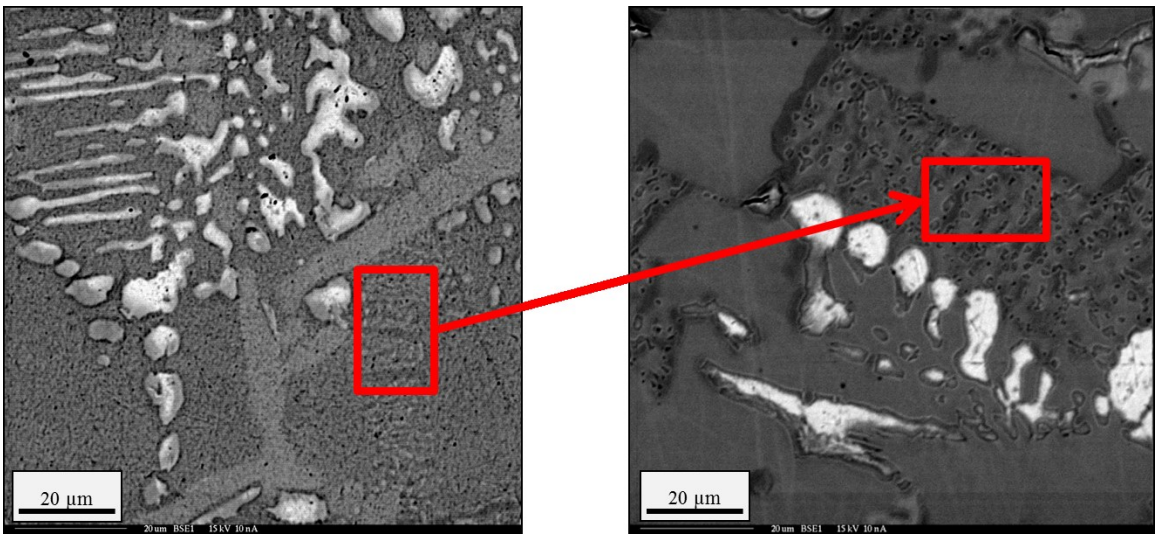

Figure 5-1: Decomposition of the Zr_3Fe intermetallic: As-cast (left) and Annealed (right).

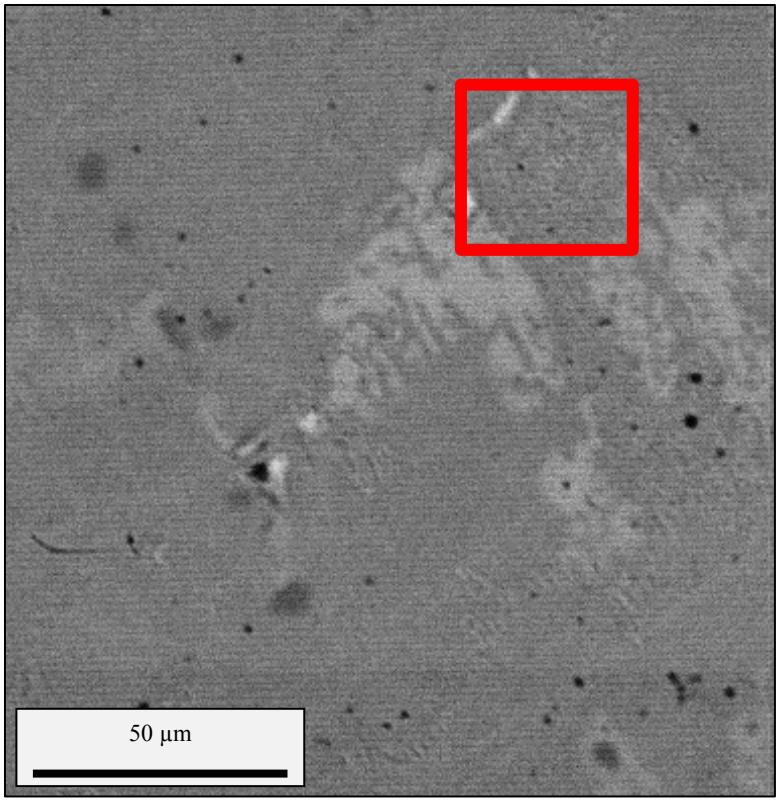

Figure 5-2: Partial decomposition of the Zr_3Fe intermetallic in annealed Group C Zr-12Fe-10Cu alloy.

There was little variation in the Fe and Cu elemental compositions in all of the observed phases in both groups with the exception of one phase in Zr-12Fe-15Cu. As with the other two alloys, the bulk intermetallic phase displayed relatively large variations in the Fe and Cu concentration. The largest disparity appeared in the axial section of the as-cast Group B alloy in which the standard deviation between measurements was 3.21, 1.58, and 1.64, for Fe, Cu, and Zr, respectively. The variation, along with the fact that only three phases appeared in the radial section compared to four that appeared in the axial section, was indicative of uneven cooling in the as-cast sample leading to the formation of non-equilibrium phases. It is of note that there may actually have been four phase present but only three were characterizable (Section 4.1.2.3). Annealing the samples eliminated the deviations seen in the as-cast samples. The Group C samples didn't experience the same variation in the matrix intermetallic phases, however, there did appear to be incomplete formation of the Zr_3(Fe,Cu) intermetallic even with annealing. Even though both groups had the same phases

present, the phase morphologies were distinctly different between the two groups. From Figure 5-3 it's easy to see that the in the Group B alloy, the Cu rich intermetallic forms a web throughout the bulk intermetallic phase as opposed to the Group C sample where it forms exclusively around the island structures.

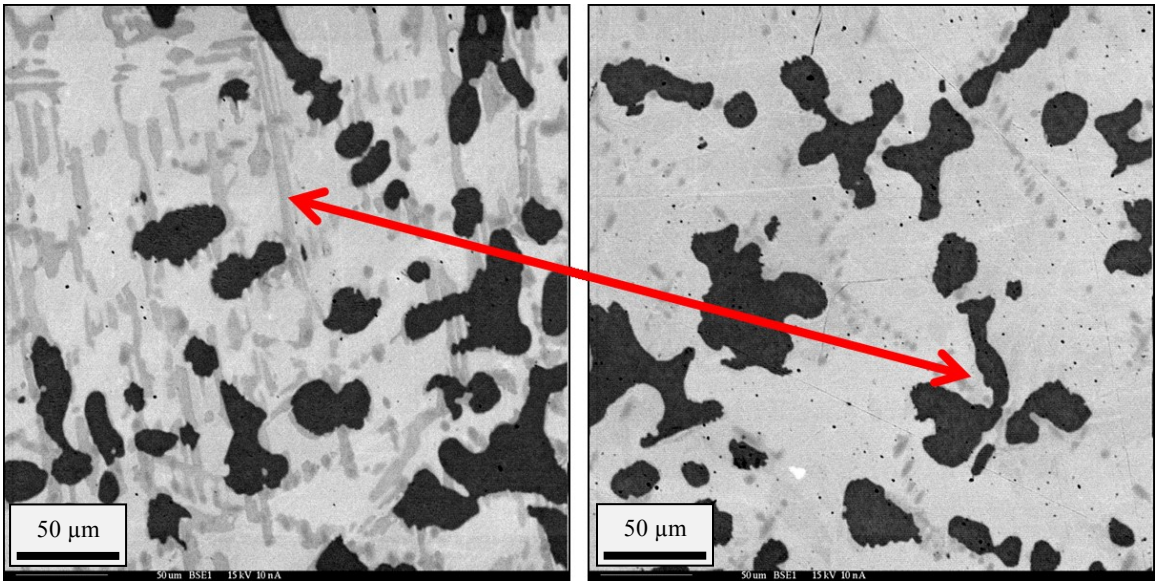

Figure 5-3: Annealed Zr-12Fe-15Cu alloy highlighting the partial formation of the Cu rich intermetallic phase: Group B (left) & Group C (right).

Table 5-2: Summary of Group B EPMA Data.

ANALYSIS	APPARENT PHASE	SPOTS AVERAGED	FE (AT%)	CU (AT%)	ZR (AT%)
Zr-12Fe-5Cu					
Axial AC*	Zr Solution	1	3.00**	2.28	94.72
Radial AC	Zr Solution	1	1.21	2.41	96.39
Annealed	Zr Solution	2	0.61 ± 0.01	0.53 ± 0.01	98.86 ± 0.00
Axial AC	Zr_3(Fe,Cu)	2	20.80 ± 0.07	3.64 ± 0.00	75.56 ± 0.07
Radial AC	Zr_3(Fe,Cu)	2	20.22 ± 0.16	4.34 ± 0.20	75.44 ± 0.04
Annealed	Zr_3(Fe,Cu)	2	20.18 ± 0.24	4.30 ± 0.29	75.52 ± 0.05
Axial AC	Zr_2(Fe,Cu)	2	23.16 ± 1.15	9.26 ± 1.20	67.58 ± 0.01
Radial AC	Zr_2(Fe,Cu)	3	22.30 ± 1.62	10.43 ± 1.66	67.28 ± 0.13
Annealed	Zr_2(Fe,Cu)	2	22.04 ± 0.09	10.75 ± 0.17	67.22 ± 0.09
Zr-12Fe-10Cu					
Axial AC	Zr Solution	1	0.59	0.95	98.46
Annealed	Zr Solution	2	0.38 ± 0.20	1.13 ± 0.48	98.48 ± 0.68
Axial AC	Zr_3(Fe,Cu)	1	18.04	7.03	74.92
Annealed	Zr_3(Fe,Cu)	2	19.39 ± 0.10	5.11 ± 0.10	75.50 ± 0.20
Axial AC	Zr_2(Fe,Cu)	3	18.97 ± 3.21	12.88 ± 1.58	68.14 ± 1.64
Radial AC	Zr_2(Fe,Cu)	2	20.17 ± 0.69	12.86 ± 0.48	66.97 ± 0.21
Annealed	Zr_2(Fe,Cu)	2	21.01 ± 0.03	11.50 ± 0.03	67.49 ± 0.04
Axial AC	Zr_2(Fe,Cu)	2	12.44 ± 0.69	15.92 ± 0.57	71.64 ± 0.12
Radial AC	Zr_2(Fe,Cu)	2	4.54 ± 0.08	28.66 ± 0.34	66.80 ± 0.27
Annealed	Zr_2(Fe,Cu)	1	21.12	10.64	68.24
Annealed	Zr_2(Fe,Cu)	2	3.83 ± 0.76	27.63 ± 0.45	68.53 ± 1.22
Radial AC	Zr(Fe,Cu)	1	20.55	28.78	50.67
Zr-12Fe-15Cu					
Axial AC	Zr_2(Fe,Cu)	2	19.23 ± 0.09	13.96 ± 0.13	66.81 ± 0.05
Annealed	Zr_2(Fe,Cu)	3	3.88 ± 0.04	29.11 ± 0.20	67.01 ± 0.24
Axial AC	Zr_2(Fe,Cu)	2	16.14 ± 3.05	16.94 ± 2.86	66.92 ± 0.19
Radial AC	Zr_2(Fe,Cu)	2	19.92 ± 0.89	13.12 ± 0.64	66.97 ± 0.25
Annealed	Zr_2(Fe,Cu)	3	21.04 ± 0.53	11.94 ± 0.44	67.02 ± 0.15
Axial AC	Zr_2(Fe,Cu)	2	19.00 ± 0.04	13.22 ± 0.02	67.78 ± 0.06
Radial AC	Zr_2(Fe,Cu)	2	21.02 ± 0.11	11.72 ± 0.05	67.26 ± 0.05
Annealed	Zr_2(Fe,Cu)	3	20.84 ± 0.53	11.77 ± 0.74	67.39 ± 0.24
Axial AC	Zr(Fe,Cu)	2	18.63 ± 0.07	30.43 ± 0.06	50.95 ± 0.13
Radial AC	Zr(Fe,Cu)	2	20.15 ± 0.05	29.29 ± 0.02	50.56 ± 0.07
Annealed	Zr(Fe,Cu)	2	19.65 ± 0.14	29.33 ± 0.12	51.02 ± 0.01

*AC = As-Cast; ** Data provided without the ± spread values represent single data points

Table 5-3: Summary of Group C EPMA Data.

ANALYSIS	APPARENT STRUCTURE	SPOTS AVERAGED	FE (AT%)	CU (AT%)	ZR (AT%)
Zr-12Fe-5Cu					
Axial AC*	Zr Solution	2	1.95 ± 1.84	1.84 ± 0.36	96.21 ± 2.19
Radial AC	Zr Solution	2	3.42 ± 0.59	2.32 ± 0.21	94.25 ± 0.80
Annealed	Zr Solution	2	0.35 ± 0.07	0.34 ± 0.17	99.31 ± 0.24
Axial AC	Zr_3(Fe,Cu)	2	21.21 ± 0.17	3.62 ± 0.02	75.17 ± 0.16
Radial AC	Zr_3(Fe,Cu)	2	20.72 ± 0.05	3.94 ± 0.15	75.34 ± 0.19
Annealed	Zr_3(Fe,Cu)	2	20.41 ± 0.48	4.06 ± 0.32	75.53 ± 0.16
Axial AC	Zr_2(Fe,Cu)	3	23.86 ± 2.38	6.86 ± 0.59	69.27 ± 2.96
Radial AC	Zr_2(Fe,Cu)	3	24.46 ± 0.86	8.24 ± 0.79	67.30 ± 0.13
Annealed	Zr_2(Fe,Cu)	4	22.29 ± 2.15	10.09 ± 2.35	67.62 ± 0.26
Zr-12Fe-10Cu					
Axial AC	Zr Solution	2	1.61 ± 1.46	1.44 ± 0.70	96.96 ± 2.16
Annealed	Zr Solution	2	0.63 ± 0.35	1.57 ± 0.65	97.80 ± 1.00
Annealed	Zr_3(Fe,Cu)	3	19.46 ± 0.04	5.03 ± 0.07	75.51 ± 0.16
Axial AC	Zr_2(Fe,Cu)	3	20.83 ± 1.57	12.36 ± 1.52	66.82 ± 0.06
Radial AC	Zr_2(Fe,Cu)	3	21.07 ± 0.62	11.62 ± 0.64	67.31 ± 0.07
Annealed	Zr_2(Fe,Cu)	3	21.05 ± 0.46	11.49 ± 0.40	67.46 ± 0.10
Annealed	Zr_2(Fe,Cu)	1	6.89**	23.78	69.34
Axial AC	Zr_2(Fe,Cu)	2	13.18 ± 0.52	15.74 ± 0.32	71.08 ± 0.20
Radial AC	Zr_2(Fe,Cu)	2	4.62 ± 0.17	27.99 ± 0.42	67.39 ± 0.25
Axial AC	Zr_2(Fe,Cu)	2	21.65 ± 0.08	10.42 ± 0.21	67.92 ± 0.13
Radial AC	Zr_2(Fe,Cu)	2	21.82 ± 0.16	10.20 ± 0.02	67.97 ± 0.14
Annealed	Zr_2(Fe,Cu)	2	21.90 ± 0.68	9.67 ± 0.36	68.43 ± 0.32
Zr-12Fe-15Cu					
Axial AC	Zr_2(Fe,Cu)	2	4.35 ± 0.10	28.78 ± 0.04	66.87 ± 0.05
Radial AC	Zr_2(Fe,Cu)	2	4.34 ± 0.11	28.76 ± 0.15	66.90 ± 0.04
Annealed	Zr_2(Fe,Cu)	4	3.88 ± 0.35	29.42 ± 0.07	66.70 ± 0.35
Axial AC	Zr_2(Fe,Cu)	2	20.58 ± 0.55	12.49 ± 0.61	66.93 ± 0.06
Radial AC	Zr_2(Fe,Cu)	2	19.30 ± 0.13	13.60 ± 0.13	67.10 ± 0.00
Annealed	Zr_2(Fe,Cu)	4	20.93 ± 0.99	11.93 ± 1.10	67.14 ± 0.23
Axial AC	Zr_2(Fe,Cu)	3	20.53 ± 0.13	11.84 ± 0.06	67.64 ± 0.09
Radial AC	Zr_2(Fe,Cu)	2	19.62 ± 0.09	12.76 ± 0.12	67.62 ± 0.03
Annealed	Zr_2(Fe,Cu)	2	20.48 ± 0.17	11.73 ± 0.25	67.79 ± 0.07
Axial AC	Zr(Fe,Cu)	2	20.46 ± 0.03	28.89 ± 0.05	50.65 ± 0.08

*AC = As-Cast; ** Data provided without the ± spread values represent single data points

Table 5-3: Continued.

ANALYSIS	APPARENT STRUCTURE	SPOTS AVERAGED	FE (AT%)	CU (AT%)	ZR (AT%)
Radial AC	Zr(Fe,Cu)	2	19.11 ± 0.12	30.09 ± 0.04	50.81 ± 0.08
Annealed	Zr(Fe,Cu)	2	19.79 ± 0.14	29.10 ± 0.39	51.11 ± 0.24

*AC = As-Cast; ** Data provided without the ± spread values represent single data points

5.1.2.2. Zr_2M Intermetallic Phase[12]

Early studies have shown that the Zr_2Fe intermetallic is only stable at high temperatures forming at temperatures between 974°C and 775°C. At temperatures below 775°C it was thought to decompose in the $ZrFe_2$ Laves phase and Zr_3Fe intermetallic by a eutectoid reaction. [33] The Laves phase are intermetallic phases that exhibit an AB_2 composition and have one of three different crystal structures: C14 (hexagonal, $MgZn_2$-type), C15 (cubic, Cu_2Mg-type), and C36 (dihexagonal, $MgNi_2$-type). [34] Recent studies have shown that Zr_2Fe will form stable compounds even at low temperatures [35] and was seen to be present in similar alloys [31]. Recent thermodynamic calculations of Zr-Fe and Zr-Fe-C alloys have adopted the existence of a stable low temperature Zr_2Fe phase while rejecting the decomposition at temperatures below 775°C. [36] In the work done by D. Abraham et. al. with similar Zr alloys, the Zr_2Fe intermetallic formed as $Zr_2(Fe,Ni)$ and appeared as precipitates within the bulk matrix phase composed of the $Zr(Fe,Cr,Ni)_{2+x}$ Laves phase. The same precipitates were observed in both the Zr-12Fe-10Cu and Zr-12Fe-15Cu alloys.

These types of precipitates formed with the an apparent Zr_2M structure, one which was Cu rich with approximately a 7:1 ratio of Cu to Fe and the second was a Fe rich phase with an approximate 2:1 ratio of Fe to Cu. The Cu rich precipitates are shown in Fig. 5-4 and Fig. 5-5Figure 5-7 while the Fe rich precipitates are shown in Figure 5-6 and Figure 5-7. The WDS data for the Cu rich phases is consistent with the formation of the Zr_2Cu intermetallic with some Fe on the Cu lattice sites. In contrast, the Fe rich phase is consistent with a Zr_2Fe intermetallic with some Cu on the Fe lattice sites. The similar contrast distinction of the

[12] *Where M is a combination of Fe and Cu*

phases in the BSE images was indicative of their relatively close atomic weight as well as the similar crystal structures for Zr_2Cu and Zr_2Fe.

In addition to the formation of both Cu and Fe rich $Zr_2(Fe,Cu)$ intermetallics there was also a third phase whose elemental composition would point to a $Zr_2(Fe,Cu)$ intermetallic phase. This third intermetallic phase formed the bulk matrix phase in all of the alloys from all three groups. This is not consistent to what was seen by D. Abraham et. al, in which the bulk matrix phase was composed of the $ZrFe_2$ Laves in Zr rich alloys. [31] [32] The $ZrFe_2$ Laves phase was not observed in any of the alloys. The bulk intermetallic phase had statistically the same elemental composition for all three elements as the Fe rich precipitate phase. At first it was thought that possibly the Zr_2Fe was also a Laves phase and that the three observed phases were a result of the allotropic differences of the three crystal structures that make up the Laves phases. [34] However, the two precipitate phases both have tetragonal type structures (Zr_2Fe is BCT), which is not one of the three Laves phases, therefore the three distinct phases could not be the result of the Laves allotropes. Additionally, the precipitates were too large to assume that the electron beam was penetrating all the way through the phase into the bulk matrix phase showing they were the same. Finally, it was also unlikely that the Fe rich precipitates were the decomposition of another phase, as observed in Figure 5-1, which would also give the same results. Since only EPMA analysis was done, the actual phases present and their effective crystal structure were not known. Because of this, it is unknown at this time why there exists two distinct phase morphologies with statistically the same elemental make up. Further analysis will need to be done in order to determine why these two phases form such different morphologies.

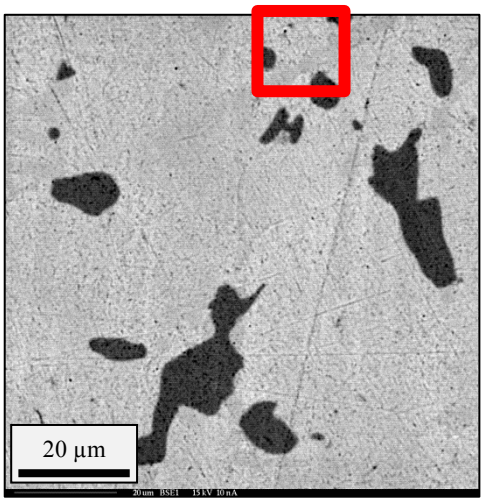

(a) Radial as-cast Zr-12Fe-10Cu

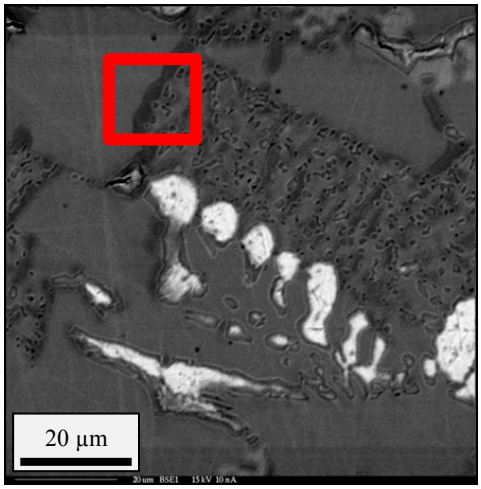

(b) Annealed as-cast Zr-12Fe-10Cu

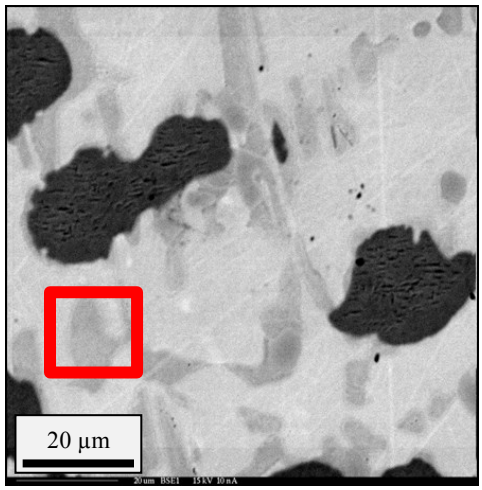

(d) Annealed Zr-12Fe-15Cu

Figure 5-4: Copper rich Zr_2(Fe,Cu) precipitates in Group B alloys.

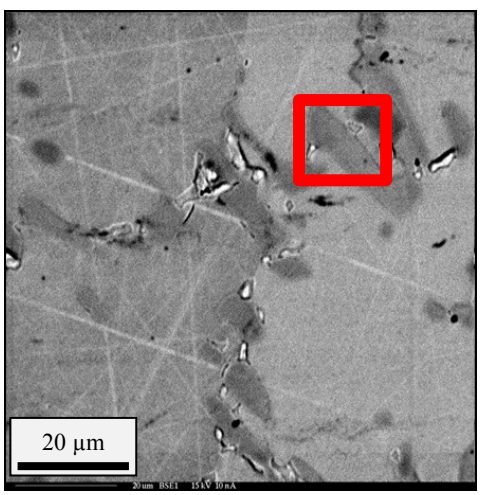

(a) Radial as-cast Zr-12Fe-10Cu

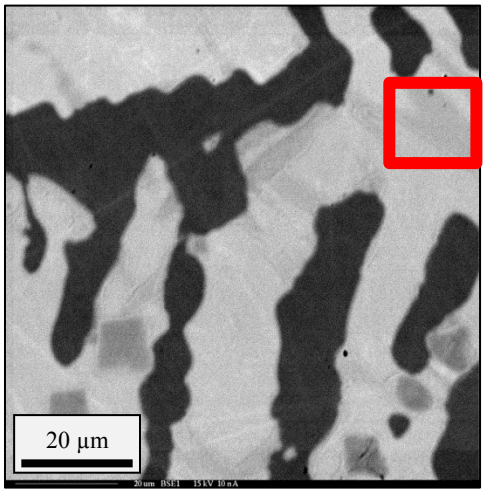

(b) Axial as-cast Zr-12Fe-15Cu

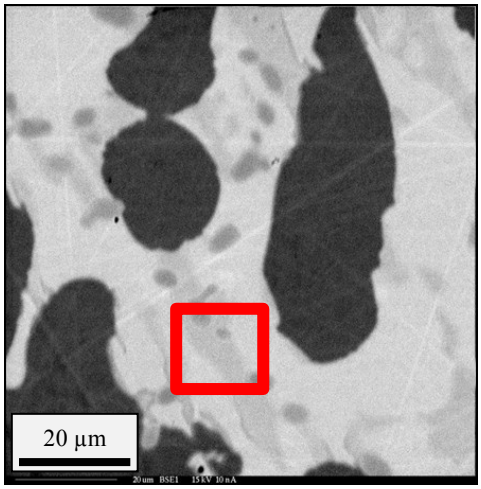

(c) Radial as-cast Zr-12Fe-10Cu

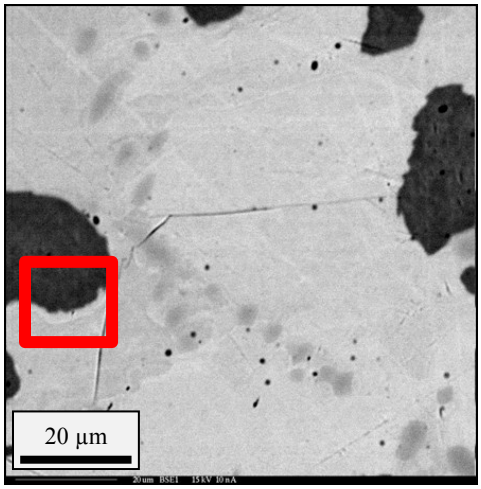

(d) Annealed Zr-12Fe-15Cu

Figure 5-5: Copper rich Zr_2(Fe,Cu) precipitates in Group C alloys.

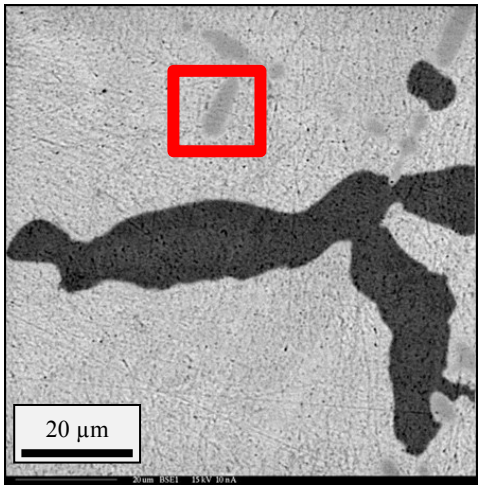

(b) Axial as-cast Zr-12Fe-15Cu

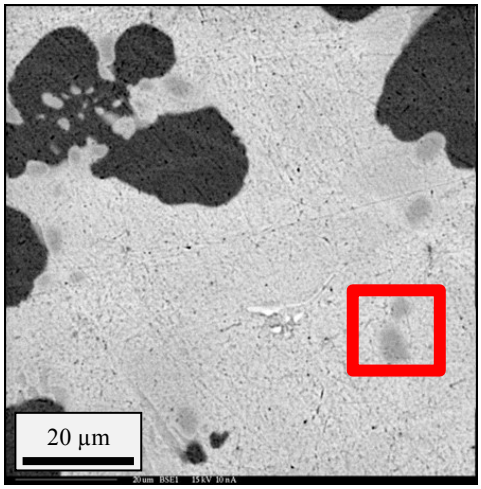

(b) Radial as-cast Zr-12Fe-15Cu

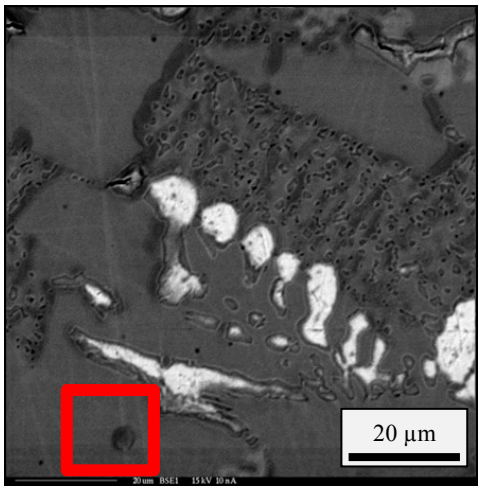

(c) Annealed Zr-12Fe-10Cu

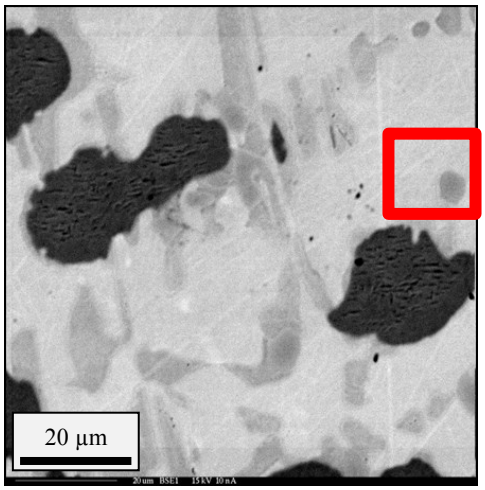

(d) Annealed Zr-12Fe-15Cu

Figure 5-6: Iron rich Zr_2(Fe,Cu) precipitates in Group B alloys.

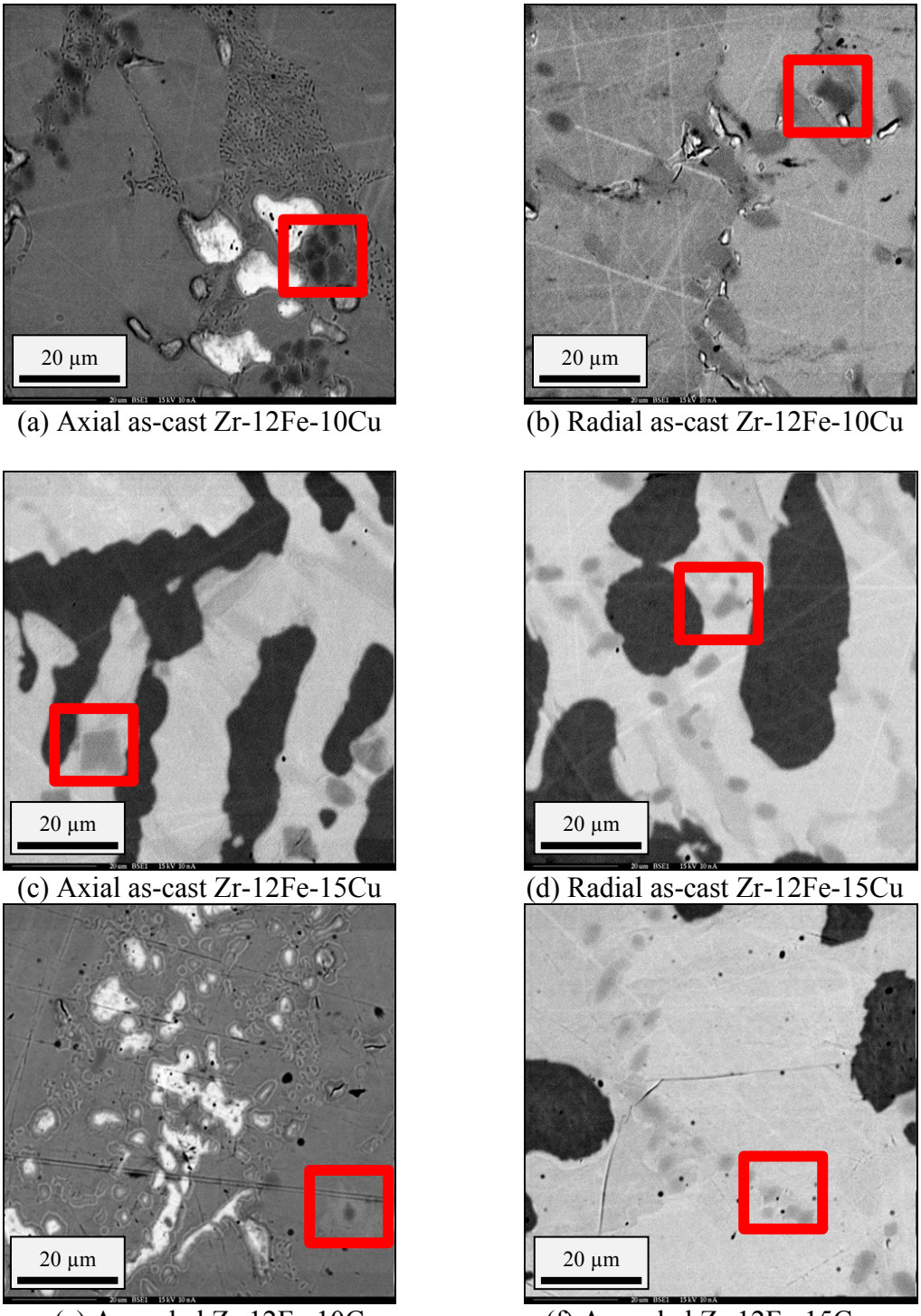

(a) Axial as-cast Zr-12Fe-10Cu (b) Radial as-cast Zr-12Fe-10Cu

(c) Axial as-cast Zr-12Fe-15Cu (d) Radial as-cast Zr-12Fe-15Cu

(e) Annealed Zr-12Fe-10Cu (f) Annealed Zr-12Fe-15Cu

Figure 5-7: Iron rich Zr_2(Fe,Cu) precipitates in Group C alloys.

5.2. Phase Transition Features of Zr-Fe-Cu Alloys

Since no published ternary phase diagram exists for the Zr-Fe-Cu alloy system, this study acted to provide an experimental basis for initial phase transformation calculations to complement the already ongoing CALPHAD simulations being done at LLNL. A discussion of the results presented in Section 4.2 is given below.

5.2.1. As-Cast Zr-Fe-Cu Alloys

Each of the three alloys experienced three distinct phase transitions. The set of DSC heating curves for all three alloys is depicted in Figure 5-8. The Zr-12Fe-5Cu and Zr-12Fe-10Cu both experienced a broad phase transition at 782.1°C and 787.9°C, a difference of 5.8°C. The actual difference may be larger or smaller based on the method for calculating the onset temperature discussed in Section 4.3. Both transitions were broad and shallow, however the depression in the DSC curve was much more subtle in the Zr-12Fe-10Cu alloy than in the Zr-12Fe-5Cu. The broad transition may be the result of a transition occurring on a non-isotherm phase boundary. In accordance with the lever rule, crossing over this phase boundary with increasing temperature will result in a continuous phase transformation.

The 5wt% alloy then exhibited a transition at 870.8°C which isn't apparent in Figure 5-8, however, can clearly be seen in Figure 4-38. It is of note the proximity of this transition to the alpha to beta zirconium transition which occurs at 865°C. This transition was very similar to the transition observed in the Zr-12Fe-15Cu alloy which occurred at 872.4°C. Both transitions occurred approximately 10°C before melting and were very small in comparison to the melt transition; the transition which occurred in Zr-12Fe-15Cu was much more distinct and can clearly be seen in Figure 5-8. All three alloys had obvious melt transitions occurring at: 883.0°C for Zr-12Fe-5Cu, 870.0°C for Zr-12Fe-10Cu, and 884.0°C for Zr-12Fe-15Cu. It's interesting to note that there was a 10°C difference between Zr-12Fe-5Cu and Zr-12Fe-10 which showed relatively the same phase morphology with the exception of the Zr solution phase which was greater in Zr-12Fe-5Cu. The increase in temperature was most likely the result of the increase in the primary Zr phase. The similarity in melting temperatures between Zr-12Fe-5Cu at 883.0°C and Zr-12Fe-15Cu at 884.0°C is also of note

given their stark difference in phase morphology. Along with the pre-melt transitions, both, Zr-12Fe-10Cu and Zr-12Fe-15Cu, experienced deflections at 881.0°C and 895.6°C respectively, in the DSC heating curves after melting. Both of these deflections were indicative of a re-melt occurring after the initial melt occurred. Both of these transitions occurred in all of the DSC measurements for both alloys and in some instance appeared as two separate transitions very close to each other.

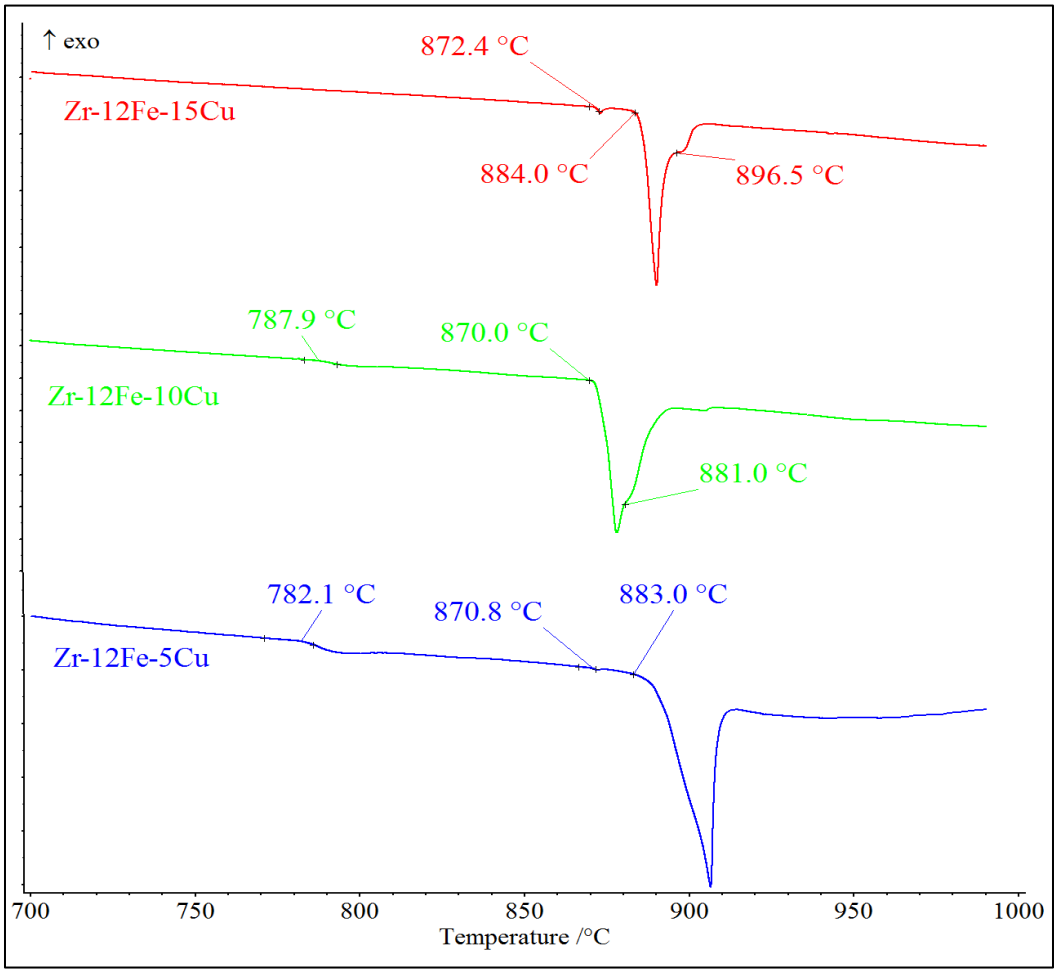

Figure 5-8: DSC curves for as-cast Zr-Fe-Cu alloys (Ordinate is not to scale).

5.2.2. Annealed Zr-Fe-Cu Alloys

There were very few differences between the as-cast and annealed alloys groups. The set of DSC heating curves for all three alloys are depicted in Figure 5-9. The Zr-12Fe-5Cu and Zr-12Fe-10Cu both experienced broad phase transitions at 795.0°C and 800.2°C. Both transitions were broad and shallow, however the depression in the DSC curve is much more subtle in the Zr-12Fe-10Cu alloy than in the Zr-12Fe-5Cu. Like in the as-cast alloy these broad transitions may be the result of a transition occurring on a non-isotherm phase boundary. Zr-12Fe-5Cu experienced a transition just before melting at 873.2°C. The transition occurred approximately 13°C before melting and was very small in comparison to the melt transition.

All three alloys had obvious melt transitions occurring at: 886.3°C for Zr-12Fe-5Cu, 870.7°C for Zr-12Fe-10Cu, and 882.7°C for Zr-12Fe-15Cu. The Zr-12Fe-5Cu alloy had the largest melting temperature at 886.3°C, although the melting temperature of Zr-12Fe-15Cu was smaller by only 3.6°C. The melting temperature of Zr-12Fe-10Cu was lower by more than 12°C. It was a challenge to precisely determine the actual melting temperature of Zr-12Fe-5Cu since the DSC heating curve only showed a gradual change as compared to Zr-12Fe-10Cu and Zr-12Fe-15Cu which showed an abrupt changed, as seen in Figure 5-9; because of this, the actual melting temperature may be larger by as much as 5°C. Both Zr-12Fe-10Cu and Zr-12Fe-15Cu experienced deflections at 888.1°C and 896.2°C, respectively, in the DSC heating curves after melting. Both of these transitions occurred in all of the DSC measurements for both alloys and in some instance appeared as two separate transitions very close to each other. Each of these deflections was indicative of a secondary melting of a lesser remnant phase that occurred after the initial melting of the bulk alloy.

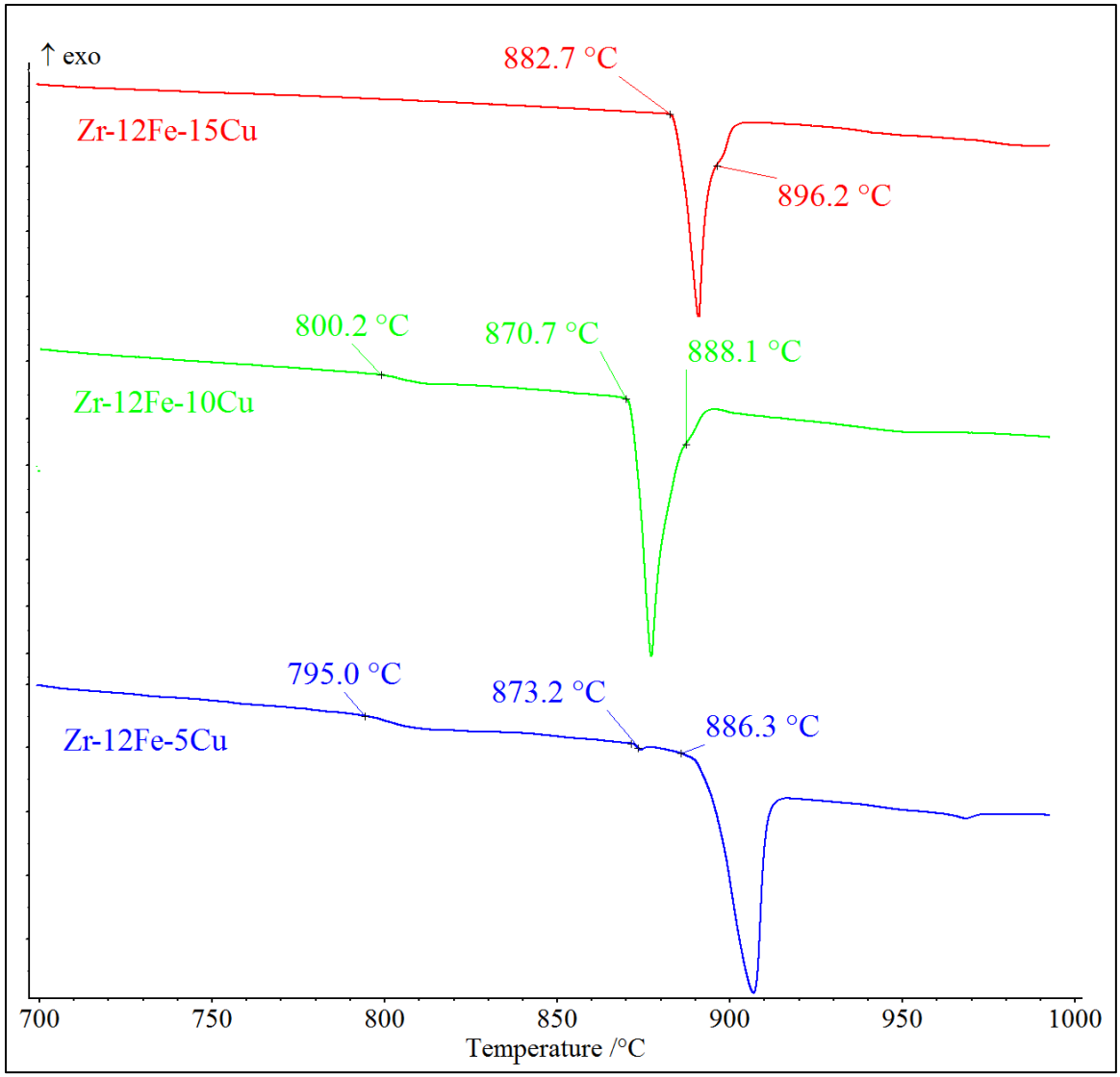

Figure 5-9: DSC curves for annealed Zr-Fe-Cu alloys (Ordinate is not to scale).

5.2.3. Phase Transition and Melting Temperatures of Zr-Fe-Cu Alloys

Little change was observed between the as-cast and annealed alloys. A summary of the DSC measurements is given in Table 5-4. The Zr-12Fe-5Cu alloy exhibited a shift in the transition temperature between the as-cast and annealed samples. Three transitions were observed in each case, however, the transition temperatures increased in the case of the annealed sample. The first transition appeared at 795°C compared to 782.1°C in the as-cast

sample. Additionally, this weak transition was significantly diminished after annealing. The small transition that occurred just before melting became more pronounced and occurred at 873.2°C in the annealed sample, compared to 870.8°C a relatively small increase of 2.4°C. Again this transition occurs within proximity to the alpha to beta zirconium transition that occurs at 865°C. Likewise, there was a small increase in the observed onset of melting by 3.3°C. The annealed Zr-12Fe-5Cu alloy had the largest onset of melting at 886.3°C.

As with Zr-12Fe-5Cu, Zr-12Fe-10Cu exhibited little change in the detected transitions over the observed temperature region. The observed first transition occurred at a higher temperature, 800.2°C, an increase of more than 12°C, which was comparable to the increase seen in Zr-12Fe-5Cu at about the same temperature. There was no practical change in the melting temperature, 870.7°C in the annealed sample vs. 870.0°C in the as-cast sample. The largest difference between the annealed samples and the as-cast samples was the temperature at which the final transition occurred after melting. In the as-cast sample, this deflection occurred at 881.0°C, near the bottom of the transition, conversely, in the annealed sample this deflection occurred at 888.1°C, near the end. The 10wt% Cu alloy had the smallest onset of melting at 870°C.

The 15wt% Cu alloy exhibited the biggest change between the annealed section and the as-cast section. While there were three observed transitions in the as-cast Zr-12Fe-15Cu alloy, there were only two in the annealed alloy. The small transition that was seen in the as-cast measurement did not appear in the DSC curve for the annealed alloy. Additionally, the melting temperature decreased slightly from 884.0°C to 882.7°C. What didn't change was the temperature at which the transition after melting occurred. In both instances, this deflection happened at ~896°C.

The measured melting temperatures were noticeably higher than those predicted. According to A.M. Savchenko et. al. the Zr-(6,12)Fe-(6,12Cu) alloys would have melting temperatures ranging from 850 – 860°C. [21] That's a difference of 10 – 20°C compared to the measured melting temperatures which had a range of 870.0 – 886.3°C.

Table 5-4: Melting and transition temperatures for all alloys in °C.

ALLOY	T1	T2	MELTING	T3
As-Cast A1	782.1	870.8	883.0	-
Annealed A1	795.0	873.2	886.3	
As-Cast A2	787.9	-	870.0	881.0
Annealed A2	800.2	-	870.7	888.1
As-Cast A3	872.4	-	884.0	896.5
Annealed A3	-	-	882.7	896.2

5.3. Thermophysical Properties of Zr-Fe-Cu Alloys

Thermal diffusivity values were measured for all three alloys using both as-cast and annealed samples from the Group C casting. A plot of the average diffusivity of each of the alloy segments at a given temperature step is shown in Figure 5-10. When plotted on the same graph, one can see that there was relatively little variation in the diffusivity measurements between the three different alloys. The 15wt% Cu exhibited the highest diffusivity values on average reaching a maximum of 4.64 ± 0.16 mm2/s. The 10wt% Cu alloy had the lowest measured valued, while Zr-12Fe-5Cu fell between Zr-12Fe-10Cu and Zr-12Fe-15Cu. Each alloy exhibited approximately the same slope, however, both the as-cast and annealed Zr-12Fe-5Cu alloys had a slightly smaller rate of increase compared to the other samples.

Table 5-5 summarizes the maximum and minimum diffusivity measurements for both the as-cast and annealed alloys. In general there was much more variation in the annealed samples compared to the as-cast samples. This was most likely the result of the sample condition at the time of the measurement. After annealing, the alloy buttons exhibited surface cracking that was not present before annealing. As a result, it is reasonable to assume that the light impinging on the surface of the sample was not uniformly absorbed and therefore wasn't transmitted through the sample evenly. Additionally, the surface cracks appeared on both sides of the sample therefore, error induced from the IR detector reading on the opposite side of the sample may have also played a part in the increased variation in each

of the measurements. Due to sample brittleness, each alloy button was not polished in an effort to avoid additional cracking and pitting, as seen in the optical images from Section 4.1.

Table 5-5: Summary of maximum and minimum thermal diffusivity values in mm^2/s.

ALLOY	MINIMUM (20°C)	MAXIMUM (260°C)
As-Cast A1	3.54 ± 0.063	4.42 ± 0.10
Annealed A1	3.46 ± 0.19	4.30 ± 0.21
As-Cast A2	3.17 ± 0.16	4.19 ± 0.22
Annealed A2	3.18 ± 0.42	4.21 ± 0.49
As-Cast A3	3.52 ± 0.15	4.64 ± 0.16
Annealed A3	3.54 ± 0.22	4.62 ± 0.21

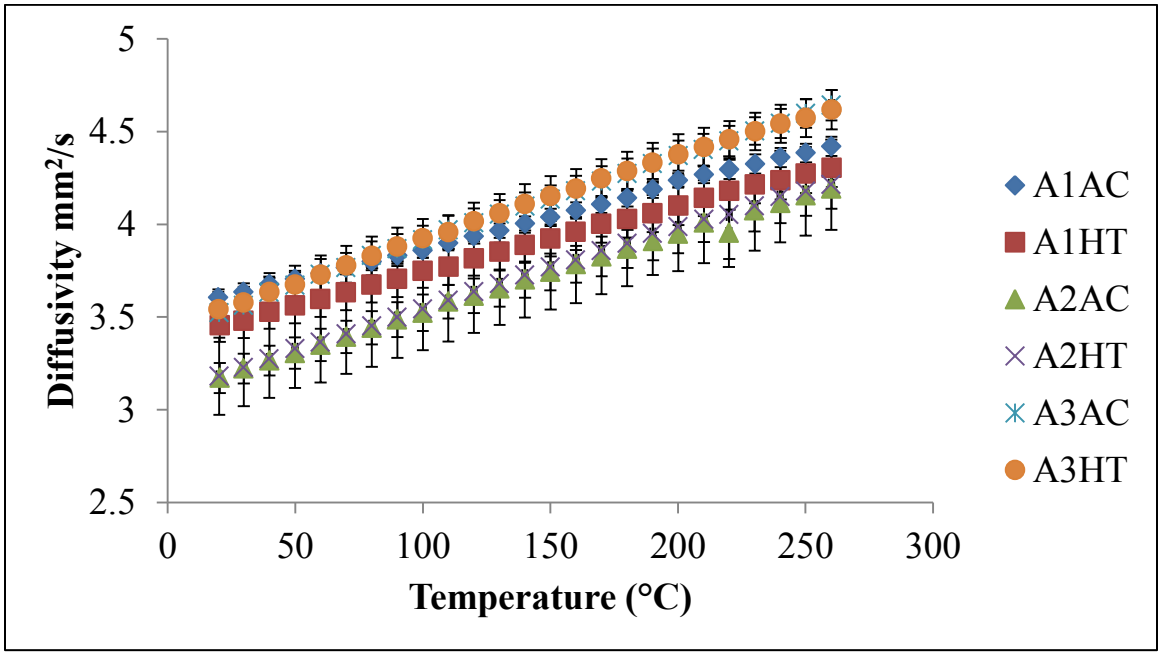

Figure 5-10: Diffusivity measurements of all Group B alloys.

Various reactor materials are compared to a representative Zr-Fe-Cu alloy in Figure 5-11. The Zr-12Fe-5Cu alloy was chosen because it showed the least amount of variation in diffusivity measurements. Reactor material values were taken from the IAEA collection of

thermophysical properties of reactor materials. [37] In general, with most pure metals and ceramics as temperature increases thermal diffusivity decreases. This is the result of the breakdown in the mechanisms that govern the transport of thermal energy (phonon and electron transport). This is shown in Figure 5-11 where the thermal diffusivity of UO_2, pure Zr metal, and Zr + 1% Nb alloy, all decrease over the temperature range. Conversely, some materials, notably Zr + 2.5% Nb and 316SS, show the same linearly increase in thermal diffusivity observed by the Zr-Fe-Cu alloys. In fact, 316SS has similar thermal diffusivity values compared to the Zr-Fe-Cu alloys over the same temperature range. Although the thermal diffusivity of the Zr-Fe-Cu alloys is smaller than pure Zr metal by a factor of three, it is notable that the alloys do exhibit similar values to other important reactor materials, most notably UO_2 fuel.

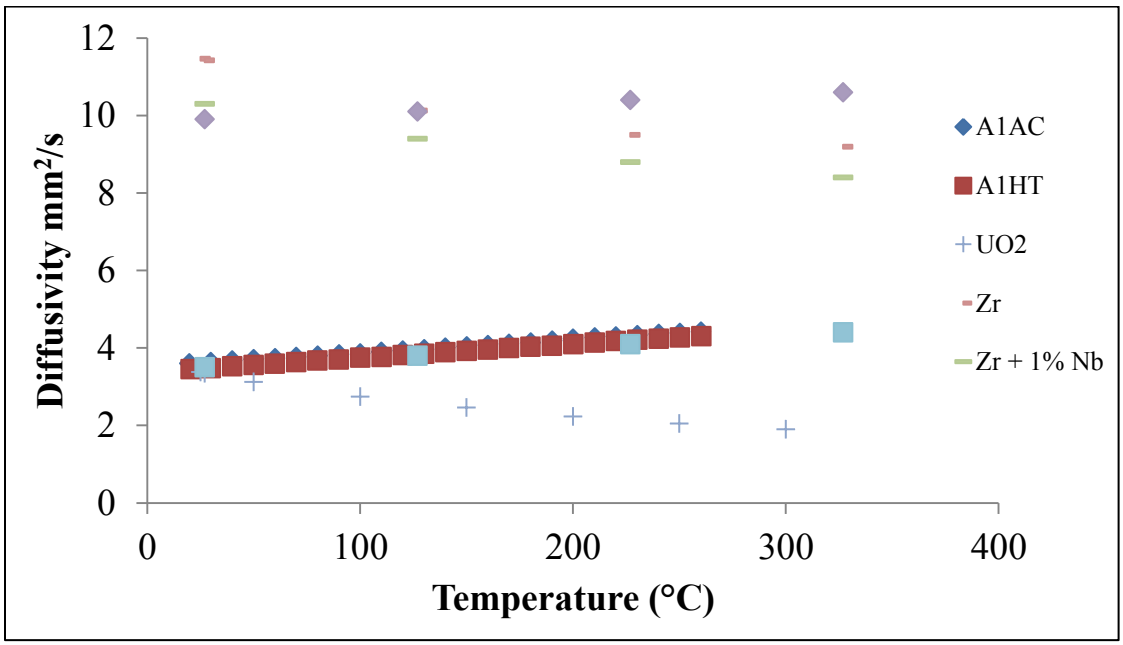

Figure 5-11: Thermal diffusivity of typical reactor materials.

6. CONCLUSIONS AND FUTURE WORKS

6.1. Conclusions

6.1.1. Zr-Fe-Cu Microstructure

Three novel Zr-Fe-Cu alloys were successfully fabricated and there microstructures characterized using EPMA and WDS. Group A was a preliminary casting and led to the development of the final casting procedures used to generate materials for further study. Both Groups B and C produced homogenous alloy mixtures as a result of the revised casting procedure with the exception of the Zr-12Fe-10Cu alloy which showed a distinct axial difference in the phase morphology. The top half was Zr rich and had features similar to that of Zr-12Fe-5Cu while the bottom half consisted of small islands dispersed in an intermetallic matrix. EPMA and WDS confirmed the existence of both Zr precipitates as well as two general intermetallic phases based on the atom percent measured. Annealing of the Group B alloys proved to further increase the homogeneity of the samples, decreasing the variation in the elemental composition of the intermetallic phases. Group C annealing was not as complete due to the increased sample size, however, annealing times were not increased to maintain continuity between the DSC and LFA data sets.

The Zr-12Fe-5Cu alloy was composed of the three different phases. The first was a Zr solution phase with limited solubility of both Fe and Cu. Next, an intermetallic matrix phase with an apparent $Zr_2(Fe,Cu)$ structure. Lastly, was a Fe rich intermediate compound which had a 3:1 ratio of Fe and Cu to Zr. This phase morphology in consistent with what was seen in similar zirconium alloys. [32] The 10wt% Cu alloy proved to be the most complex of the three alloys. The phase morphology varied greatly between the top and bottom of the cast alloy slug. The top was Zr rich and exhibited the formation of Zr precipitates. Elemental composition in all of the observed intermetallic phases varied giving rise to the possibility of 6 different phases in the annealed Group B samples. The bottom half of the ingot proved to be Zr depleted and lacked any Zr precipitates and formed a phase structure more similar to that predicted by the CALPHAD models (Refer to Figure 3-2). The 15wt% Cu alloy also exhibited a relatively complex phase morphology that consisted of four

different intermetallic phases based on WDS data and BSE images. As-cast samples showed a larger variation in the elemental composition of all but one phase, however, after annealing the phases appeared much more uniform. Overall, the cast alloys showed the projected combination of phases with the exception of the $ZrFe_2$ Laves phase which was predicted for the Zr-12Fe-15Cu alloy but was not detected.

6.1.2. Melting Temperatures and Phase Transitions

Introductory DSC measurements were performed in order to provide experimental data to compliment the CALPHAD models being generated at LLNL. The results of the DSC analysis showed the possibility of a phase transition between ambient and melting in each of the three alloys. There was little difference between the as-cast samples and the annealed samples. In Zr-12Fe-5Cu and Zr-12Fe-10Cu, the first transition occurred at ~780°C in the as-cast samples and ~800°C in the annealed samples. Each of the transitions was very broad and shallow and it was not readily apparent that there was a transition from the DDSC curve, however, there was a clear depression in the DSC curves at those temperatures.

The same transitions were observed in the annealed samples, however, the transition temperatures shifted, pre-melt transitions increasing by ~13°C in each alloy. In both Zr-12Fe-5Cu and Zr-12Fe-15Cu there was a small transition approximately 11°C before melting in the as-cast samples which for the Zr-12Fe-5Cu alloy is in proximity to the αZr to βZr transition which occurs at 865°C. This same transition was observed in the annealed Zr-12Fe-5Cu alloys, however, in the annealed Zr-12Fe-15Cu alloys, this transition was not present. All three alloys showed clear melt transitions ranging from 870°C to 886.3°C. The 5wt% Cu alloy had the largest onset of melting ranging from 883.0°C to 886.3°C between as-cast and annealed samples. The 10wt% Cu alloy had the lowest melting temperature at approximately 870°C for both samples, while Zr-12Fe-15Cu had a melting temperature just below that of Zr-12Fe-5Cu. The as-cast sample had a melting point of 884.0°C while the annealed sample decreased slightly to 882.7°C. In addition to the initial melt, both the Zr-12Fe-10Cu and Zr-12Fe-15Cu alloys experience a deflection in the DSC curve after melting. In some instances, two transitions that were very close together appeared. This phenomenon

was indicative of the sample partially melting and then re-melting, the possible result of sample contamination.

6.1.3. Thermal Diffusivity of Zr-Fe-Cu Alloys

Thermal diffusivity data measured from LFA measurements showed that in all three alloys, the diffusivity increased linearly versus temperature from ambient to 260°C at approximately the same rate. Diffusivity measurements were completed from three different sections of each alloy. The as-cast measurements were much more uniform than the annealed samples, most likely due to cracks that formed during annealing. Each of the three Zr-12Fe-5Cu alloys fell within the statistical error of each other. The 10wt% Cu alloy showed increased variation, which was expected because of the varying phase morphologies. The two measured Zr-12Fe-15Cu sections were also in fair agreement with each other. The annealed samples showed much greater variation between each of the three portions of the alloy which was the opposite effect of what one would expect. The increased variation was most likely the result of sample condition at the time of measurement. Each of the annealed samples exhibited surface cracking on both sides of the samples.

In most pure metals and ceramics, thermal diffusivity decreases with increasing temperature as a result in the breakdown of the thermal transport mechanisms. Figure 5-11 showed this trend with many common reactor materials including both pure zirconium as well as UO_2. In some alloys, including the alloys in this study, this trend is reversed and the thermal diffusivity actually increases for a given temperature range. For instance, over the same temperature range, 316 SS had almost identical thermal diffusivity values as the Zr-Fe-Cu alloys and exhibited the same linear increase. The data from the LFA measurements showed that the Zr-Fe-Cu alloy system has similar magnitudes for the diffusivity compared to common reactor materials.

6.2. Future Works

Several recommendations can be made toward future works involving the study of this set of Zr based alloys. These alloys were characterized as a course matrix for scoping

purposes, but since this initial characterization is now complete further alloys should be fabricated with a finer elemental distribution to better understand the behavior of these alloys; including variations in both the Cu and Fe compositions. With that said, further analysis still needs to be done on the original group of alloys to better understand the phase morphology observed in each alloy, particularly the formation of the three apparent $Zr_2(Fe,Cu)$ intermetallic phases. More detailed analysis techniques such as X-ray diffraction, neutron diffraction, and transmission electron microscopy need to be implemented in order to determine the true phases present as well as their crystallographic structures. Knowing the crystal structure of each of the observed phases may help to better understand the presence of two distinct morphologies in the Fe rich intermetallic phases.

Furthermore, a more detailed analysis may be performed to develop a more accurate basis for the thermophysical properties of the Zr-Fe-Cu alloys. A more detailed alloy matrix with varying Fe and Cu compositions will help form a better basis for the development of the ternary phase diagram. More experimental points will help to improve the database used to create the ternary phase diagrams using CALPHAD. Additionally, further DSC measurements should be made using higher purity argon gas to ensure oxidation does not affect the data. Moreover, enthalpy of formation values could be measured to compare to predicted values.

Finally, further LFA measurements may be made. This can be achieved by first determining the annealing time needed to produce completely homogenous samples, such as those seen in the Group B DSC measurements. Additionally, the casting procedure can be modified to include slower cooling times in an effort to ensure equilibrium phases are present in the as-cast alloys with little axial variation in phase composition. A more uniform ingot will allow for thicker LFA samples to be cut which can then be ground and polished to the desired thickness. A sensitivity analysis may be performed to determine the ideal sample thickness. Sample integrity is key to LFA measurements, therefore, perfectly parallel samples as well as polished surfaces will improve the results. Because of the LFA measurements showed that the diffusivity of the three alloys were relatively similar, it is not certain whether or not a finer sample matrix will improve the results and thus may not be needed in future experiments.

The course alloy matrix studied here represents only 1 of 4 test groups originally established by A. Savchenko et. al. Additional alloying elements could be added to the matrix to determine their contributation to the metal matrix form. Finally, the purpose of these alloys is to act as a coating metal in the final fuel form, therefore the next logical step would be to begin sessile-drop tests to determine the wetting behavior of these alloys.

REFERENCES

[1] IAEA (International Atomic Energy Agency), Nuclear Technology Review 2007, Vienna, Austria, 2007.

[2] IAEA (International Atomic Energy Agency), Nuclear Technology Review 2012, Viena, Austria, 2012.

[3] D. Crawford, D. Porter, S. Hayes, M. Meyer, D. Petti, K. Pasamehmetoglu, An approach to fuel development and qualification, J. Nucl. Mater, 371 (2007) 232-242.

[4] A.M. Savhenko, A.V. Vatulin, A.V. Morozov, I.V. Dorbrikova, S.A. Ershov, S.V. Maranchak, Z.N. Petrova, Y.V. Konovalov, Inert matrix fuel with low melting point zirconium brazing alloys, J. Nucl. Mater, 352 (2006) 334-340.

[5] A. Savchenko, I. Konvalov, A. Vatulin, A. Morozov, V. Orlov, O. Uferov, S. Ershov, A. Laushkin, G. Kulakov, S. Maranchak, Z. Petrova, Dispersion type zirconium matrix fuels fabricated by capillary impregnation method, J. Nucl. Mater, 362 (2007) 356-363.

[6] A.M. Savhenko, A.V. Vatulin, E.M. Glagovsky, I.I. Konovalov, A.V. Morozov, A.V. Kozlov, S.A. Ershov, V.A. Mishunin, G.V. Kulakov, V.I. Sorokin, A.P. Simonov, Z.N. Petrova, V.V. Fedotov, Main results of the development of dipersion type IMF at A.A. Bochvar Institute, J. Nucl. Mater, 396 (2010) 26-31

[7] W.N. Association, Nuclear Power in the USA, in, 2013. [Online]. Available: http://www.world-nuclear.org/info/Country-Profiles/Countries-T-Z/USA--Nuclear-Power/#.UadsGrVlm0w

[8] H., H. Stehle, H. Assmann, F. Wunderlich, Uranium Dioxide Properties for LWR Fuel Rods, Nucl. Eng. Des., 33 (1975) 230-260.

[9] G.L. Hoffman, R.G. Pahl, C.E. Lahm, D.L. Porter, Swelling behavior of U-Pu-Zr Fuel, Metall. Mater. Trans. A, 21A (1990) 517-528

[10] V.V. Rondinella, T. Wiss, The high burn-up structure in nuclear fuel, Materials Today, 2010, pp. 24-32. ISSN: 1369 7021

[11] D. Crawford, LWR Fuel Performance, Presentation, ATR NSUF User Week 2009, Idaho National Lab, Idaho Falls, ATR National Scientific User Facility, 2009. [Online]. Available: http://atrnsuf.inl.gov/LinkClick.aspx?fileticket=EVeSpII4qPI=

[12] H. Bailly, D. Menessier, C. Prunier, The Nuclear Fuel of Pressurized Water Reactors and Fast Neutron Reactors: Design and Behaviour, Cachan, France, Lavoisier, 1999.

[13] W.L. Lyon, W.E. Baily, The solid-liquid phase diagram of the UO2-PuO2 system, J. Nucl. Mater., 22 (1967) 332-339.

[14] R.E. Latta, R.E. Fryxell, Determination of solidus-liquidus temperatures in the UO2+x system (-0.50<x<0.20), J. Nucl. Mater., 35 (1970) 195-210.

[15] T. Yamamoto, M. Yamamoto, Nuclear analysis of PIE data of irradiated BWR 8x8-2 and 8x8-4 UO2 fuel assemblies, J. Nucl. Sci. Technol., 45 (2008) 1193-1214.

[16] S. Ishmoto, M. Hirai, K. Ito, Y. Korei, Thermal conductivity of UO2-BeO pellet, J. Nucl. Sci. Technol., 33 (1996) 134-140.

[17] A.M. Savhenko, A.V. Vatulin, A.V. Morozov, V.L. Sirotin, I.V. Dobrikova, G.V. Kulakov, S.A. Ershov, V.P. Kostomarov, Y.I. Stelyuk, Inert matrix fuel in dipersion type fuel elements, J. Nucl. Mater., 352 (2006) 372-377.

[18] P. Turchi, Ultra-High Burn-up Metallic Inert Matrix Nuclear Fuel Concept, Presentation, Texas A&M University, College Station, 2011.

[19] A. Savchenko, A. Vatulin, I. Knovalov, A. Morozov, V. Sorokin, S. Maranchak, Fuel of novel generation for PWR and as alternative to MOX fuel, Energy Convers. Manage., 51 (2010) 1826-1833.

[20] G.L. Hofman, Y.S. Kim, M.R. Finlay, J.L. Snelgrove, S.L. Hayes, M.K. Meyer, C.R. Clark, F. Huet, Recent observations at the postirradiation examination of low-enriched U-Mo miniplates irradiated to high burnup, Research Reactor Fuel Management, Munchen, Germany, 2004.

[21] A.M. Savchenko, A.V. Vatulin, A.V. Morozov, G.V. Kulakov, S.A. Ershov, A.V. Laushkin, S.V. Maranchak, Y.V. Konovalov, E.K. Malamanova, Zirconium alloys matrix as innovative material for composite fuel, Prog. Nucl. Energy, 57 (2012) 138-144.

[22] D. Arias, J.P. Abriata, The Fe-Zr (Iron-Zirconium) System, Bull. Alloy. Phase. Diagr., 9 (1988) 597-604.

[23] O. Kubaschewski, Iron-Binary Phase Diagrams, New York: Springer Publications, 1982, p. 175.

[24] A.D. Pelton, L. Leibowitz, R.A. Blomquist, Thermodynamic analysis of phase equilibria in the iron-zirconium system, J. Nucl. Mater., 201 (1993) 218-224.

[25] Z. Alekseeva, N. Korotkova, Russ. Met., 4 (1989) 197.

[26] L.R. Bairi, S. Ningshen, U. Kamachi, B. Raj, Microstructural analysis and corrosion behavior of D9 stainless steel - Zirconium metal waste form alloys, Corros. Sci., 52 (2010) 2291-2302.

[27] D. Arias, J.P. Abriata, Cu-Zr (Cooper-Zirconium), Bull. Alloy. Phase. Diagr., 11 (1990) 452-459.

[28] R.N. Guillemette, Methods of soil analysis. Part 5. Mineralogical Methods, in: A.L. Ulery, L.R. Drees (Eds.), Methods of Soil Analysis, Soil Science Society of America Inc., Wisconsin, 2008, pp. 325-365.

[29] T. Flanagan, C.N. Park, W. Oates, Hysteresis in solid state reactions, Prog. Solid State Chem., 23 (1995) 291-363.

[30] W.J. Parker, R.J. Jenkins, C.P. Butler, G.L. Abbott, Flash method of determining thermal diffusivity, heat capacity, and thermal conductivity, J. Appl. Phys, 9 (1961) 1679-1684.

[31] D.P. Abraham, S.M. McDeavitt, J. Park, Microstructure and phase identification in type 304 stainless steel-zirconium alloys, Metall. Mater. Trans. A, 27A (1996) 2151-2159.

[32] D.P. Abraham, J.W. Richardson, S.M. McDeavitt, Laves intermetallics in stainless-steel-zirconium alloys, Mater. Sci. Eng., A, A239-240 (1997) 658-664.

[33] T.O. Malakhova, Z.M. Alekseyeva, The Zr-Fe phase diagram in the range 20-40 at% Fe and the crystalline structure of the intermetallic compound Zr3Fe, J. Less-Common Met., 81 (1981) 293-300.

[34] J.H. Westbrook, R.L. Fleischer, Crystal Structures of Intermetallic Compounds, John Wiley & Sons Ltd, West Sussex, 1995.

[35] C. Servant, C. Gueneau, I. Ansara, Experimental and thermodynamic assessment of the Fe-Zr system, J. Alloys Compd., 220 (1995) 19-26.

[36] M. Jiang, K. Oikawa, T. Ikeshojo, L. Wulff, K. Ishida, Thermodynamic calculations of Fe-Zr and Fe-Zr-C Systems, J. Phase Equilib., 22 (2001) 406-417.

[37] IAEA, Thermophysical Properties of Materials for Nuclear Engineering: A Tutorial and Collection of Data, Nuclear Power Technology Development Section, Viena, Austria 2008